

University of St Andrews



Full metadata for this thesis is available in
St Andrews Research Repository
at:

<http://research-repository.st-andrews.ac.uk/>

This thesis is protected by original copyright

NEUTRON DEPTH DOSE MEASUREMENTS IN A TISSUE-EQUIVALENT
PHANTOM IRRADIATED BY COLLIMATED BEAMS OF
Pu Be, D - D AND D - T NEUTRONS

A Thesis
presented by
Robert Crawford Lawson, B.Sc.
to the
University of St. Andrews
in application for the degree
of Doctor of Philosophy



DECLARATION

I hereby declare that the following Thesis is based on research carried out by me, that the Thesis is my own composition, and that it has not previously been presented for a Higher Degree.

Robert b. Lawson.

CERTIFICATE

We certify that Robert Crawford Lawson, B.Sc., has spent nine terms as a research student in the Department of Experimental Physics of the United College of St. Salvator and St. Leonard in the University of St. Andrews, that he has fulfilled the conditions of Ordinance No. 16 of the University Court of St. Andrews and that he is qualified to submit the accompanying Thesis in application for the Degree of Doctor of Philosophy.

J. F. Allen
.....
Research Supervisor

J. H. Clark
.....
Research Supervisor

CAREER

I matriculated in the United College of St. Salvator and St. Leonard in the University of St. Andrews in October 1958 and followed a course leading to graduation in June 1962 with the Degree of Bachelor of Science with First Class Honours in Natural Philosophy. In July 1962, I accepted the post of Scientific Officer with the United Kingdom Atomic Energy Authority, Chapelcross Works, Annan, Dumfriesshire, and began research into the problems associated with Neutron Dosimetry. This research was accepted by the Senatus Academicus of the University of St. Andrews as subject matter for this thesis in October 1963. Under the conditions of Ordinance No. 16 of the University Court of St. Andrews, I have spent two years at Chapelcross, and three terms in the University of St. Andrews during which time I held a Carnegie Senior Scholarship.

ACKNOWLEDGEMENTS

I should like to record my sincere thanks to:-

Professor J. F. Allen, F.R.S. : for his interest and for allowing me the facilities of the Department of Natural Philosophy.

The following members of staff
at the U.K.A.E.A.,
Chapelcross Works,
Annan.

Dr. J. H. Martin : for his encouragement and for suggesting the topic and providing the necessary facilities at the U.K.A.E.A., Chapelcross Works.

Dr. D. E. Watt : for his supervision and his stimulating advice.

Messrs. M. Clare and S. Hughes : for helpful discussions.

Messrs. N. Brow and J. Pagan : for assistance with the computer programming.

Mr. S. Macaulay : for assistance with the photography.

Mrs. H. Macaulay : for the efficient typing.

The Carnegie Trust and the

Dumfries Educational Trust

:

for the award of maintenance
grants.

SUMMARY

Neutron irradiation facilities suitable for dosimetry studies were constructed which provided collimated beams of fast neutrons from a 10 curie Pu-Be source, and from the D(d,n) and T(d,n) reactions. An elliptically shaped polythene phantom, filled with tissue-equivalent liquid, was exposed to the beams and the components of absorbed dose were measured at depth in the phantom for beams incident on both the major and minor axes. A Bragg-Gray type detector, made from plastic phosphor and polyvinyltoluene sheet, was used to measure the proton recoil dose from the fast neutrons. The components of absorbed dose due to the thermal neutron reactions, $^{14}\text{N}(n,p) ^{14}\text{C}$ and $^1\text{H}(n,\gamma) ^2\text{D}$, were derived from the thermal neutron flux measured with a LiI(Eu) crystal and corrected for perturbation effects such as flux depression.

Thermal neutron flux distributions at depth in tissue were measured for various collimated beams incident on different sized phantoms. The experimental measurement of the diffusion length of thermal neutrons in tissue-equivalent liquid permitted calculation of the transport mean free path, and hence the determination of an accurate flux depression factor for the LiI(Eu) detector used to measure the thermal flux.

Quality factors for the various neutron beams were calculated from the proton recoil dose measurements and the dose as a function of linear energy transfer, LET, was determined at depth in the phantom.

The experimental components of dose, quality factors, and dose as

a function of LET, are compared with the published theoretical and experimental results.

PUBLICATIONS

A Papers Published

- WATT, D. E., LAWSON, R. C., and MARTIN, J. H., 1963, The Measurement of Energy Deposited at Depth in Tissue for an Incident Pu-Be Spectrum, I.A.E.A. Symposium on Biological Effects of Neutron Irradiations, Paper SM 44/11.
- WATT, D. E., LAWSON, R. C., and WILLIAMSON, J., 1964, A Low Cost Neutron Facility for Dosimetry Studies, Physics in Medicine and Biology, Vol. 9, No. 4, p.477.
- LAWSON, R. C., and WATT, D. E., 1964, Neutron Depth Dose Measurements in a Tissue-Equivalent Phantom for an Incident Pu-Be Spectrum, Physics in Medicine and Biology, Vol. 9, No. 4, p. 487.

B Papers Submitted for Publication

- LAWSON, R. C., CLARE, D. M., and WATT, D. E., (D,D) and (D,T) Neutron Depth Dose Measurements in a Tissue-Equivalent Phantom.
- LAWSON, R. C., and WATT, D. E., Thermal Neutron Depth Dose Dependence on Beam and Phantom Size for Incident Collimated Beams of Fast Neutrons.
- LAWSON, R. C., and WATT, D. E., The LET Distribution of the Recoil Proton Dose at Depth in Tissue Due to Fast Neutron Irradiation.

TABLE OF CONTENTS

		<u>Page</u>
CHAPTER 1	THE PRESENT STATUS OF NEUTRON DOSIMETRY	
	§1.1 Introduction.	1
	§1.2 Terminology Employed in Neutron Dosimetry.	3
	§1.3 Survey of the Theories on Energy Deposition.	7
	§1.4 Techniques of Neutron Dosimetry.	12
	§1.4.1 Calorimetric Methods.	13
	§1.4.2 Spectral Measurements.	14
	§1.4.3 Chemical and Photographic Dosimeters.	17
	§1.4.4 Ionisation Devices.	18
	§1.4.5 Special Counting Methods.	23
	§1.5 Review of Experimental Dose Measurements.	24
	§1.6 Dose Equivalent.	31
	§1.7 Distribution of Absorbed Dose as a Function of Linear Energy Transfer.	32
	§1.8 Conclusions.	35
CHAPTER 2	NEUTRON FACILITIES FOR DOSIMETRY STUDIES	
	§2.1 Introduction.	38
	§2.2 Pu-Be Facility.	41
	§2.2.1 Selection of Shielding Material.	43
	§2.2.2 Design of Shield.	44
	§2.2.3 Performance of the Shield.	45
	§2.3 Monoenergetic Neutrons by the DD and DT Reactions.	48

	<u>Page</u>
§2.3.1 Method of Neutron Production.	48
§2.3.2 Neutron Energies.	51
§2.3.3 Methods of Measuring Neutron Flux.	55
§2.3.4 Performance of the Shield.	66
§2.3.5 Contamination of the DD and DT Neutron Beams.	66
§2.4 Thermal Neutron Production.	69
 CHAPTER 3 NEUTRON DEPTH DOSE MEASUREMENTS IN A TISSUE-EQUIVALENT PHANTOM FOR AN INCIDENT Pu-Be SPECTRUM	
§3.1 Neutron Irradiation Conditions.	71
§3.2 Flux Measurements.	73
§3.3 Thermal Neutron Distribution at Depth in Tissue.	75
§3.3.1 Effective Crystal Surface Area.	76
§3.3.2 Flux Attenuation by the Perspex Probe.	77
§3.3.3 Flux Depression and Self Shielding.	77
§3.3.4 Neutron Scattering and Leakage Through the Shielding.	78
§3.4 Thermal Depth Dose.	79
§3.4.1 $^{14}\text{N}(n, p) ^{14}\text{C}$ Depth Dose.	79
§3.4.2 $^1\text{H}(n, \gamma) ^2\text{D}$ Depth Dose.	80
§3.5 Fast Neutron Recoil Proton Dose.	80
§3.6 Discussion of Results.	88
§3.6.1 Thermal Neutrons.	88
§3.6.2 Fast Neutrons.	92
§3.7 Dose Equivalent for Proton Recoils.	96

§3.7.1	Mean LET - for Radiation Protection.	100
§3.7.2	Dose in Rems.	105

CHAPTER 4 EXTENSION OF DEPTH DOSE MEASUREMENTS TO IRRADIATION
BY MONOENERGETIC DD AND DT NEUTRONS

§4.1	Introduction.	107
§4.2	Thermal Neutron Depth Dose.	108
§4.2.1	Thermal Neutron Distribution at Depth in Tissue.	108
§4.2.2	$^{14}\text{N}(n, p) ^{14}\text{C}$ Dose.	109
§4.2.3	$^1\text{H}(n, \gamma) ^2\text{D}$ Dose.	110
§4.3	Fast Neutron Proton Recoil Dose.	111
§4.3.1	DD Proton Recoil Dose.	111
§4.3.2	DT Proton Recoil Dose.	113
§4.4	Dose Equivalent for Proton Recoils.	115
§4.4.1	Quality Factor.	117
§4.4.2	Dose in Rems.	120
§4.4.3	Quality Factor for the Total Dose.	121

CHAPTER 5 THE LET DISTRIBUTION OF THE RECOIL PROTON DOSE

§5.1	Introduction.	124
§5.2	Theoretical Treatment of the Distribution of Dose in LET.	126
§5.3	Comparison of the Experimental Techniques.	129
§5.4	The Experimental Distribution of Dose Using the NE 102 Detector.	133
§5.5	Comparison of the NE 102 Measurements with Snyder's Calculations.	138

CHAPTER 6	THERMAL NEUTRON DEPTH DOSE DEPENDENCE ON BEAM AND PHANTOM SIZE	
§6.1	Introduction.	142
§6.2	Variation of Fast Neutron Flux with Beam Size.	142
§6.3	Thermal Neutron Flux due to Assorted Beams of Incident Fast Neutrons.	143
§6.4	Effect of Phantom Shape on Thermal Neutron Flux.	145
§6.5	Determination of Peak Position and Magnitude.	147
§6.6	Two Group Theory Determination of Thermal Peak.	149
§6.7	Theoretical Prediction of the Magnitude of the Peak.	153
§6.8	Conclusions.	160
CHAPTER 7	FUNDAMENTAL PARAMETERS OF TISSUE-EQUIVALENT LIQUID REQUIRED IN CALCULATIONS	
§7.1	Introduction.	162
§7.2	Thermal Diffusion Length, L , and Transport Neutron Free Path, λ_{tr} , for tissue.	162
§7.3	Flux Depression Caused by a $\text{LiI}(\text{Eu})$ Crystal.	172
CHAPTER 8	CONCLUSIONS AND RECOMMENDATIONS FOR THE FUTURE.	176
REFERENCES.		179
APPENDIX 1	Chapelcross Fortran Programme CXF 148.	187
APPENDIX 2	Chapelcross Fortran Programme CXF 157.	189
APPENDIX 3	LET for Protons in Water.	194

LIST OF ILLUSTRATIONS

	TITLE	OPPOSITE PAGE
Fig. 1.1	Polythene Phantom and Author.	1
Fig. 2.1	Standard Plutonium-Beryllium Neutron Source.	41
Fig. 2.2(a)	Photograph of Neutron Source.	45
Fig. 2.2(b)	Photograph of Neutron Shield.	45
Fig. 2.3	Profile of the Fast Neutron Beam from the Collimator.	48
Fig. 2.4	The Observed Flux at the Collimator Exit.	48
Fig. 2.5	Photograph of the 600 KV Electrostatic Generator.	49
Fig. 2.6	Photograph of the Particle Accelerator.	49
Fig. 2.7	Photograph of the Target System.	50
Fig. 2.8	The Effective Centre of the Long Counter.	61
Fig. 3.1	Schematic Diagram of Irradiation Conditions.	71
Fig. 3.2	Error Due to Thermal Neutrons in Beam.	75
Fig. 3.3	Depth Distribution of the Thermal Neutron Flux, and the $^{14}\text{N}(n, p)^{14}\text{C}$ Dose in Rads, for Each Fast Neutron per cm^2 Incident on the Front Surface of the Tissue.	77
Fig. 3.4	Comparison of Measured $^{14}\text{N}(n, p)^{14}\text{C}$ Dose with Snyder's Theoretical Data.	80
Fig. 3.5	Comparison of Measured $^1\text{H}(n, \gamma)^2\text{D}$ Dose with Snyder's Theoretical Data.	80
Fig. 3.6	Response of the NE 102 Plastic Phosphor.	82
Fig. 3.7	Proton Tracks in Phosphor.	85
Fig. 3.8	Recoil Proton Dose Deposited in Tissue.	88

	TITLE	OPPOSITE PAGE
Fig. 3.9	Comparison of Published Results for the Total Dose in Rads due to Fast Neutrons.	96
Fig. 3.10	Calibration of Channel Width in terms of Proton Energy.	102
Fig. 3.11	Dose per Unit LET Interval Plotted Against the LET.	103
Fig. 3.12	Dose Equivalent for Proton Recoils at Depth in Tissue.	105
Fig. 4.1	Schematic Diagram of the Irradiation Conditions.	107
Fig. 4.2	The $^{14}\text{N}(n, p)^{14}\text{C}$ Dose for DD Neutrons Normalised to One Count per Minute on the Standard.	109
Fig. 4.3	The $^{14}\text{N}(n, p)^{14}\text{C}$ Dose for DD Neutrons in Rads/n/cm ² .	109
Fig. 4.4	The $^{14}\text{N}(n, p)^{14}\text{C}$ Dose for DT Neutrons in Rads/n/cm ² .	109
Fig. 4.5	The $^1\text{H}(n, \gamma)^2\text{D}$ Dose for DD Neutrons in Rads/n/cm ² .	111
Fig. 4.6	The $^1\text{H}(n, \gamma)^2\text{D}$ Dose for DT Neutrons in Rads/n/cm ² .	111
Fig. 4.7	The Recoil Proton Dose for DD Neutrons Normalised to One Count per Minute on the Standard.	111
Fig. 4.8	Comparison of Published Results for the Recoil Proton Dose in Rads due to DD Neutrons.	111
Fig. 4.9	Comparison of Published Results for the Total Dose in Rads due to DD Neutrons.	113
Fig. 4.10	The Recoil Proton Dose for DT Neutrons Normalised to One Count per Minute on the Standard.	114
Fig. 4.11	Comparison of Published Results for the Recoil Proton Dose in Rads due to DT Neutrons.	114

	TITLE	OPPOSITE PAGE
Fig. 4.12	Dose per Unit LET Interval Plotted Against the LET.	117
Fig. 4.13	The Quality Factor for DT Neutrons as a Function of Depth in the Phantom.	118
Fig. 4.14	Dose Equivalent for Proton Recoils from DD Neutrons.	120
Fig. 4.15	Dose Equivalent for Proton Recoils from DT Neutrons.	120
Fig. 5.1	LET Distribution of Absorbed Energy for DD Neutrons.	134
Fig. 5.2	Comparison of the Measured LET Distribution of Absorbed Energy with Boag's Theoretical Curves, for 2.5 MeV Neutrons.	135
Fig. 5.3	LET Distribution of Absorbed Energy for DT Neutrons from the 2 in. Collimator.	136
Fig. 5.4	LET Distribution of Absorbed Energy for DT Neutrons from the 6 in. Collimator.	136
Fig. 5.5	Maximum Value of the LET Distribution as a Function of Proton Energy.	137
Fig. 5.6	Comparison of the Measured LET Distribution of Absorbed Energy with Boag's Theoretical Curves, for 14.1 MeV Neutrons.	138
Fig. 5.7	Comparison of the Measured LET Distribution of Absorbed Energy with Snyder's Histograms, for 2.5 MeV Neutrons.	138
Fig. 6.1	Variation of Normalised Thermal Neutron Flux with Beam Size for Incident Pu-Be Neutrons.	144.
Fig. 6.2	Thermal Neutron Flux from 2 in. Beam Pu-Be Neutrons for Assorted Phantom Sizes Measured Along the Major Axis.	145
Fig. 6.3	Thermal Neutron Flux from 6 in. Beam Pu-Be Neutrons for Assorted Phantom Sizes Measured Along the Major Axis.	145

	TITLE	OPPOSITE PAGE
Fig. 6.4	Thermal Neutron Flux from 6 in. Beam Pu-Be Neutrons for Assorted Phantom Sizes Measured Along the Minor Axis.	146
Fig. 6.5	Variation in the Thermal Neutron Peak Magnitude with Phantom Size.	148
Fig. 6.6	Spherical Co-ordinates.	154
Fig. 7.1	Thermal Neutron Diffusion Length.	170

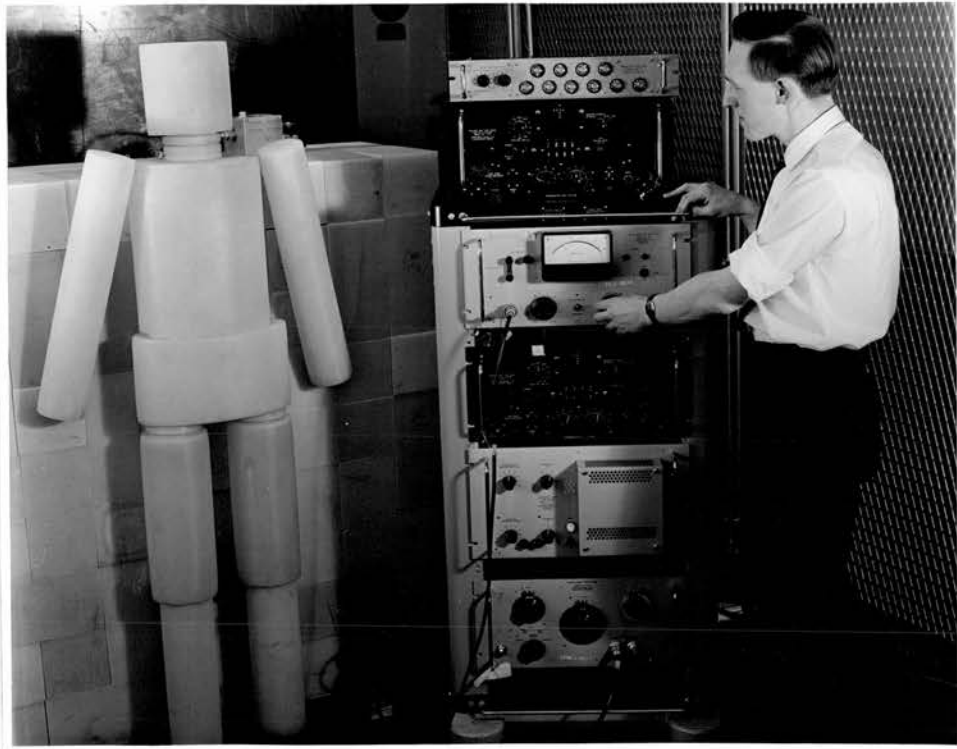


Fig. 1.1 Polythene Phantom and Author.

CHAPTER ONE

THE PRESENT STATUS OF NEUTRON DOSIMETRY

§1.1 Introduction

Neutron dosimetry is the measurement or calculation of the energy deposited in materials by the interaction of neutrons with the material. The object of this study was to experimentally determine the amount of energy delivered, as a function of depth, in the human body due to irradiation by collimated beams of neutrons, and to compare the results obtained with the currently accepted theoretical values. A polythene phantom built to the dimensions recommended by Bush (1949) for the standard man, and filled with tissue-equivalent liquid, was used to simulate the human body (Fig. 1.1). Although the phantom is a radical simplification of the human shape, the statistical spread in the dimensions of the population is such that it provides a suitable average on which to base dose measurements.

Neutrons interact with atomic nuclei in tissue, transferring a certain fraction of their energy to secondary charged particles which distribute this energy through the material by ionising and exciting some of the molecules in the vicinity of their tracks. Secondary uncharged particles can also be formed, for example gamma rays by the thermal neutron (n, γ) reaction. The gamma rays then lose energy by Compton scattering.

Since the interactions can take place in a number of ways dependent on the neutron energy and the atomic composition of the medium, tissue-

equivalence must be simulated more rigorously than in the case of x or γ -rays. The percentage by weight of the elements in the body are shown in Table 1.1 for soft tissue (Lea 1947), and for bone (Tobias 1952).

Table 1.1

Material	Percent by Weight							
	H	C	N	O	P	S	Ca	Other Elements
Standard Soft Tissue	10.0	12.0	4.0	73.0	0.2	0.2	0.01	0.59
Bone	4.0	17.0	5.0	48.0	5.0	0.2	20.0	0.8

The division of neutrons into energy groups is somewhat arbitrary although it depends to a limited extent on the interaction cross-sections. For the purpose of this thesis neutrons with energies up to 0.5 ev will be regarded as thermal neutrons, between 0.5 ev and 10 kev as intermediate energy neutrons and between 10 kev to 20 Mev as fast neutrons. Neutrons with energies greater than 20 Mev are relativistic neutrons and will not be considered. The transition between the ranges is gradual.

The experimental energy measurements shall be restricted to the reactions which provide the predominant sources of absorbed energy. These are the elastic collisions of fast neutrons with hydrogen atoms, and the thermal neutron reactions; $^1\text{H}(n, \gamma) ^2\text{D}$ which releases a 2.2 Mev gamma ray, and $^{14}\text{N}(n, p) ^{14}\text{C}$ which yields 0.62 Mev shared between the

carbon-14 nucleus and the recoil proton. The energy due to the recoil protons is deposited locally within microns of the reaction site whereas the gamma ray energy is deposited over considerable distances from the point of origin. Table 1.1 shows that bone contains 5% by weight of phosphorous, therefore in calculating the energy deposited in bone it is also necessary to consider the (n, γ) reaction in phosphorous-31.

Fast neutrons deposit energy mainly by elastic scattering. Since the neutron (mass M_n) in slowing down in a moderator loses a maximum fraction $\frac{4 M_R M_n}{(M_R + M_n)^2}$ of its energy to the recoil nucleus (mass M_R), it can easily be shown that the recoil protons account for 70 to 95% of the total energy deposited. At low energies elastic scattering is approximately isotropic in the centre of mass system but as the energy increases above 10 Mev the scattering becomes assymetric, peaking in the forward direction. For neutrons above a few Mev inelastic collisions are also energetically possible with C, N and O nuclei, which at energies above 10 Mev may be as probable as elastic scattering (Randolph 1957).

§1.2 Terminology Employed in Neutron Dosimetry

Dosimetry units have been, and are being, continuously redefined as new experimental techniques are evolved. A quantity of fundamental importance in neutron physics is the neutron flux density which is the number of neutrons entering a sphere of unit cross-sectional area per second. This shall simply be referred to as "neutron flux" or "flux".

Early dose measurements were obtained using Victoreen chambers and the "n" Unit, introduced in 1942 by Aebersold and Lawrence. This

represented the amount of neutron radiation required to produce the same discharge in a 100-r Victoreen chamber as one roentgen (r) of x-rays. It was rejected on the grounds that the response of the chamber was not constant with neutron energy, also two chambers which gave identical readings for x-rays were found to differ by as much as 10% for neutrons. To calculate the dose both the energy spectrum and chamber sensitivity as a function of neutron energy were required.

Gray (1940) suggested the " ν " unit defined such that "The dose of neutrons at a point shall be 1 ν when the associated corpuscular radiations produced in water liberate in air 1 e.s.u. of charge of either sign per 0.001293g of air". This was not widely adopted due to difficulties encountered in measuring the ionisation, and also, the response varied with neutron energy such that the dose would be underestimated at thermal energies.

Following this Parker (1948) defined the "roentgen-equivalent-physical" (rep) as "that dose of ionising radiation which produces an energy absorption of 83 ergs/cc of tissue". This was later altered to read 93 ergs/cc of tissue to give better agreement with the energy absorbed/cc of tissue from a dose of 1 r of hard x-rays or γ -rays.

The currently accepted units of neutron dose are based on the energy absorbed per gram of material under consideration and can be applied to all ionising radiation. The rad is the established unit of absorbed dose representing an absorption of 100 ergs/g. The first collision dose is measured simply in ergs/g.

The absorbed dose (D), by the I.C.R.U. 1962 recommendations, is the energy imparted by ionising radiation per unit mass of material at the point of interest,

$$D = \frac{\Delta E_D}{\Delta m}$$

where ΔE_D is the energy imparted by ionising radiation in volume element dV and Δm is the mass of material contained in that volume element. The criterion is that the volume element is chosen to be small enough for $\Delta E/\Delta m$ to be approximately constant and yet still be sufficiently large to be traversed by many particles and contain many interactions. Since these conditions cannot both be met simultaneously, the dose can only be found by averaging procedures represented by the symbol Δ . The absorbed dose can simply be termed "dose".

Energy deposition can also be measured as Kerma, which is the quotient of ΔE_k by Δm where ΔE_k is the sum of the initial kinetic energies of all the charged particles liberated by indirectly ionising particles in a volume element of the specified material (NBS 84, 1963). It differs from the absorbed dose which is the specific energy imparted by the charged secondaries. They are equal under conditions of charged particle equilibrium, i.e. when the energy imparted per unit mass is equal to the energy liberated per unit mass in the form of charged particles.

Kerma is equivalent to the concept of first collision dose defined in NBS 75 (1961). Attix (1965) has reviewed the meanings of first collision dose which has previously taken one of several forms,

- (a) first collision dose \equiv absorbed dose in an isolated small sphere (NBS 63, 1957),
- (b) first collision dose \equiv that part of the absorbed dose contributed by primary radiation only, in a small mass located anywhere (Hurst and Ritchie, 1962),
- (c) first collision dose \equiv kerma (NBS 75, 1961 and NBS 84, 1963).

The sensible definition of first collision dose emerges as that part of the absorbed dose at any point under charged particle equilibrium conditions, in a small mass of the specified material, and resulting only from 'primary' radiation, the source of any 'non-primary' radiation being identified in each case.

The magnitude of a biological effect arising from a given energy deposition by different processes was originally calculated by adopting an appropriate weighting factor known as the relative biological efficiency factor, (RBE), which was closely related to the specific ionisation of the ionising particles.

Radiobiologically the RBE was the inverse ratio of the doses required to produce equal effects, which depended on the biological effect, dose, dose rate and other factors. For Radiation Protection purposes a less variable factor was required. A new term called the quality factor was introduced for use in radiation protection and corrects for the difference in biological effect due to the variation in the LET. The linear energy transfer (LET) of charged particles in a medium is the average energy imparted locally to the medium by a charged particle of specified energy traversing unit distance.

The dose (D) is modified in radiation protection to give the 'dose equivalent' (DE) in rems which is numerically equal to the dose in rads multiplied by modifying factors such as the quality factor (QF) and distribution factor (DF).

$$(DE) = (D) \times (QF) \times (DF) \dots\dots$$

The advantage of the dose equivalent is that it gives some measure of the biological damage due to different radiations, and also the doses so expressed are additive.

§1.3 Survey of the Theories on Energy Deposition

A number of papers have been published on the calculation of the neutron tissue dose corresponding to exposure to a unit flux of neutrons with a given energy. The majority of the authors assume that a broad monoenergetic beam of neutrons is incident normally on the body which is represented by a homogeneous semi-infinite slab, 30 cm thick, having an atomic composition simulating that of soft tissue. Initially the main interest lay in determining the maximum permissible exposure to neutrons (Biram 1949, Capron 1949, Mitchell 1947(a) and 1947(b)). It was not until 1949 that Tait calculated the distribution of dose with depth for neutrons with energies between 0.5 and 5.0 Mev, followed by Snyder's theory in 1950 for the thermal neutron distribution. The latest and most complete work on the subject of energy deposition as a function of depth in tissue was produced by Snyder and Neufeld in 1955, which covered neutron energies up to 10 Mev. The only theory for neutrons with energies greater than 10 Mev and less than 20 Mev is that due to

Randolph (1957) which deals with the first collision dose in various media due to 14.1 Mev neutrons. Kogan et al (1959) have carried out extensive calculations in the intermediate energy region but as this is outwith the scope of this thesis it will not be discussed further.

In his calculations of the tolerance flux of thermal neutrons, Mitchell (1947(a)) assumed that the neutron distribution in the body could be represented as an exponential function of depth. The experimental data of Capron, Faes and Tavernier (1949) suggested that the distribution should in fact attain a peak at some depth within the body. This was confirmed by Snyder's theory (1950) in which he calculated the thermal neutron collision density as a function of depth. Snyder made two assumptions, namely that the neutrons are scattered isotropically in the laboratory system of co-ordinates and that their energy remains constant throughout their history. This is akin to neglecting the binding effects of the molecules on the cross-sections of individual elements, and neglecting the Maxwellian distribution of neutron energies. In 1955 Snyder and Neufeld extended the thermal dose calculations to include fast neutrons which had been thermalised, and it will be shown later (Chapters 3 and 4) that these assumptions may lead to an overestimation of the thermal peak distribution at depth.

The first collision dose treatment developed as more data on neutron cross-sections and anisotropic effects became known. It was originally assumed that the absorption cross-section was negligible compared to the elastic scattering cross-section, and that since most

of the dose for neutrons up to 10 Mev was due to the hydrogen present in tissue the inelastic scattering cross-section could be neglected. The elastic cross-section was therefore used in the calculations and assumed to be isotropic and equal to the total cross-section. The latest recommendations (NBS 88, 1963) allow for anisotropic elastic scattering but still neglect inelastic scattering. NBS 85 (1964) presents a table of kerma values in tissue for neutron energies ranging from 0.01 to 14.0 Mev calculated from the formula

$$D_i = 19.31 \times 10^{-7} \phi_n \frac{\epsilon K_i(\epsilon) \sigma_i(\epsilon)}{(1 + A_i)^2} \dots (1.1)$$

where D_i is the kerma in ergs/g,

ϕ_n = neutron fluence (n/cm^2),

ϵ_i = mean energy transferred in an elastic collision between a neutron of energy ϵ (Mev) and an atom of type i and is given by

$$\epsilon_i = \frac{2 A_i \epsilon \sigma_i(\epsilon) K_i(\epsilon)}{(1 + A_i)^2} ,$$

A_i = atomic weight of atom of type i ,

$\sigma_i(\epsilon)$ = total elastic scattering cross-section (barns/atom),

$$K_i(\epsilon) = \int_0^\pi [\sigma_i(\theta, \epsilon) / \sigma_i(\epsilon)] (1 - \cos \theta) 2\pi \sin \theta d\theta,$$

and $\sigma_i(\theta, \epsilon)$ = differential elastic scattering cross-section for neutrons scattered at angle θ (barns/steradian).

Kerma for any material can be found by multiplying equation (1.1) by the fractional atomic composition by weight for each type of atom and

summing the individual contributions.

The particular case of 14.1 Mev neutrons has been studied by Randolph (1957) who included the contribution to kerma from inelastic nuclear reactions and the asymmetric distribution of recoils from elastic scattering. The kerma calculated in this way yielded higher values of the dose for the carbon, nitrogen and oxygen elements exposed to 14.1 Mev neutrons than was obtained using equation (1.1) which neglected inelastic contributions. This is illustrated in Table 1.2 for the tissue composition corresponding to the Standard Man (hydrogen = 10%, carbon = 18%, nitrogen = 3.0% and oxygen = 65%, the other constituents contribute a negligible amount to the dose).

Table 1.2

Kerma for 14.1 Mev Neutrons

Method	Kerma, 10^{-7} ergs/g per n/cm^2				
	D_H	D_C	D_N	D_O	Total
Randolph	4.62	0.433	0.073	1.464	6.59
NBS 85	4.62	0.094	0.014	0.466	5.19

Inelastic reactions were found to contribute between 18 and 30% of the total dose in several hydrogenous materials which have been used to simulate tissue while the corresponding elastic reactions (i.e. with C, N and O) contributed less than 8%.

When the energy deposited at depth in a body of dimensions greater

than the mean free path of the incident neutrons is to be calculated, it is necessary to modify the first collision dose theory. In broad beam irradiation corrections must be applied to the dose for the attenuation of the primary flux, and for the increase in flux due to neutrons being scattered into the volume under consideration from collisions in surrounding tissue. The maximum permissible flux of fast neutrons was first estimated by Mitchell (1947(b)) who approximated the effect of backscatter on the surface dose by replacing the average energy lost per collision by $1 - e^{-\zeta}$ where ζ is the mean log energy decrement. This was improved on and extended to include the multi-collision dose at depth in tissue by Tait (1949) who derived the neutron density for a beam of monochromatic neutrons at normal incidence. Both Tait, and Biram (1949) who did the calculation for isotropic incidence, assumed that the mean free path of the neutrons remained constant in the tissue, and neglected the contribution to the dose from elements other than hydrogen. The latter approximation was rectified by Biram in 1962.

The most comprehensive treatment of multiple collision dose theory, which is currently accepted for radiation protection purposes, is due to Snyder and Neufeld (1955). They considered neutrons up to 10 Mev and derived the dose curves for the (n, p) and (n, γ) reactions due to fast neutrons which were thermalised, and also the curves for the recoil protons and heavy recoils. The case histories of 2,000 incident neutrons with 10 Mev energy were followed on a computer until their energy fell below 1 ev. Scattering was assumed to be isotropic in the

centre of mass systems, and inelastic scattering was neglected. The collision density of neutrons with a particular energy at any point could then be abstracted from the data compiled by the computer. To obtain reasonable statistics, energy groups of neutrons were chosen rather than a specific energy, and the energy of the group was taken as the mean energy. Snyder also showed that the ratio of the maximum multiple collision dose for a man to maximum first collision dose was 1.6 ± 0.2 for fast neutron energies from 0.5 to 10 Mev. (NBS 63, 1957)

§1.4 Techniques of Neutron Dosimetry

Dose measurements can be divided into two broad categories, (a) direct determination of the dose by measuring the energy absorbed, and (b) indirect determination of the dose via the neutron flux. The second method is of limited usefulness since equal neutron fluxes may give rise to varying tissue dose depending on the energies of the neutrons involved. In general, therefore, the neutron energy spectrum is also required.

The density of the secondary charged particles produced by neutrons in matter increases to a depth at least as great as their maximum range in the material. Beyond this point the number of secondaries that originate in any layer are approximately equal to the number terminating and charged particle equilibrium is said to exist. In general this requires that the linear dimensions of the mass be in excess of two maximum charged particle ranges. True radiation equilibrium is therefore not possible since the intensity of the primary beam gradually decreases by absorption and the density of the secondaries increase to the point

where charged particle equilibrium is first approached and then decrease at the same rate as the primary beam.

Before discussing the techniques used in neutron dosimetry it is appropriate to consider which 'dose' the instrument will measure i.e. kerma or absorbed dose. If, for example, radiation equilibrium can be approximated by using a tissue-equivalent ionisation chamber whose wall thickness is just greater than the maximum range of the secondary charged particles produced, then it will measure kerma for tissue in any medium. Where radiation equilibrium cannot be approximated then the dose determined is simply a mean dose to the tissue - equivalent gas in the chamber. Absorbed dose measurements need not be carried out under conditions of equilibrium since the object is to determine the energy locally absorbed rather than the energy locally lost from the incident radiation. A dosimeter fulfilling Bragg-Gray conditions (§1.4.4) located in a phantom filled with tissue-equivalent liquid measures the absorbed dose. Under conditions of charged particle equilibrium kerma equals the absorbed dose (Rossi 1965).

§1.4.1 Calorimetric Method

This is, in principle, a very direct method of measuring the dose absolutely provided corrections are applied to account for the energy absorbed or liberated in chemical reactions. The temperature rise expected in soft tissue irradiated by neutrons is very small amounting to an increase of the order of 2×10^{-8} °C per rad. A disadvantage is that the energy released by any γ -rays present will also be measured.

Although the error involved in estimating the corrections necessary due to chemical reactions is not much greater than that in W , the energy required to produce one ion pair in a gas, no calorimetric methods of neutron dosimetry have been reported in the literature.

§1.4.2 Spectral Measurements

For fast neutrons the energy absorbed per gram of the irradiated material can be calculated from equation (1.1) or from Snyder's data in NBS 63 (1957), provided the neutron energy spectrum is known.

If radiation equilibrium has been established the first collision dose (kerma) will be given by

$$D_f = \int_0^{\infty} n(E) D_f(E) dE$$

where $D_f(E) = \sum_i D_i(E)$ is the first collision dose for a neutron of energy E and $n(E)$ is the number of neutrons with energy E at the point in the medium where the dose is to be determined.

Similarly the absorbed dose can be found by weighting the mono-energetic data on multi-collisions in NBS 63. However, it is usually easier to find the absorbed dose directly by another method than to measure the neutron spectra. Some spectrometers are not suitable for use in phantoms.

For absorbed dose measurements high resolution is not essential which permits the use of threshold detectors and other low energy resolution detectors. The main advantage of such detectors is that they can be used with high intensity burst of neutrons where other

detectors cannot be used.

Hurst et al. (1956) described a method of measuring fast neutron (1 kev to 10 Mev) spectra using threshold detectors which consisted of discs of ^{239}Pu , ^{237}Np , ^{238}U and ^{32}S foil. A knowledge of the incident neutron direction is not required and also the method is suitable for use in a phantom. The ^{239}Pu was surrounded with 2.2 g cm^{-2} of ^{10}B to remove the thermal neutrons. The neutron fluxes above the threshold can be determined for each type of foil and a histogram constructed which gives the distribution of neutron energies in the intervals 1 kev to 0.75 Mev, from 0.75 Mev to 1.5 Mev, from 1.5 Mev to 2.5 Mev, and above 2.5 Mev. Originally Hurst calibrated the detectors against a thin disc of ^{239}Pu which had been irradiated by a known thermal flux. The fission product decay curves for ^{237}Np and ^{238}U were derived by a simple cross-section correction to the ^{239}Pu curve. Later data proved this to be incorrect. Johnson et al. (1965) improved the method by using a surface barrier detector irradiated by 14.8 Mev neutrons to calibrate the foils, and also experimentally determined the correct decay curves for the fission products. From the measured spectrum dose may be determined by the kerma curve (NBS 85, 1964) which gives

Dose =

$$\left[1.4 (\phi_{\text{Pu}} - \phi_{\text{Np}}) + 2.4 (\phi_{\text{Np}} - \phi_{\text{U}}) + 3.0 (\phi_{\text{U}} - \phi_{\text{S}}) + 3.8 (\phi_{\text{S}}) \right] \times 10^{-9} \text{ rads}$$

where ϕ_{Pu} , ϕ_{Np} , ϕ_{U} and ϕ_{S} are the neutron fluences above the threshold for ^{239}Pu , ^{237}Np , ^{238}U and ^{32}S respectively. The coefficients represent the average dose per neutron for the various energy regions weighted to a

fast fission spectrum of neutron energies. The method has an accuracy of $\pm 10\%$ and the advantage of excellent discrimination against γ -rays. The major limitation on its usefulness is that high neutron fluxes are required for activation. A second disadvantage is the crude spectrometry involved, particularly for neutrons in the intermediate energy range.

A second technique of interest was devised by Bramblett et al (1960) and further developed by Hankins (1961). Neutrons are detected in a $\text{LiI}(\text{Eu})$ crystal after moderation in polythene spheres of different diameters. The neutron spectrum shape can be deduced by observing count rates with the spheres providing these have been previously calibrated for monoenergetic neutrons over the energy range of interest. This technique has been used in an instrument capable of measuring the tissue equivalent dose rate of neutrons in the energy range thermal to 10 Mev. The response of the instrument, which utilises a 10 in. diameter polythene sphere and a 4 mm. diameter by 4 mm. thick $\text{LiI}(\text{Eu})$ crystal enriched to 96% in Li^6 , follows the inverse curve of the maximum permissible dose equivalent. The observed dose equivalent corresponds to within a few % at thermal energies, and to $\pm 15\%$ between 0.2 and 7.0 Mev. In the intermediate energy range, however, it overestimates the dose equivalent by a factor of 4 to 5, and at 0.1 ev by 50%. This could not be used in the present report since it was not adaptable to measurements in a phantom due to its large physical size and weight.

A complete survey of methods used in neutron flux measurements can

be found in NBS 72 (1960).

§1.4.3 Chemical and Photographic Dosimeters

The integrated dose can be measured using nuclear emulsions. If the hydrogen content of the emulsions is known the fast neutron dose can be evaluated by determining the number and length of recoil proton tracks per unit volume of emulsion. The most accurate results are obtained when the emulsion is analysed to determine the proton energy spectrum. This is very tedious and detection is limited to proton tracks between 0.15 Mev and 5 Mev, the lower limit being determined by the natural background and the upper limit by ease of track counting. Cheka (1953) developed a simplified device surrounding the emulsion with layers of tissue-equivalent material. The thickness was chosen such that the number of tracks produced in the emulsion per unit absorbed dose was independent of neutron energy. The disadvantage of such a detector is that the sensitivity to irradiation in the plane of the detector is only half that for normal incidence. Emulsion detectors are also subject to fading and shrinkage, and the fog produced by γ -ray exposure can seriously impair the visibility of proton tracks. Thermal neutrons may also produce spurious proton tracks via the $^{14}\text{N}(n, p)^{14}\text{C}$ reactions in the nitrogen present in the emulsion gelatine. This can be reduced by cadmium shielding provided the thermal dose is less than 20 rems, otherwise the cadmium capture gamma rays become a hazard.

The thermal neutron dose can be determined by measuring the increase in optical density by photo-electric means. Protons produced by the $^{14}\text{N}(n, p)^{14}\text{C}$ reaction produce a larger number of tracks per unit area

than the recoils from elastic scattering by fast neutrons. Alternatively the emulsions may be loaded with elements with large thermal neutron cross-sections such as lithium or boron, to increase the sensitivity by as much as a factor of 200 over ordinary emulsions.

Other dosimeters in this class which are more strictly chemical in origin than the nuclear emulsions are at present in an early stage of development. The Fricke dosimeter (NBS 75, 1961) is the only reliable chemical detector for routine use, and in general they are not suitable for total doses below 1,000 rads. Chemical dosimeters have an appreciable gamma ray sensitivity and the disadvantage that the relationship between the absorbed dose and the observable effect is non-linear. Also, they are not in general tissue-equivalent in response.

§1.4.4 Ionisation Devices

The total absorbed dose delivered by any ionising radiation may be determined using the Bragg-Gray relation. In 1912 Bragg related the ionisation in a gas-filled cavity irradiated with gamma rays to the electron stopping power of the wall materials and later Gray (1928) formulated the theory to give the Bragg-Gray Principle. When the cavity is sufficiently small the gas is subjected to the same flow of ionising particles as the material under consideration. The energy imparted per gram of material, E_m , is related to the number of ion pairs formed per gram of gas, J_g , by the Bragg-Gray equation

$$E_m = J_g W$$

where W = the average energy in ergs expended by the ionising particles

crossing the cavity per ion pair formed, and

S = the ratio of the mass stopping power of the solid to that of the gas for the ionising particles in question.

In the special case when the wall and gas have the same atomic composition, $S = 1$, the size and shape of the cavity are irrelevant providing the radiation field is constant in the region surrounding the collecting volume. Thus the energy imparted to unit mass of gas is directly proportional to the ionisation. The constant of proportionality W varies by only a few % depending on the nature and energy of the ionising particle. Detectors based on this condition will be discussed. In particular since the material in which the dose is to be determined is tissue, perturbation effects caused by the presence of the detector will largely be removed if the walls and gas of the chamber have the same atomic composition as tissue. Tissue-equivalent chambers which may be utilised over a wide range of interest have been discussed in detail by Rossi and Failla (1956). The wall material may be a conducting plastic where most of the oxygen present in tissue is replaced by carbon (Shonka et al 1958). If exact tissue-equivalent is required a gel can be used instead. The gas is composed of various gases to give the correct composition (Rossi, 1956). The error involved in using the plastic is less than 5% for neutron energies up to 14 Mev.

Dosimeters based on ionisation and the Bragg-Gray relation can conveniently be subdivided into two distinct groups,

(a) ionisation chambers, and

(b) proportional counters.

§1.4.4(a) Ionisation Chambers

Owing to the large contribution to the dose by the hydrogen content, the total energy absorbed by hydrogenous materials will be approximately proportional to the percentage hydrogen present and many dosimetric calculations and methods of measurement were based on this. In one of the first attempts to determine the absorbed dose Gray and Read (1939) compared the ionisation produced in a graphite chamber with that produced in geometrically similar chambers with walls of Aerion ($C_6 H_{4.4} O_{1.5}$), icing sugar (CH_2O), and paraffin wax (CH_2), which were filled with gas mixtures having the same atomic composition as the walls. The use of homogenous chambers having gas walls of identical composition is discussed in a review article by Marinelli (1953) who shows that they are really only suitable for uncontaminated neutron beams, i.e. no gamma radiation.

In general the most direct approach to the problem has been in the development of tissue-equivalent ionisation chambers which have been discussed in many papers by Rossi. The report by Rossi (1956) provides an excellent introduction to the concept of tissue-equivalence and the construction techniques required in the production of chambers having various sensitivities. Chambers have been designed which will operate for dose rates of less than one millirad per hour or as high as several thousand rads per minute. These chambers determine the total absorbed dose in tissue, and other instruments must be used to evaluate the relative proportions of the radiations making up this total dose. The

sensitivity to neutrons is 10% less than the sensitivity to gamma rays due to the difference in W for electrons and heavy particles.

The contribution from the inherent gamma rays in a mixed radiation field to the dose recorded by a tissue-equivalent chamber can be found using the paired chamber technique. A second chamber lined with carbon and filled with carbon dioxide gas is used to measure the absorbed dose delivered by the gamma rays. Such chambers will, however, have a certain sensitivity to neutron, k , which is a function of the neutron energy. The appropriate theory is discussed in NBS 85 from which it is shown that the separate doses can be evaluated from the equations

$$T = N + 1.04 G$$

$$C = kN + 1.04 G$$

where T and G represent the doses recorded by the tissue-equivalent and carbon chambers respectively, and N and G are the neutron and gamma tissue doses in rads. This technique becomes very inaccurate when the gamma dose exceeds the neutron dose by a factor of ten.

The separate components of the neutron dose, i.e. due to $^{14}\text{N}(n, p)$, ^{14}C and $^1\text{H}(n, \gamma)$ ^2D reactions, and elastic scatter, can be determined by using a third chamber from which the nitrogen content has been omitted. This chamber will not record the nitrogen dose and the carbon chamber will not record any significant capture gamma radiation since there is no hydrogen present. Consequently the magnitude of the three components can be determined from these three chambers. This method would be of no use in determining the separate components of absorbed dose at depth in

a phantom unless the incident neutron beam was pure, since it would be impossible to separate gamma rays from the ${}^1\text{H}(n, \gamma) {}^2\text{D}$ reaction scattered into the carbon chamber from the inherent gamma radiation in a mixed beam.

Similar schemes involving several ionisation chambers to separate neutron and gamma ray doses have been suggested by Gray (1940), Dainty (1950), Bretscher (1944), Marinelli (1953), and Sayeg et al (1958).

§1.4.4(b) Proportional Counters

If the dosimeter is designed to operate as a proportional counter, and pulse heights are summed rather than a current measurement, then pulses due to gamma rays can be rejected. The gas pressure and cavity dimensions can be chosen such that the pulses due to electrons are very much smaller than those from recoil protons. If the pulse height is proportional to the number of ion pairs formed then the method is equivalent to the ionisation chamber with the advantage that it is insensitive to gamma rays. To obtain proportionality between pulse height and number of ion pairs formed care must be taken to exclude gases with high electron attachment, also, the height of the pulse at the output of the linear amplifier must be independent of the recoil proton track orientation to the centre wire in the counter. The latter condition can be fulfilled by proper selection of the amplifier rise time and decay time (Hurst and Ritchie, 1953).

A polyethylene-ethylene proportional counter was designed by Hurst (1954) which contained an internal alpha source for calibration. The total dose is proportional to the summation of pulse heights which may be

measured directly using the electronic pulse integrator of Glass and Hurst (1952). The original design was modified by Wagner and Hurst (1958) to provide an absolute dosimeter which was not directional in response and incorporated a four stage binary circuit to sum the pulse heights. The lower limit of acceptable neutron energy was set by the discrimination required to suppress the response to gamma radiation.

§1.4.5 Special Counting Methods

Dosimeters in this group have the advantage that the energy absorbed in tissue can be obtained simply by counting the number of pulses produced in the detector. The detector materials need not necessarily simulate the medium for which the energy absorption is indicated since they are designed to have an energy response curve which approximates to the kerma curve.

Hurst et al (1951) developed a recoil proportional counter which would discriminate against gamma radiation. The energy response was adjusted by suitable gas filling and by inserting layers of hydrogenous material on the front wall of the counter to give a counting rate that was proportional to the dose delivered for neutrons with energies between 0.2 and 10 Mev. The lower limit was set by the bias required to suppress the response to gamma radiation. The main drawback was its directional response. A modified version was produced by Dennis and Loosemore (1957) which had a non-directional response. De Pangher and Roesch (1955) also developed a dosimeter suitable for the energy range 0.1 to 5.1 Mev which consisted of a BF_3 counter surrounded by a paraffin

moderator, with the neutrons incident normally to the axis of the cylinder. The size and directional properties make it unsuitable for depth dose measurements.

Scintillation techniques have also been employed. Skjöldebrand (1955) developed a spherical scintillation detector whose energy response was adjusted to Snyder's multiple collision absorbed dose curves. The disadvantages for use in a phantom were the large size and poor sensitivity. The Hornyak button (1952) was modified by Muckenthaler (1957) to respond to fast neutrons in a manner similar to kerma. Fast neutrons strike the hydrogenous material in the button and produce proton recoils which cause the ZnS to produce light pulses. The size and concentration of the ZnS particles were varied to produce the desired energy response. The thickness of the ZnS particles limits the accuracy of the detector due to absorption losses. The lower threshold is about 0.5 Mev proton energy for the smallest size of ZnS particles available.

The conclusion is that none of the methods discussed are suited to neutron depth dose measurements in a phantom with the possible exception of Bragg-Gray type tissue equivalent proportional counters. The major disadvantage of the latter is their relatively large size, since ideally the detector should cause the minimum perturbation of the neutron flux in the phantom, also it means that the position of the counter is restricted and measurements cannot be taken close to the phantom walls.

§1.5 Review of Experimental Dose Measurements

Despite the fact that Snyder and Neufeld computed depth dose curves

for multicollisions of monoenergetic neutron beams in tissue in 1955, it was not until 1961 that Smith and Boot produced experimental components of dose in a phantom for direct comparison with the theoretical values. Previous experimental data on Pu-Be and Po-B sources had been reported by Mills and Hurst (1954), and Barr and Hurst (1954), who used polyethylene-ethylene proportional counters to determine the total dose. The discriminating technique used to eliminate the inherent gamma rays also removed the gamma from the ${}^1\text{H}(n, \gamma) {}^2\text{D}$ reaction and part of the recoil dose which fell below the bias level.

Barr and Hurst used a Po-B source and assumed that the average energy of the neutrons was 2.5 Mev. They approximated to Snyder's infinite slab of tissue by a large cylindrical tank, 30 cm thick and 200 cm in diameter filled with tissue-equivalent liquid. The dose measurements were corrected for the 138 day half life of Po. Contribution to the total dose from neutrons scattered in the room was found to be negligible. When the dose measurements were compared to Snyder's for a 2.5 Mev beam, there was seen to be reasonable agreement. Mills and Hurst used a smaller phantom, comparable in size to the human head, and determined the total dose at depth for both a Po-B source and a Pu-Be source. The results in this case were not compared with theory. The data in both reports was analysed by the least squares method and fitted to a curve of the form

$$D_x = \frac{D_{\text{Be}} e^{-x/L}}{(R + x)^2}$$

where D_x is the dose rate at depth x in tissue, R is the separation between the source and phantom, and D is the first collision dose rate at 1 cm in air from the source, B is a factor to allow for the build up of the dose in the phantom, and L is the relaxation length. This expression can be re-written in the form

$$D_x = D_0 e^{-x/L}$$

where D_x is the absorbed dose per unit flux at depth x and D_0 is the corresponding value on the surface of the phantom. The main interest at this stage seems to have been in the determination of the build up factor to be applied to the dose recorded by a "first collision dose" dosimeter to give the true dose received by a man exposed to a neutron flux. The results indicated that the factor was a function of the phantom size.

Smith and Boot (1961) directed the first extensive search into the comparison of the dose received in tissue experimentally, with the theoretical curves of Snyder and Neufeld (1955), and Kogan et al (1959). Two phantoms were used in the experiment, the first, a 30 cm thick by 60 cm high and 60 cm wide slab, was used to approximate to the theoretical 'body', and the second was an elliptical cylinder, of axes 20 cm and 36 cm, and height 40 cm, to simulate the average body. The phantoms were again filled with tissue-equivalent liquid. A variety of mono-energetic neutron sources were used, 0.13 Mev, 0.5 Mev, 1.0 Mev, 2.5 Mev and 14.1 Mev, and also several sources having complex spectra, for example, Pu-Be and a fission source. Irradiations were made at a metre

or more from the source and the beam was incident normal to the front surface of the phantom. The thermal neutron flux density was measured at depth in the phantom using gold, manganese or sodium detectors. The $^{14}\text{N}(n, p) ^{14}\text{C}$ dose was then calculated simply by considering the nitrogen abundance in tissue, the cross-section of the reaction, and the energy released in the reaction. A major disadvantage of this method is that either the foils must be irradiated separately at each position of interest in the phantom, or alternatively all the foils may be placed in the phantom together and irradiated simultaneously which requires a correction to be applied to the measured flux to correct for the foils screening each other. Throughout the report all the absorbed doses were normalised to unit fast neutron flux incident on the phantom. The $^1\text{H}(n, \gamma) ^2\text{D}$ dose was calculated in a similar manner applying a formula due to Taylor (1954) to take account of the fact that γ -rays do not deposit their energy locally. The fast neutron recoil proton dose in the phantom was determined using nuclear emulsion detectors. The sensitivity of these detectors has been calculated by Cook (1958) and the mean of the sensitivities for normal and grazing incidence was assumed. The detectors were based on the type described by Cheka (1953) and were mounted at 45° to the incident beam to compensate for the change from a mainly unidirectional flux at the front of the phantom to a more isotropic flux deeper in the phantom. The emulsion detectors provide only a lower bound to the recoil proton dose. Smith and Boot suggest a method of calculating an upper bound which depends on the incident neutron spectrum

remaining virtually unchanged with depth in tissue. This assumption is given some support in a recent paper by Field (1965) who shows that neutron spectra do not change shape appreciably with depth in tissue to at least 25 cm. As an indication of the difference in magnitude between the lower and upper bound, for 2.5 Mev neutrons they differed by a factor of 2 at the front of the phantom increasing to 2.5 at the back of the phantom. The experimental results obtained shall be discussed and compared with the present work where appropriate.

This was followed in 1963 by two other reports on neutron depth dose measurements. Akagi and Lehman (1963) used a Pu-Be neutron source and Aceto and Churchill determined the dose for several (α , n) and (γ , n) sources. The report of Akagi and Lehman was mainly concerned with establishing how useful, or otherwise, nuclear emulsions are in determining the tissue dose from neutron exposure. The data presented from exposure of the emulsions, at various depths, in a tissue-equivalent phantom to Pu-Be neutrons included absolute differential energy spectra, average energy, and emulsion dose of proton tracks. The emulsions were exposed for sufficient time to contain at least 10^5 proton tracks. Hydrogen present in the emulsion served as an internal radiator and only tracks with both end points in the emulsions were recorded. A computer programme was formulated to calculate the proton recoil energy spectrum. The number of tracks in the energy range 0 to 0.66 Mev that were lost below the bias and by the sampling technique were estimated, and the average proton track energy was calculated, with and without, the (n, p) contribution. The $^{14}\text{N}(n, p)^{14}\text{C}$ dose was estimated by considering the ratio

of the nitrogen present in tissue to that present in the emulsion. Similarly the fast neutron proton dose was obtained by multiplying the emulsion dose by the appropriate factor for the ratio of the hydrogen densities.

The object of the study made by Aceto and Churchill was to determine the dose delivered as a function of depth by various point neutron sources of different energy spectra. The neutron source of direct interest to the present report was again a Pu-Be source. In all the dose measurements an inverse square correction was applied for the geometric divergence of the neutron flux. Scattering was minimised by performing the experiment outdoors and suspending the phantom 130 cm above the ground. The fast neutron energy measurements were made with a polyethylene lined proportional counter filled with different gases and adjusted to discriminate against gamma rays. The thickness of the polyethylene liner was chosen such that charged particle equilibrium was approached and therefore the fast neutron proton dose was easily obtainable from the total count rate and a knowledge of the energy spectrum of the neutron at the point in question, i.e. kerma = absorbed dose, except near the surface of the phantom. The tissue-dose components due to the $^{14}\text{N}(n, p) ^{14}\text{C}$ and $^1\text{H}(n, \gamma) ^2\text{D}$ reactions were calculated directly from the thermal neutron flux, which was measured with indium foils and checked with a BF_3 detector, in the same way as Smith and Boot. The dose values obtained were in good agreement with Snyder, and Smith and Boot.

The absorbed dose deposited at depth in tissue due to irradiation by

14 Mev neutrons has not been widely studied. The literature to date consists of one report by Blosser and Freestone (1963) in which they discuss the absorbed dose deposited in a water-filled spherical phantom due to 14 Mev and Po-Be neutrons. In both cases γ -rays are associated with the neutron emission and the dose rate from the γ -rays was determined with a detector described by Wagner and Hurst (1961). The neutron flux from the DT 14 Mev source was measured using aluminium foil and the $^{27}\text{Al}(n, \alpha) ^{24}\text{Na}$ threshold reaction. An ethylene filled ionisation chamber was used to determine the dose in the phantom, and by subtraction of the γ -dose the neutron dose at depth, corrected for inverse square distance of source and detector, was obtained.

Lawrence (1962) produced an interesting report describing the method he used to calculate the emission rate of a Pu-Be source from a knowledge of the dose rate delivered to an assumed standard tissue $(\text{CH}_7 \text{O}_3)_n$ by the fast neutrons and γ -rays emitted from the source. An ethylene-filled polyethylene counter was used to determine the total dose and a carbon dioxide-filled teflon ionisation chamber measured the gamma dose. The emission rate was then calculated from the neutron dose rate and the neutron spectrum shape of Stewart (1955). Excellent agreement was obtained with the currently accepted value at that time of 1.6×10^6 n/sec per curie.

More recently Jones et al (1965) compared calculated and experimental values for kerma in tissue produced by Pu-Be and Po-Be neutron sources. The experimental values were obtained using a cyclopropane-

filled proportional counter and found to agree with the calculated values. For the Pu-Be source, which is the source of interest in this report, the kerma was found to be 3.9×10^{-9} rads per n/cm² for tissue in air.

§1.6 Dose Equivalent

The biological effect of a given absorbed dose depends on the type of radiation involved. In general it may be simply obtained by multiplying the dose in rads by the appropriate quality factor and the product is the dose equivalent in rems. Until 1957 recommended values for the quality factors could be obtained from NBS 59 (1954). The quality factor was taken to be 1 for all LET values up to 3.5 keV/ μ after which it was assumed to increase almost linearly from 1 to 20 in the range 3.5 to 175 keV/ μ , beyond which it remained constant with the value of 20. In 1957 NBS 63 was published which contained quality factors calculated by Snyder. The quality factor for the total dose deposited was obtained by weighting the quality factors for γ -rays, heavy recoils and recoil protons by the appropriate dose fraction. Quality factor values were calculated as a function of depth in the tissue for various incident neutron energies on the basis that the quality factor for γ -rays was 1, for heavy recoils 20, and that for recoil protons it remained constant with depth being equal to the surface value. This is tantamount to assuming that the incident neutron beam spectrum shape does not change with the depth in the phantom. Table 1.3 lists the quality factors for a selection of neutron energies. These values, taken from NBS 63, are

currently accepted for the purpose of radiation protection.

Table 1.3

Quality Factors for Monoenergetic Neutrons

Neutron Energy Mev	Quality Factor
Thermal	3
0.005	2.5
0.02	5
0.1	8
0.5	10
1.0	10.5
2.5	8
5.0	7
7.5	7
10	6.5

No experimental evidence was found in the literature of dose equivalent curves for comparison with the theory of Snyder although attempts have been made to determine dose average LET'S from which the quality factors can be calculated (Rossi 1955, Conger et al 1958, Randolph 1964). These shall be compared later with the quality factors measured in this report.

§1.7 Distribution of Absorbed Dose as a Function of Linear Energy

Transfer

Calculation of the absorbed dose is only the first step in dosimetry.

The energy absorbed must then be analysed to determine its distribution as a function of LET. Since this aspect of neutron dosimetry has not been extensively investigated the present discussion shall be limited to an introduction to the concept which will be considered in more detail in Chapter 5.

Boag (1954) calculated LET spectra for the proton component from fast neutrons absorbed in water. More recently Snyder (1963 and 1964) has attempted to find the LET spectrum of dose from monoenergetic beams of neutrons incident on tissue cylinders simulating a mouse, guinea pig, dog and man. The Monte Carlo code used at present does not include inelastic scattering, but will allow for anisotropy of scattering with carbon, nitrogen and oxygen atoms. The method is still at the preliminary stage, but it is hoped in the near future to produce detailed information on the LET distribution of dose. Hurst (1956) and Randolph (1964) give equations for deriving average LET's from a kerma LET spectrum. Ideally, to derive average LET's and hence quality factors, the contributions by all elements and all reactions in the tissue concerned should be considered. As an example Conger et al (1958) find that for 14.1 Mev neutrons the energy average LET in tissue is $75.1 \text{ kev}/\mu$ when all the contributions are taken into account, but it is only $16 \text{ kev}/\mu$ for the recoil protons.

There are two ways of plotting the LET,

- (a) as the proportion of the total absorbed energy which is dissipated in each interval of LET, and

(b) as the proportion of the total track length belonging to each interval of LET.

At present only one method has been developed to measure the LET spectrum of dose. The detector was a spherical proportional counter of tissue equivalent plastic. The operating principles and design of the instruments were reported by Rossi and Rosenzweig (1955a), and experimental data (1956b) was produced and compared with Boag's theoretical curves. The counter was filled with tissue-equivalent gas at low pressure such that the particle spectrum set up in the wall was the same as the one occurring in tissue. Pulses produced by the counter can be sorted according to height and since the pulse distribution is predictable, only the relative number of maximum pulses corresponding to a given specific ionisation need be known. The total dose within any range of specific ionisation can be determined by a measurement of a limited portion of the pulse spectrum. The analysis assumed that the ionising particles traverse the cavity in straight lines, that particles traversing the cavity incur small change in LET, and that W (the average energy required to produce an ion pair) is independent of the nature and energy of the ionising particles and is the same for the medium in solid or gaseous state. The counter is insensitive to electrons and is inaccurate for neutron energies below 200 kev. Spectra obtained with the counter depend on the gas pressure used due to statistical variations of energy loss of charged secondaries, i.e. the LET spectra depend on the size of the biological sample under consideration (Rosenzweig and Rossi, 1959).

The device is at present limited to dose rates of less than 0.5 rad/hour.

The proportional counter is difficult to operate in practice and the results must be analysed by differentiating a differential spectrum. Its large size makes it unsuitable for depth dose measurements.

§1.8 Conclusions

When this research programme commenced in 1962 very little work had been done on the comparison between the measured absorbed dose values at depth in tissue and the theoretical curves of Snyder and Neufeld (1955) on which radiation protection factors were based. Neutron generators producing DD and DT neutrons, and Pu-Be alloy sources were rapidly establishing popularity for general use in laboratories without any extensive investigation having been carried out of the absorbed dose that could be received by a person exposed to the neutrons. It was also felt that some standard neutron facility was desirable which could be used by Radiobiologists for reproducible irradiation conditions. The physical dose data obtained in this report could then be used to advantage by persons experimenting under identical conditions. Further a knowledge of the quality factor and dose curves at depth for a phantom irradiated by neutrons has direct application in the estimation of the dose received by a radiation worker exposed to the neutrons provided his surface dose is known.

The later depth dose measurements of Aceto and Churchill (1963) and Akagi and Lehman (1963), on Pu-Be sources, were not sufficiently accurate due to the detection methods used to confirm or deny the accuracy of

Snyder's theoretical dose calculations. The experimental techniques for determining the dose components at depth in a phantom have favoured the use of nuclear emulsions to determine the recoil proton dose, and the activation of foils to determine the thermal neutron component. Smith and Boot, however, were unable to resolve a 24% decrease in the flux when measured using nuclear detectors to that obtained with a long counter, which left some uncertainty in the calibration of the emulsion detector. Akagi and Lehman appear to have underestimated the recoil proton dose which could be due to the scanning technique used which discriminated against short tracks, and although a correction was applied it may not have been sufficient particularly near the front of the phantom.

There was only one method available for measuring the dose as a function of LET (Rossi and Rosenzweig 1955(a)) which was restricted to the first collision dose and which relied on a complicated method of analysis of data obtained from a proportional counter difficult to operate in practice.

It was decided therefore to use scintillation techniques to measure the components of absorbed dose, and to expose the phantom to collimated beams of incident neutrons from a shield specially designed to minimise scattering from the room and to provide a standard neutron facility.

A Bragg-Gray type detector, made from NE 102 plastic phosphor and polyvinyltoluene sheet, was used to measure the recoil proton absorbed dose from the fast neutrons. The NE 102 phosphor was selected because:-

(a) it is a solid with similar atomic composition to soft tissue,

- (b) there is no problem about electrical conductivity of ionisation chambers,
- (c) γ -rays and heavy recoils can be discriminated against,
- (d) a knowledge of W , the energy required to produce an ion pair is not required,
- (e) the detector can be made very small in size.

It was felt that these combined properties made the detector particularly suited to the problem. The thermal neutron flux produced when the fast neutrons were moderated by the tissue was measured with a $\text{LiI}(\text{Eu})$ crystal and correction factors were applied for flux depression. Absorbed doses were measured at depth in the phantom for beams incident on both the major and minor axes of an elliptical phantom. The Bragg-Gray detector also provided a means of estimating the quality factor for the neutrons for radiation protection purposes, and hence the dose equivalent. Finally the detector was used to determine the recoil proton absorbed dose as a function of LET at depth in tissue.

CHAPTER TWO

NEUTRON FACILITIES FOR DOSIMETRY STUDIES

§2.1 Introduction

Neutron dosimetry is complicated by the poor detection sensitivity of existing measuring instruments. Both the sensitivity of the detector and the biological damage are dependent on the incident neutron energy, and hence spectrum shape of the incident radiation. An ideal detector would have an energy response directly related to the tissue dose which avoids the need to know the spectrum shape. (Anderson and Braum, 1964).

Neutrons have been classified according to their energy into thermal, intermediate, fast and relativistic groups. Since it has not yet been possible to match the response of one detector to neutron dose over the whole energy range, several detecting instruments must be used. This also allows measurement of individual contributions to the total dose. Theoretical and experimental measurements of energy deposition for monoenergetic and polyenergetic systems with energies up to 14.1 Mev will be compared.

Free neutrons do not occur in nature due to their short lifetime but they can be artificially produced by various methods. For neutron production, the light nuclei play the predominant role since very high energies are required due to the strong Coulomb barrier, before charged particles can react with heavy nuclei.

A neutron generator was used to produce monoenergetic neutrons by the $^2\text{H}(d,n)^3\text{He}$ and $^3\text{H}(d,n)^4\text{He}$ reactions which are particularly suitable because:-

- (a) the energy as a function of angle of emergence is known,
- (b) the energy range of a fission spectrum can be covered,
- (c) due to increasing use of generators employing these reactions it is essential to know more about the energy deposition in tissue when irradiated by DD or DT neutrons,
- (d) they allow direct comparison with theoretical values (cf. the polyenergetic spectra where the theoretical curves must be weighted for the spectrum shape),
- (e) large neutron fluxes are available.

The choice of the polyenergetic system was not so easy. All crystal and gas filled counters designed for neutron detection have varying degrees of γ -ray sensitivity. One of the main difficulties in neutron dosimetry is the separation of the effects from γ -rays and from neutrons. Since most sources of neutrons have associated γ -ray backgrounds e.g. from de-excitation of short-lived isotopes and fission products in reactors, induced γ -radiation by neutron capture, careful consideration had to be given to the choice of a neutron source with a minimum γ -ray background.

A suitable neutron source should fulfil the following conditions:-

- (1) there must be a low γ -ray output associated with the source,
- (2) a fast neutron output which is constant with time over, at least, several months, to eliminate frequent correction and normalisation of results,
- (3) the neutron intensity must be sufficiently large to provide good

counting statistics in the neutron detector,
 (4) the neutron spectrum shape should be well known.

Considerations of the above requirements led to the decision to use an (α , n) type neutron source. The other type of sources, e.g. (γ , n), spontaneous fission, accelerators and reactors, were rejected for one or more of the above reasons. The Be(α , n) reaction gives the highest neutron emission rate e.g. B(α , n) or O^{18} (α , n) reactions give approximately one third the yield of the Be(α , n) reaction. Table 2.1 shows details of the available Be(α , n) sources.

Table 2.1

Data on (α , n) Neutron Sources

Source	Half-Life	Maximum neutron energy (Mev)	Average neutron energy (Mev)	Yield n.sec ⁻¹ per curie	γ -dose MR.h ⁻¹ per 100 n.sec ⁻¹	Cost per curie
²²⁷ Ac-Be	22 y	11.79	4.6	1.8×10^7	8	£10,500
²⁴¹ Am-Be	458 y	11.10	4.6	2.7×10^8	< 0.1	Only small sources are available
²¹⁰ Pb-Be	21 y	-	-	2.3×10^6	8.8	£10,000
²¹⁰ Po-Be	138.4 d	10.87	4.2	2.5×10^6	0.04	£80
²³⁹ Pu-Be	24,400 y	10.74	4.5	1.4×10^8	1.7	£300 (£840)
²²⁶ Ra-Be	1,620 y	13.08	3.9	1.3×10^7	60	£300 + £250 annual hire charge
²²⁸ Th-Be	1.91 y	-	-	2.5×10^7	30	£850

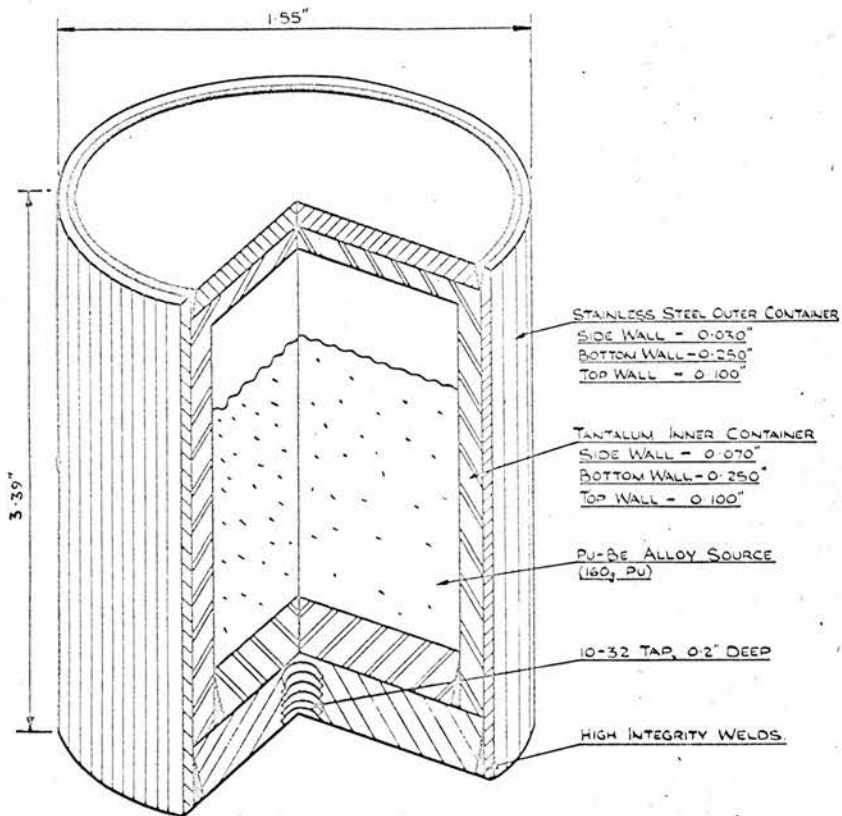


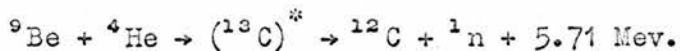
Fig. 2.1. Standard plutonium-beryllium neutron source.

§2.2 Pu-Be Facility

It was decided that the neutron output would have to be greater than 10^7 n/sec to satisfy condition (3). A survey of γ -dose rates in table 2.1 shows that the most suitable sources are ^{241}Am and ^{239}Pu . ^{210}Po has a comparatively short half-life; it would therefore require renewal and was not considered further. To satisfy the neutron intensity conditions, a 10 curie source of either ^{241}Am or ^{239}Pu was required. This ruled out ^{241}Am on the grounds of cost and availability, leaving ^{239}Pu as the only suitable choice. The associated γ -radiation is predominantly low energy and is almost completely removed by $1/32$ in. thick lead.

A 10 curie Pu-Be source was purchased[†], (Fig. 2.1) which consisted of 160 g of plutonium alloyed with beryllium metal and sealed in a stainless steel container (0.030 in. wall) having a tantalum metal liner with 0.070 in. wall. The source is 1.55 in. diameter by 3.39 in. long and has a nominal yield of 1.4×10^7 n/sec. Such a yield with mean neutron energy of 4.5 Mev would give about 10^{-4} rad/min in muscle tissue at a distance of 1 metre.

Neutrons are formed by the reaction



The high neutron yield is due to weak binding of the neutron in the ${}^{13}\text{C}$

[†]Pu-Be sources are not obtainable in the United Kingdom but can be bought under Licence in the U.S.A. from Nuclear Materials and Equipment Corporation (NUMEC), Apollo, Pennsylvania. The licence can be obtained by arrangement with the U.S. Atomic Energy Commission, Director, Division of International Affairs, Washington 25, D.C.

compound nucleus which decays to ^{12}C a very stable three alpha particle nucleus. The (α, n) type of source has the disadvantage of emitting a spectrum of energies, but provided the spectrum shape is known the theoretical results can be integrated from the data for monoenergetic beams to provide the results for the spectrum and allow direct comparison with the experimental values. The continuous spectra is due to the slowing down by ionisation loss in the source material of the α -particles producing the reaction, and also the ^{12}C nucleus can be left in the ground state, or the 4.43 and 7.66 Mev excited states.

Several authors have published experimental and theoretical Pu-Be spectra (Anderson 1963, Broek 1960, Hess 1959, Huber 1962, Lewandowski 1961, Stewart 1955). The spectra shape used in this report is that of Stewart (1955). More recent publications, however, have shown the existence of a large number of low energy neutrons below the lower limit of Stewart's results. De Pangher (1959) predicted a variation in the number of low energy neutrons on the basis of double moderator ratios for various sized Pu-Be sources. As the source size increases there are more neutrons produced by fission of the ^{239}Pu , and by the $(n, 2n)$ reaction and elastic scattering with ^9Be . St. Romain (1962) also reported the possibility of inelastic scattering of alphas by ^9Be , leaving the ^9Be in the 1.75 Mev excited state which decayed by neutron emission. These neutrons peak about 0.3 Mev. Present data indicates that 15% of the total number of neutrons lie below 1.0 Mev., (Anderson 1963, Geiger 1964, St. Romain 1962), and for a large 80 g Pu-Be source

Heertje (1964) suggests that this figure could be as high as 25%. This is considerably more than the 9% predicted by Stewart and is important in determining the average energy of the Pu-Be source (Chapter 3, §3.6.2).

§2.2.1 Selection of Shielding Material

The shielding was designed with the object of producing pure well collimated beams with a minimum of scattered neutrons. Capture γ -rays resulting from (n, γ) events in the shield were minimised by choosing materials with small (n, γ) cross-sections. Such material also required good neutron slowing-down and absorption properties. Polythene loaded with boron met these requirements since polythene is an efficient moderating medium, and although the hydrogen had an (n, γ) cross-section of 0.34 barns at thermal energies producing a 2.23 Mev γ -ray, the γ -ray intensity was greatly reduced by adding 10% by weight of boric oxide. Boron-10, which has a cross-section of 3840 barns for the (n, α) reaction, served the dual purpose of preventing the thermalised neutrons leaking through the shield and of limiting γ -ray production. Only 1% of the neutrons were absorbed in the hydrogen, the remainder being absorbed in the boron.

A further concern was the γ -emission from the source itself. Polythene is less efficient than lead for attenuating γ -rays below 500 keV, but above 500 keV polythene becomes more efficient for an equivalent mass of shielding. Karama and Wetherington (1960) measured the γ -ray shielding properties of polythene and lead mixtures and concluded that for a shield containing more than 17 g/cm² of polythene

the attenuation of the combination with lead becomes less than for all lead. For 3 to 17 g/cm² of polythene plus any thickness of lead, the combination provides better attenuation than the same mass equivalent of either material. It follows that polythene loaded with lead powder (Densithene) can be a very efficient γ -ray shield. This shielding material also has good neutron-shielding properties and few (n, γ) events occur since ²⁰⁸Pb is a nuclide with completely filled neutron and proton shells, and has, therefore, a very low capture cross-section (viz. 5×10^{-4} barns).

The mass absorption coefficient for the attenuation of γ -rays for the combination is given by:

$$\mu = \frac{1}{x_1 \rho_1 + x_2 \rho_2} \log I_0/I_1$$

where I_0 is the intensity of the incident radiation, I_1 is the shielded intensity and $x_1 \rho_1, x_2 \rho_2$ are the areal densities for polythene and lead respectively.

These considerations led to the conclusion that the addition of boron to Densithene would yield an excellent shielding material in close proximity to the source. Blocks of this material were prepared to the specification (5 parts lead to 1 part polythene by weight plus 10% boric oxide).

§2.2.2 Design of Shield

The Pu-Be source was mounted on an aluminium platform which could be raised and lowered by a chain drive into a 2 ft. deep recess in the concrete floor, the idea being that the source could be shielded safely

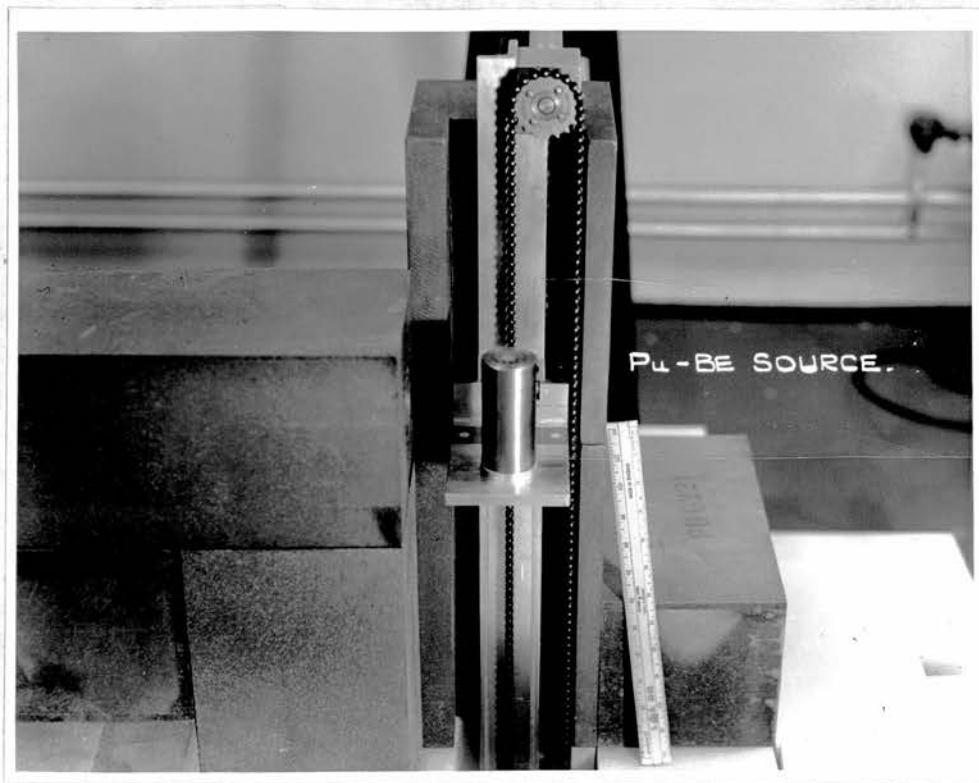


Fig. 2.2(a) Photograph of Neutron Source.

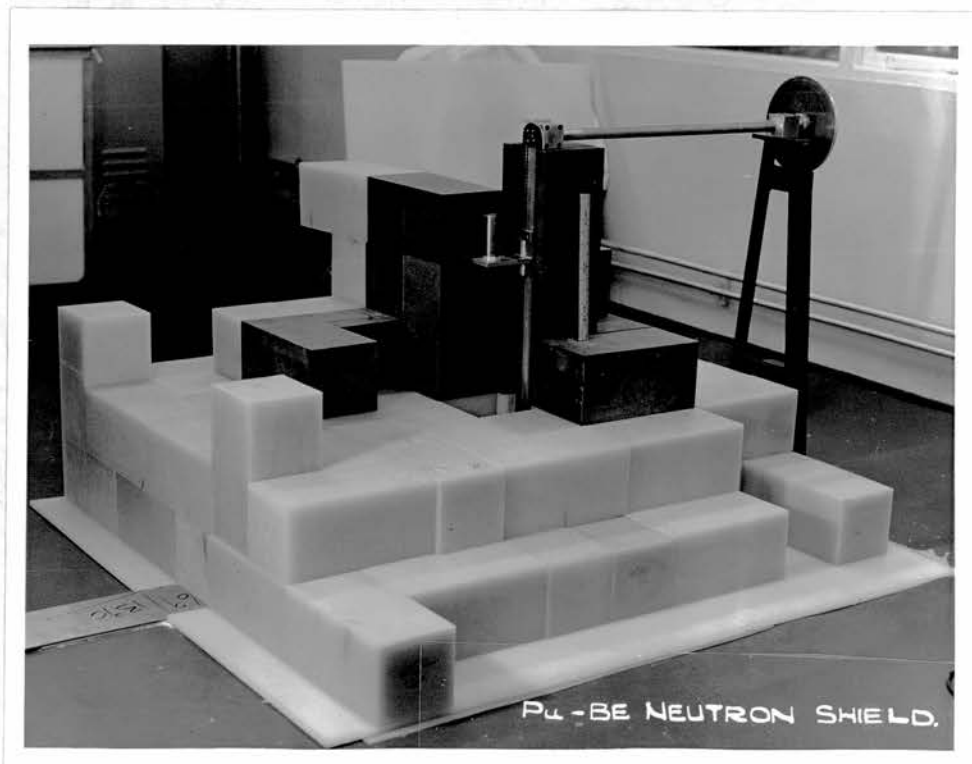


Fig. 2.2(b) Photograph of Neutron Shield.

in the recess if it was desired to make modifications to the shielding arrangement for new experiments. Versatility of the shielding arrangement was obtained by making the shielding bricks size $6 \times 6 \times 12$ in. With this design the bricks could be criss-crossed to minimize leakage paths through the shield. Fig. 2.2(a) shows a close-up of the neutron source mounted on the platform and Fig. 2.2(b) shows the partially completed shield. The final form of the shield was a cube as shown in the schematic diagram in Fig. 3.1. When the source was in position the neutrons had to pass through 1 ft thick Densithene and 1 ft thick polythene to escape.

The brick protruding from the left-hand side of the shield in Fig. 2.2(b) could be moved on an aluminium slider to cover the source after it was lowered into the floor recess, reducing streaming and permitting alterations to the shield to be made in safety.

The shield was constructed to permit two (one horizontal and one vertical) collimated beams of neutrons to be used. The bricks containing the collimators could be adjusted to give any size of beam up to a 6 in. square beam. The standard sizes used were a 2 in. diameter and a 6 in. square beam.

§2.2.3 Performance of the Shield

The Pu-Be neutron source was calibrated by the standard manganous sulphate bath technique in which the 2.5 hr ^{56}Mn isotope was activated and counted (N.B.S. Handbook 1960). When corrected for the geometry subtended by the collimator at the source it was found that the 2 in.

beam emitted a flux of $5.30 \times 10^2 \text{ n cm}^{-2} \text{ sec}^{-1}$. A direct measurement of the fast flux was also made using a plastic phosphor (type NE 102) 4.45 cm diameter and 0.64 cm thick. The neutron detection efficiency was calculated assuming the Pu-Be spectrum shape of Stewart (1955) and weighting each energy band by the hydrogen scattering cross-section. A net $\sigma_H = 2.44$ barns was obtained and the detection efficiency calculated to be 7.8%.

The efficiency of the phosphor is defined as the ratio of the number of recoil protons to the number of incident neutrons. It has been found for the largest and smallest size of phosphor used in this report that the efficiency calculated on the basis of carbon and hydrogen scattering was nearly the same as the efficiency calculated on the assumption that carbon does not scatter neutrons at all. The efficiency of all the NE 102 phosphor discs used was therefore calculated from

$$\epsilon(E_0, t) = 1 - \exp(-n_H \sigma_H t)$$

where $\epsilon(E_0, t)$ is the efficiency of a phosphor of thickness t to a flux of monoenergetic neutrons energy E_0 ; n_H is the number of hydrogen atoms per cc in the phosphor and σ_H is the neutron-proton scattering cross-section at neutron energy E_0 .

Correction had to be made to the flux measurements for the attenuation of neutrons in a $1/4$ in. thick sheet of lead which was inserted in the collimator to remove any γ -rays emerging from the source. The attenuation of neutrons was about 7% of the total compared to almost 99%

of the γ -rays.

The response of the NE 102 phosphor to γ -rays occurs by the Compton effect. The maximum pulse height produced by the γ -rays is limited by the phosphor dimensions. The $1/4$ in. thick phosphor is capable of stopping 1 Mev electrons which produce pulses of the same height as 3 Mev protons. Experiment indicated, however, that the background due to gamma rays was negligible. Count rates were therefore recorded for different operating voltages and discriminator bias levels and extrapolated to zero bias to yield a total flux of 5.44×10^2 n cm⁻² sec⁻¹ for the 2 in. diameter collimated beam.

A series of simple experiments were designed to evaluate (1) leakage through the shielding and (2) the presence of thermal neutrons in the collimated 2 in. beam. A LiI thermal neutron detector was placed in front of the collimator exit, and count rates were recorded with and without a 0.030 in. thick cadmium metal sheet placed over the aperture from which it was deduced that there was a thermal neutron contribution of less than 0.1% to the total fast flux.

When the whole front face of the shield was covered with cadmium foil the count rate was less than 1% lower than that observed when only the collimator was covered. It was concluded that there was no appreciable thermal neutron leakage through the shield and, by implication, a negligible fast neutron leakage, since neutrons should be predominantly of thermal energies after passing through the moderating medium.

Measurements were made of the beam profile using a plastic phosphor

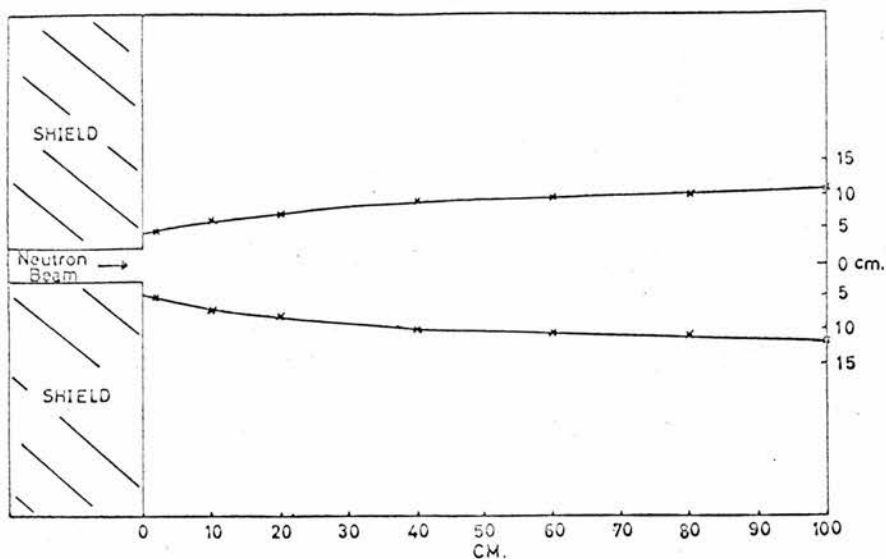


Fig. 2.3. Profile of the fast neutron beam from the collimator. The beam has an intensity of 10% maximum along the contour.

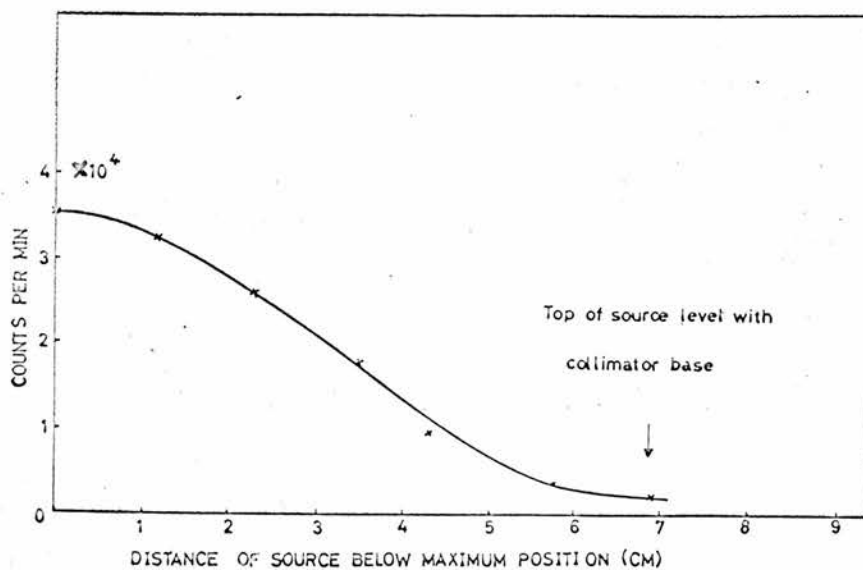


Fig. 2.4. The observed flux at the collimator exit is plotted against the distance, the top of the source holder is lowered below the maximum position.

detector. Count rates were observed at measured intervals along the axis of the collimator up to 100 cm distance from the shield and also at distance along the normal to the beam. All count rates were corrected to zero bias level. Fig. 2.3 shows the beam bounded by a contour at which the neutron intensity falls to 10% of the value observed on the axis.

The results showed that the intensity along the axis fell off more rapidly than predicted from the inverse square law. The extra reduction in beam intensity was 0.21%/cm in the 100 cm distance from the collimator exit, but the average reduction was only 0.14%/cm over the last 65 cm. This indicated that there was some small degree of scattering from the collimator walls and, therefore, the neutron flux observed at the collimator exit would be enhanced slightly above the value calculated from the solid angle and the total source yield.

As a further test on the effectiveness of the shield, the neutron flux at the collimator exit was observed when the source was lowered gradually. The results shown in Fig. 2.4 indicated that the flux observed when the top of the source was level with the bottom of the collimator tube was only 6% of the maximum intensity. Probably most of this count rate was caused by scattering from the collimator walls.

§2.3 Monoenergetic Neutrons by the DD and DT Reactions

§2.3.1 Method of Neutron Production

Monoenergetic DD and DT neutrons were produced using a medium stability Sames \pm 600 K.V. Electrostatic Generator which can produce a beam current of 1 mA.

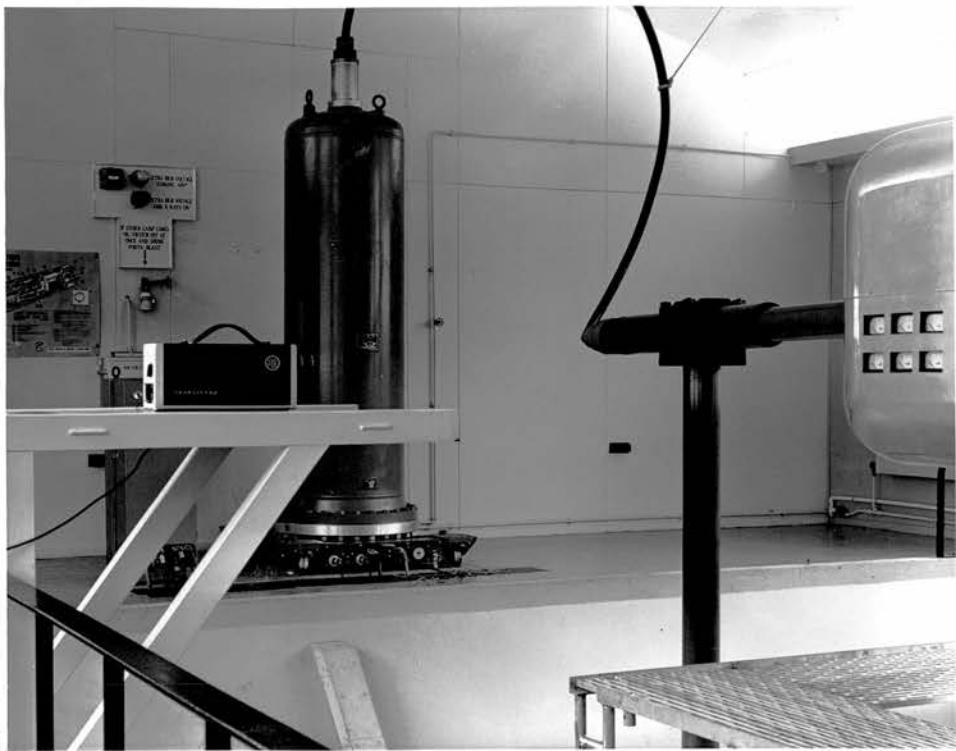


Fig. 2.5 Photograph of the 600 KV Electrostatic Generator.

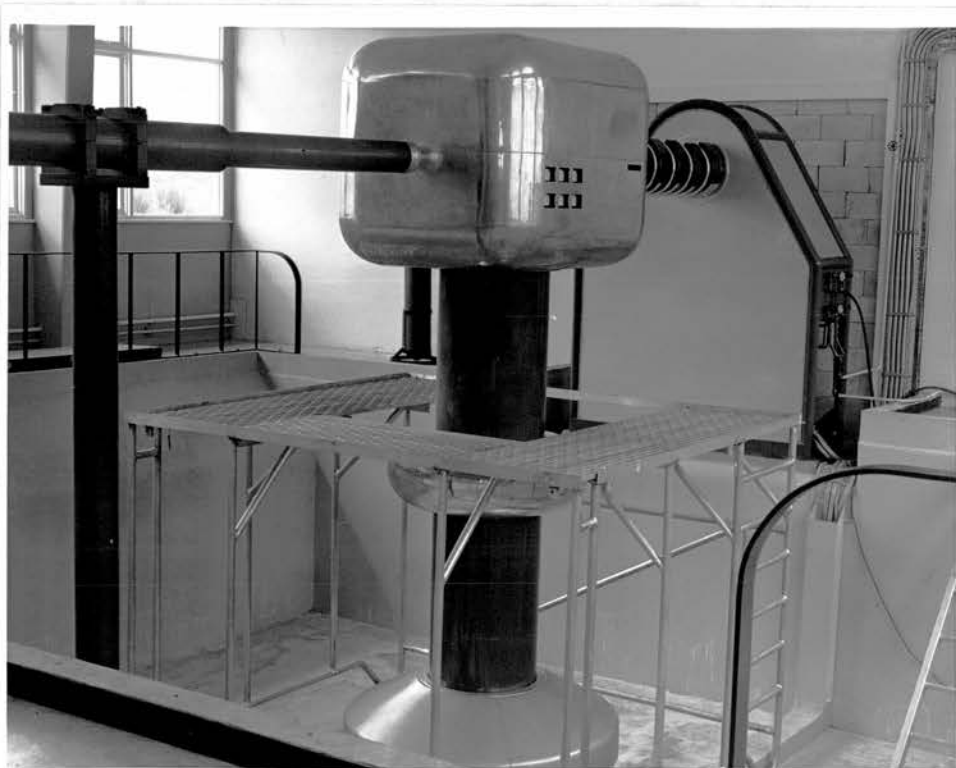


Fig. 2.6 Photograph of the Particle Accelerator.

The neutron generator consists essentially of two sections, an electrostatic generator to produce the high voltage (Fig. 2.5) and the accelerator (Fig. 2.6) where the plasma of hydrogen or deuterium ions is formed and accelerated down a beam tube to impinge on a nuclear target of deuterium or tritium gas.

The high voltage is produced in the cylindrical vessel which is hermetically sealed and contains all the high voltage elements of the generator in a gas of high dielectric strength. Production of the 600 K.V. follows the Van de Graff principle. Since the commutation takes place by ionisation there is no mechanical contact to cause friction. A small auxiliary 30 K.V. generator supplies the necessary excitation voltage. The 600 K.V. is fed via a damping resistor to the H.T. terminal of the accelerator i.e. aluminium 'bun'.

The plasma is formed by allowing the gas to pass through a palladium 'leak' tube, from a reservoir contained in the bun, into the ion tube and exciting the gas with 100 mc/s R.F. signals. The positive ions are then extracted from the ion tube by ~ 6 K.V. applied to a tungsten probe and focussed through an aluminium canal by an axial magnetic field. During the operation, a closed circuit television was used to monitor the plasma and meters on the bun. The monitor was placed on the control console in the room adjacent to the generator.

The ions are then accelerated down the evacuated beam tube, which has a uniform field maintained by a chain of 325 megohm araldite-encased resistors, and through a one metre long drift tube to the target.

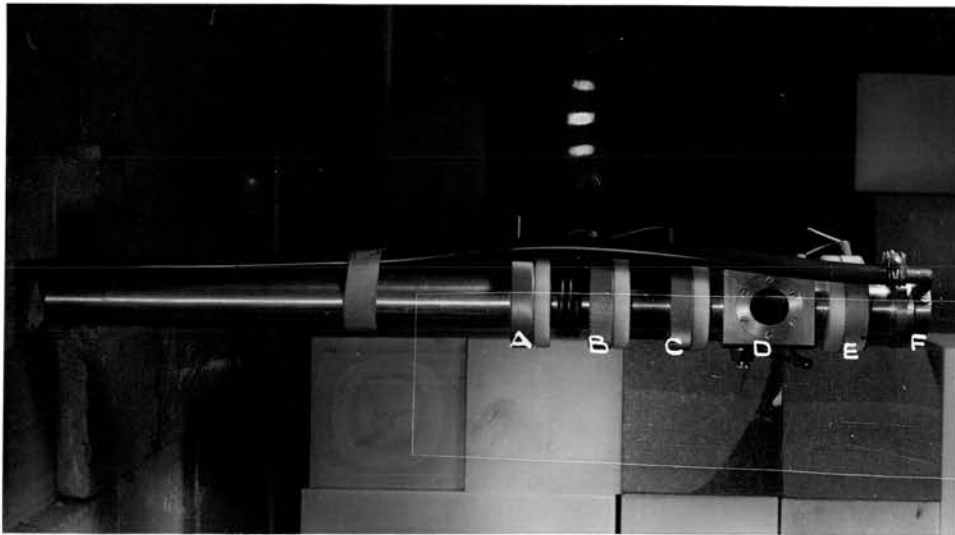


Fig. 2.7 Photograph of the Target System.

- A Diaphragm.
- B Diaphragm.
- C Electron Suppressor.
- D Quartz-Window Viewing Chamber.
- E Electrode for Target Current Measurement.
- F Target Holder.

The source of neutrons i.e. target, is enclosed in a shield similar to that already described, and is in the control room. The maximum ion current is 1 mA and provides continuous beam operation for protons or deuterons. The maximum beam diameter is 20 mm. Ionised hydrogen atoms (protons) accelerated down the tube can be used to align the beam using a quartz window assembly to observe the beam, since no neutrons are formed.

The target system consists of a target holder (Fig. 2.7), quartz window, diaphragm, and also an electron suppressing electrode. When the positively ionised particles strike the target or surrounding material in the beam tube they release electrons. The electron suppressor ring prevents the stream back of secondary electrons from the target. The electrons can have energies up to the 600 K.V. and when stopped at the H.T. bun they produce x-rays which are released with maximum intensity at right angles to the bun. The exposure rate may be as high as 50 mr/hour at 1 metre distance.

The diaphragm monitors the divergence of the beam when the neutron shield is in position. During operation the pressure in the accelerator tube is of the order of 10^{-6} torr, the vacuum being maintained by a combined backing pump and diffusion pump. Water is used to cool the diffusion pump and the target. The targets obtained from the Radio-Chemical Centre, Amersham, consisted of approximately 0.3 cc of deuterium or tritium gas absorbed in a thin layer of titanium $200 \mu\text{g}/\text{cm}^2$ thick, which had been evaporated on to a copper disc 2.5 cm in diameter

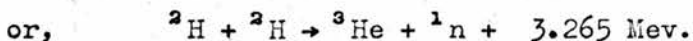
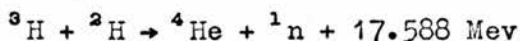
and 0.025 cm thick. The good heat conducting property of the latter assist cooling. There is approximately a one to one relationship between the number of deuterium or tritium atoms and titanium atoms.

Care was taken to minimise the hazard from the tritium targets which contain approximately 4 curies of tritium. Although the weak 18 Kev beta particle emitted produces no external hazard because it is absorbed in the dead layer of skin on the body, the gas becomes a hazard if it enters the body fluids where it can deposit its entire energy within a single cell nucleus (Johnson 1965). Prud'homme (1964) suggests that for a four curie target, one curie per hour will be released in the first two hours operation at 1 mA and less than 1% of the tritium is actually used in neutron production. Most of the tritium released is removed by the diffusion pump and passes into the atmosphere via the outlet valve of the backing pump.

To reduce this hazard an exhaust line was connected to the outlet valve and led outside the building. A negligible amount of tritium remains in the diffusion pump oil. Spare targets were stored in a glove box.

§2.3.2 Neutron Energies

When the accelerated deuterons strike the target, neutrons are released in the nuclear reaction that occurs,



Since the deuteron has a very small binding energy, a very highly excited

compound nucleus is formed by its capture and hence nearly all (d, n) reactions are exothermic.

It can easily be shown from the laws of conservation of energy and momentum that the energy of the neutron in the above reactions for zero incident deuteron energy is given by

$$E_n = \frac{M_R}{M_R + M_n} \times Q \text{ Mev}$$

M_R = mass of residual nucleus

M_n = mass of neutron

Q = energy released in reaction.

When the deuteron kinetic energy is not negligible the relationship is more complex.

$$E_n = \frac{E_d}{A(M_n + M_R)} \left\{ 2 \cos^2 \theta_n + ABM_R \pm 2 \cos \theta_n [\cos^2 \theta_n + ABM_R]^{\frac{1}{2}} \right\}$$

where $A = \frac{M_n + M_R}{M_d M_n}$ M_d = mass of deuteron, E_d = energy of deuteron.

$$\text{and } B = \left[\frac{Q}{E_d} + \left(1 - \frac{M_d}{M_R} \right) \right]$$

θ_n = angle the neutron makes with the direction of the incident deuteron beam.

At 90° to the incident deuteron beam this reduces to

$$E_n = \frac{E_d}{M_n + M_R} \times B M_R.$$

Since the DD and DT reactions are exothermic only the positive value before the third term should be used to find E_n .

The neutron energy is a function of the deuteron energy and the

angle of emission. McKibben (1946) produced energy nomographs for the DD and DT reaction. Tables of neutron energy as a function of θ_n for several incident deuteron energies can be found in a report by Fowler and Brolley (1956).

The deuteron energy to be used in the calculation of the neutron energy is not the incident deuteron energy since deuterons which have lost energy in penetrating the target are still capable of producing neutrons. The energy loss of the deuterons in the target material can be calculated (Benveniste 1954), and hence the average energy, \bar{E}_d , at which the deuterons react with the target nuclei can be obtained from the equation

$$\bar{E}_d = \frac{\int_{E_f}^{E_i} \sigma_T(E) E dE}{\int_{E_f}^{E_i} \sigma_T(E) dE} \quad \dots (2.1)$$

where E_i = initial acceleration energy in kev,

E_f = the energy of the deuterons emerging from the target material, in kev,

and σ = the total cross-section of the reaction.

The stopping power, i.e. the rate of energy loss dE/dx , for deuterons in titanium loaded with deuterium or tritium has not been experimentally determined. Benveniste (1954), however, calculated the stopping power of deuterons in Ti-T using the relation

$$\left\{ \frac{dE}{dx} \right\}_{\text{Ti-T}} = \frac{48}{48 + 3N} \left\{ \frac{dE}{dx} \right\}_{\text{Ti}} + \frac{3N}{48 + 3N} \left\{ \frac{dE}{dx} \right\}_{\text{T}}$$

where $\left\{ \frac{dE}{dx} \right\}_i$ is the rate of energy loss of deuterons in material i , and the fractions are weighting factors to allow for the difference in the atomic weights. N represents the number of tritium atoms per titanium atom which for the present report shall be assumed to be unity. The stopping power of deuterons in titanium was derived from the data of Warsaw (1949) on the stopping power of protons in various materials, and the stopping power of deuterons in tritium from the report by Reynolds (1953). The energy of the incident deuteron beam used to produce neutrons for the present experiments was 300 kev. Calculations similar to Benveniste's were also carried out for a Ti-D target. The rate of energy loss of the deuterons was found to be $316 \text{ kev mg}^{-1} \text{ cm}^2$ for the Ti-D target and $313 \text{ kev mg}^{-1} \text{ cm}^2$ for the Ti-T target.

The thickness of the evaporated titanium layer was $200 \mu\text{g/cm}^2$. When the titanium is loaded with deuterium the volume expansion of the hydride is 20%. Similarly for the Ti-T target the volume expansion is 15%. The corresponding target thicknesses were therefore $240 \mu\text{g/cm}^2$ and $230 \mu\text{g/cm}^2$ respectively. The deuterons with 300 kev incident energy would therefore lose 76 kev in the Ti-D target and the neutrons produced would have a spread in energy, for a fixed angle of emergence, corresponding to deuterons with energies between 224 and 300 kev. The average deuteron energy for the DD reaction was calculated from equation (2.1) to be 266 kev. In the Ti-T target the deuterons lose 72 kev and the average deuteron energy was calculated to be 260 kev.

Throughout the experiments with the monoenergetic neutron beams, the

collimator exit subtended a small solid angle at the target about the $\theta_n = 90^\circ$ position. The solid angle was calculated to be 4.1×10^{-3} radians for the 2 in. beam and 37.2×10^{-3} radians for the 6 in. beam. When allowance was made for the solid angle subtended by the 6 in. collimator exit, the neutron energies at the target, uniquely determined by the angle of observation θ_n and the average deuteron energy \bar{E}_d , were found from the tables of Fowler (1956) to be 2.51 ± 0.06 Mev for the DD neutrons and 14.13 ± 0.10 Mev for the DT neutrons. When the 2 in. beam is used the error in the observed energy of the neutrons emitted from the target should be proportionately lower but the difference is insignificant for the present report where the neutron energies shall be assumed to be 2.5 and 14.1 Mev for the DD and DT neutrons respectively.

When the generator is operating at 600 K.V. and 1 mA beam current the neutron flux is of the order 10^{11} n/sec for the DT reaction, and 10^9 n/sec for the DD reaction, when the targets are fresh. Under maximum operating conditions the lifetime of the DT targets is of the order of 1 mA hour, in which time the yield will have decreased by a factor of five.

§2.3.3 Methods of Measuring Neutron Flux

Although the beam current remained very stable, the neutron flux need not be stable since the beam can be focussed on different parts of the target. Some method was therefore required of monitoring the fast neutron flux emitted at the source with which to compare the flux emitted at the beam exit. In the initial stages of the research programme this

was solved by having two collimated beams from the shield which was identical to that used for the Pu-Be experiments except that an extra 6 in. layer of boron loaded polythene blocks was placed round the two sides of the shield nearest the control desk. The irradiation conditions are shown schematically in Fig. 4.1.

Neutrons from the horizontal beam were incident on the front surface of the phantom. In the vertical beam they were thermalised in a suitable layer of polythene before entering a LiI detector which subtended the beam and acted as a reference standard. The beam current was adjusted to maintain a count rate of 15,000 counts/min on the standard detector and all the experimental data from the horizontal beam was then normalised to one count/min. The count rate in the horizontal beam, and to a lesser extent in the vertical beam, is dependent on the angle subtended by the beam and the area of the target reacting with the incident deuteron beam. The variation in the relative counting rates was minimised by using a diffuse beam of deuterons which covered the entire target area. It was found that the normalised count rate was constant for the 6 in. beam and varied by less than 1.5% for the 2 in. beam.

When large neutron fluxes at the target are to be measured, it is more suitable to use an associated particle detector. The flux is determined by absolute counting of the charged particles associated with the production of neutrons. The number of neutrons per unit solid angle, at any angle, can be calculated from the number of associated particles per unit solid angle at one angle, provided the angular distributions of

the associated particles and the neutrons are known. In the case of the ${}^3\text{H}(d, n) {}^4\text{He}$ reaction, the associated particle is an alpha particle, with an energy of the order of 3.5 Mev, which can easily be detected with a solid state counter. Similarly the ${}^2\text{H}(d, n) {}^3\text{He}$ reaction produces associated ${}^3\text{He}$ particles, which due to their low energies (≈ 1 Mev), have a range equivalent to the scattered deuterons, hence it is difficult to resolve the ${}^3\text{He}$ particles from the unwanted background. Instead the 3 Mev protons from the competing ${}^2\text{H}(d, p) {}^3\text{H}$ may be counted since for low deuteron energies the cross-sections are very similar. The information required for associated particle counting can readily be obtained from the data published by Benveniste (1954 and 1959), Seagrave (1958), and Ruby (1963).

While the associated particle detector has the advantage over the less refined LiI detector technique in that it can measure much larger neutron fluxes, the limiting factor in both cases being the time constants of the amplifier, a disadvantage is that great care is required to obtain reliable results, for example γ pile-up may cause large inaccuracies, also interference may occur due to (n, p) reactions, and recoils. In comparison, the LiI detecting system is very simple to operate, because once the discriminator bias is set at a suitable level below the (n, α) peak, a drift in gain of as much as two channels in one hundred will affect the total number of counts be less than 1/2%. It is unaffected by unwanted background and can be calibrated absolutely against a long counter. For the present report therefore, the LiI detector was

satisfactory as it provided a suitable reference standard within the quoted accuracies. It is planned to use an associated particle detector which has recently been purchased for future experiments where the maximum flux of neutrons available from the generator will be required. The charged particles will be detected by a solid state surface barrier detector.

Several methods of measuring the fast neutron fluxes incident on the phantom were considered:-

- (a) activation analysis,
- (b) plastic phosphor,
- (c) the McTaggart long counter, and
- (d) ^{235}U and ^{237}Np parallel plate fission chambers.

A 1/4 in. sheet of lead was placed half-way along the horizontal beam tube to reduce the gamma background from the target. Since this sheet of lead remained in position throughout the experiments no correction for its presence was required.

§2.3.3(a) Activation Analysis

It was decided at a conference of activation analysts at College Station, Texas (Nucleonics 1965) to standardise a method of measuring the DT fast neutron fluxes. The technique recommended was to expose high purity (99.9%) copper discs, 0.25 mm thick and 1 cm or 2.5 cm diameter, for one minute to the neutron flux to be measured. The associated ^{16}N activity should be allowed approximately one minute to decay before counting the positron annihilation radiation from the sample. The disintegration rate of the ^{62}Cu can then be determined and the flux

quoted in units of disintegration per minute per gram of copper. This method requires a much larger neutron flux, for good counting statistics, than used in the dose measurements in this report. Also it does not give an absolute flux in $n \text{ cm}^{-2} \text{ sec}^{-1}$.

A second possibility was the activation of ^{16}O to produce ^{16}N which undergoes beta decay and the emission of 6 to 7 Mev gamma rays to return to stable ^{16}O . This method was discarded since a large inaccuracy can occur due to the variation in the neutron flux. The half life for the decay of ^{16}N to ^{16}O is 7.36 seconds and since typical irradiations must be of the order of 30 seconds, significant decay of the ^{16}N can occur before the sample is counted. The rate of formation of ^{16}N depends on the incident neutron flux and if this fluctuates during the irradiation period then the ^{16}N decay rate at the end of the irradiation will not be proportional to the integrated neutron flux.

§2.3.3(b) Plastic Phosphor

The fast neutron flux incident on the phantom was measured using 1 in. diameter discs of NE 102 plastic phosphor of various thicknesses (0.05 cm to 0.60 cm). The flux values obtained from the DD beams were $0.18 \text{ n cm}^{-2} \text{ sec}^{-1}$ per count min^{-1} on the standard for the 2 in. beam and $0.30 \text{ n cm}^{-2} \text{ sec}^{-1}$ per count min^{-1} for the 6 in. beam. The corresponding DT neutron fluxes were $0.70 \text{ n cm}^{-2} \text{ sec}^{-1}$ per count min^{-1} for the 2 in. beam and $1.20 \text{ n cm}^{-2} \text{ sec}^{-1}$ per count min^{-1} for the 6 in. beam. The fluxes were estimated to be accurate to $\pm 8\%$ when all possible sources of error were considered.

§2.3.3(c) The McTaggart Long Counter

The long counter developed by McTaggart (1958) was based on the original design of Hanson and McKibben (1947), and had a 40 times greater sensitivity. The response was independent of the energy to within $\pm 3\%$ between 25 keV and 5 MeV. Above 5 MeV the efficiency of the long counter gradually decreased until it was only 70% efficient for 14 MeV neutrons.

The long counter used in the present report was built to the specifications of the McTaggart counter with the exception that the moderator was made of high density polythene instead of paraffin wax in order to minimise distortion. Calibration of the long counter was effected at the Berkeley Laboratories[†] where Thompson and Lavender (1965) have carried out extensive investigations of the response of a McTaggart long counter to various neutron sources. The sensitivity of the Chapelcross long counter was found to be 14% higher than the Berkeley counter. When exposed to the Berkeley 3 curie Americium-Beryllium source emitting 7.54×10^6 n/sec the Chapelcross long counter recorded 4.71×10^{-6} counts per n/sec at 100 cm from the source. The neutron flux values at the collimated beam exit were calculated from the count rate at 100 cm from the source. This distance was measured from the centre of the source to the effective centre of the long counter which is a function of neutron

[†]Central Electricity Generating Board, Dosimeter Calibration Facility, Berkeley Nuclear Laboratories, Gloucestershire, England.

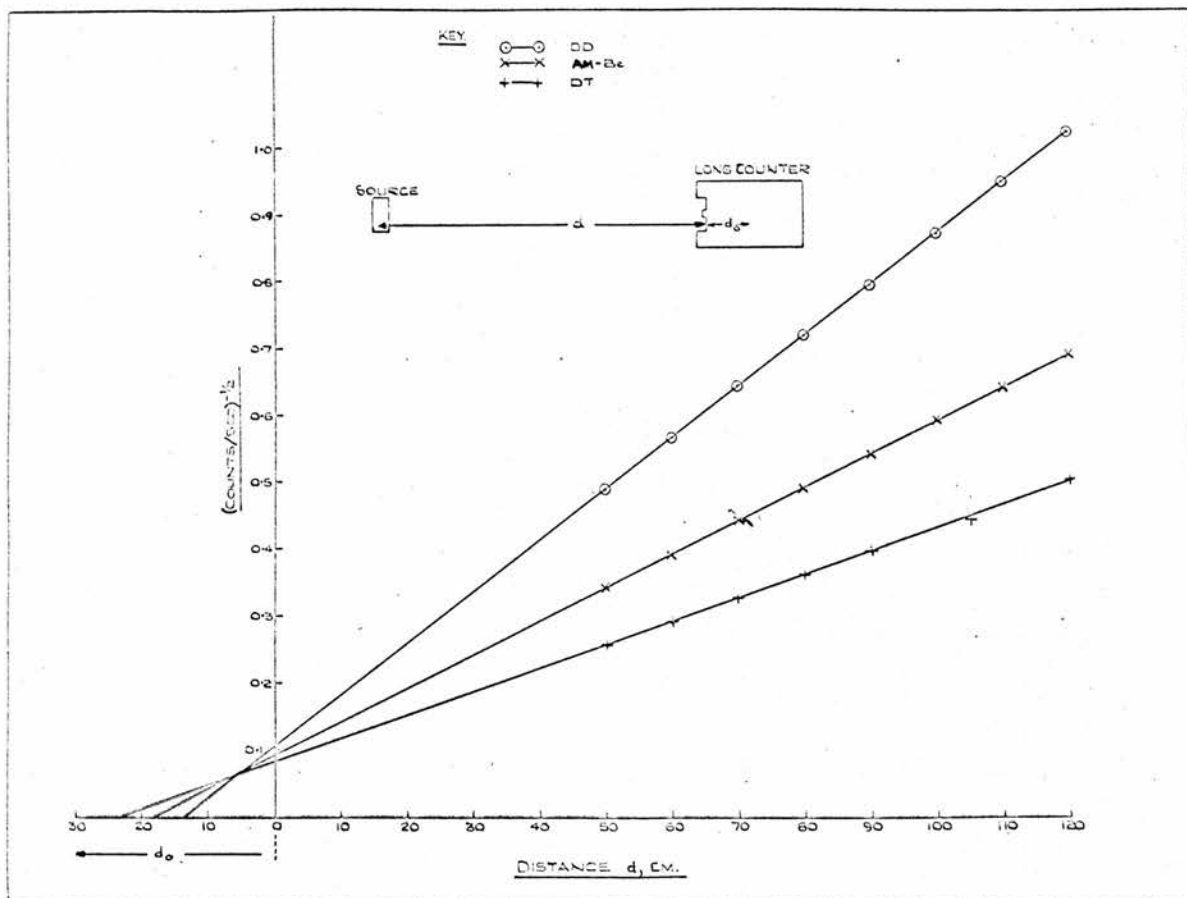


Fig. 2.8 The Effective Centre of the Long Counter.

energy. The effective centre was found by plotting a graph of (count rate)^{-1/2} against the distance of the centre of the source to the front face of the counter (Fig. 2.8), where the count rate has been corrected for background. The effective centre was found to be 18 ± 1 cm for the Am-Be neutrons, 13.5 ± 1 cm for the DD neutrons, and 23.5 ± 1 cm for the DT neutrons. The count rates for the DD and DT neutrons were normalised to 1 count/min on the standard. The flux values obtained in this way for the 6 in. beam DD and DT neutrons were $0.32 \text{ n cm}^{-2} \text{ sec}^{-1} \text{ per c min}^{-1}$ on the reference standard, and $1.18 \text{ n cm}^{-2} \text{ sec}^{-1} \text{ per c min}^{-1}$ respectively, where the reduced sensitivity to the DT neutrons was corrected for by multiplying the value obtained using the sensitivity $4.71 \times 10^{-5} \text{ c sec}^{-1}$ by 1.60 (Thompson 1965). The method was unsuitable for use with the 2 in. beam due to the small beam area. The overall accuracy of flux values measured by this method was estimated to be $\pm 12\%$.

§2.3.3(d) Parallel Plate Fission Chambers

When it was first decided to measure the fast neutron flux using the fission chamber technique there was only a Uranium - 235 parallel plate chamber available, in which the thermal neutron response was approximately 100 times the response to fast neutrons due to the relative cross-sections. If the fission chamber is shielded with boron-10 however, the effective thermal cross-section can be greatly reduced without any appreciable decrease in the fast neutron fission cross-section (Basson 1962). The chamber, which was 2 in. diameter, was therefore suitable for determining an upper limit to the fast neutron flux magnitude provided

it was shielded with enriched boron. Containers of boron-10 of nominal density 2 g/cm^2 were inserted in the collimators at the exit. Thermal neutrons leaking through the shield were minimised by covering the shield face with 0.05 cm thick cadmium sheet and the chamber was surrounded with the cadmium sheet. The effective cross-section of ^{235}U in the $^{235}\text{U}_3\text{O}_8$ oxide when shielded by $2 \text{ gm cm}^{-2} \text{ }^{10}\text{B}$ was obtained from the data of Basson (1962). The fast neutron fluxes determined in this way were enhanced due to the relatively high cross-section for low energy scattered neutrons but were found to agree to within + 10% with the plastic phosphor measurements.

It was decided to purchase a Neptunium - 237 parallel plate fission chamber since the fission cross-section, which has a threshold about 0.3 Mev, rapidly increases to ≈ 1.5 barns at 1.0 Mev and remains fairly constant over a wide energy range. This type of chamber is not affected by the low energy scattered neutrons and provides a better measure of the DD and DT fluxes.

The main advantage of the fission chamber is the low sensitivity to gamma radiation. The sensitivity to neutrons is limited by the amount of fissile material present in the chamber. The thickness of the coating is restricted however, by the absorption of fission fragments on the coating. An approximate estimate of the fraction, F_e , of fission fragments emerging from a flat coating of the oxide of thickness $t \text{ mg/cm}^2$ can be calculated from the relation

$$F_e = 1 - \frac{t}{2(R_{\text{max}} - R_B)}$$

where F_e is the fraction of the particles emerging with a remaining range equal to, or greater than, R_B mg/cm², and R_{max} is the maximum range in mg/cm². For example in the ²³⁵U₃ O₈ oxide the mean estimated range of the fission fragments is 10 mg/cm² (Rossi and Staub 1949).

The range R_B is determined by the bias required to discriminate against the 4 to 5 Mev alpha particles which are emitted by the fissile material. Due to build-up of the alpha pulses, the bias energy must be at least 10 Mev which corresponds to a range R_B of 4 mg/cm² (Abson 1957). F_e for the ²³⁵U chamber used, which had a 1 mg/cm² thick coating of the oxide, was 0.92. The ²³⁵U has low specific activity, but ²³⁷Np has a high activity which restricts the suitable coating of oxide. The coating layer was 0.5 mg/cm² for the ²³⁷Np chamber and F_e was calculated to be 0.96 from Rossi and Staub (1949). The alpha build-up effect was minimised by using short time constants (0.08 μ sec).

The sensitivity, S, of the parallel plate fission chambers to the fast neutrons were calculated from the formula

$$S = \frac{N_A}{A} F_e \sigma_f (E) W \quad \text{counts sec}^{-1} \text{ per n cm}^{-2} \text{ sec}^{-1}$$

where N_A = Avogadro's number,

A = atomic weight of the fissile material,

F_e = fraction of fission fragments detected,

$\sigma_f(E)$ = fission cross-section in cm² at neutron energy E,

and W = weight of fissile material.

The fissile coating for the ²³⁵U chamber was ²³⁵U₃ O₈ which contained

93% ^{235}U , 5.6% ^{238}U and 1.4% ^{234}U by weight. The coated area of the chamber was 15.6 cm^2 and the coating density was 1 mg/cm^2 . Cross-sections for the oxide, obtained by weighting the cross-sections for the isotopes of uranium by the percentage weights, were found to be 1.26 barns for 2.5 Mev neutrons and 2.08 barns for 14 Mev neutrons. The corresponding sensitivities were therefore 4.62×10^{-5} and 7.62×10^{-5} counts sec^{-1} per $\text{n cm}^{-2}\text{ sec}^{-1}$. The flux values obtained using these sensitivities were within + 10% of the phosphor flux measurements.

The cross-sections for fission with Neptunium were 1.45 barns for 2.5 Mev neutrons and 2.5 barns for 14 Mev neutrons. The corresponding sensitivities were therefore 2.74×10^{-5} and 4.73×10^{-5} counts sec^{-1} per $\text{n cm}^{-2}\text{ sec}^{-1}$. The DD beam flux values measured with the ^{237}Np chamber were calculated to be $0.18\text{ n cm}^{-2}\text{ sec}^{-1}$ per count min^{-1} on the standard for the 2 in. beam and $0.32\text{ n cm}^{-2}\text{ sec}^{-1}$ per count min^{-1} for the 6 in. beam. The corresponding DT beam neutron fluxes were $0.71\text{ n cm}^{-2}\text{ sec}^{-1}$ per count min^{-1} for the 2 in. beam and $1.22\text{ n cm}^{-2}\text{ sec}^{-1}$ per count min^{-1} for the 6 in. beam. The major source of error in the measured flux values was the limitation on the accuracy of the cross-section data of $\pm 5\%$. The overall error was estimated to be $\pm 8\%$. The flux values obtained for all the methods used are summarised in Table 2.2

Table 2.2

Methods of Flux Measurement and Experimental Values Obtained

Method	Accuracy	DD Flux n cm ⁻² sec ⁻¹ per count min ⁻¹		DT Flux n cm ⁻² sec ⁻¹ per count min ⁻¹	
		2 in.	6 in.	2 in.	6 in.
Plastic Phosphor	± 8%	0.18	0.30	0.70	1.20
Long Counter	± 12%	-	0.32	-	1.18
²³⁵ U Fission Chamber	± 10%	0.19	0.33	0.74	1.28
²³⁷ Np Fission Chamber	± 8%	0.18	0.32	0.71	1.22

It was decided to take the mean of the neutron flux values measured using the plastic phosphors and the ²³⁷Np parallel plate fission chamber to be neutron flux emitted by the DD and DT beams. The long counter flux measurements were not included due to the relative low accuracy involved and the inability to determine the 2 in. beam fluxes. Similarly the ²³⁵U parallel plate fission chamber measurements were not included because the ²³⁷Np fission chamber provides a more accurate determination of the flux. The mean values of the DD 2 in. and 6 in. beam neutron fluxes were therefore 0.18 n cm⁻² sec⁻¹ per c min⁻¹ and 0.31 n cm⁻² sec⁻¹ per c min⁻¹ respectively, and the corresponding DT fluxes were 0.71 n cm⁻² sec⁻¹ per c min⁻¹ and 1.21 n cm⁻² sec⁻¹ per c min⁻¹.

§2.3.4 Performance of the Shield

When the tests described in §2.2.3 were applied to the shield surrounding the DD and DT neutron sources, similar conclusions were again reached. The shield provided adequate protection from the DD neutrons, and from the DT neutrons when the beam current was less than 200 μA . Above 200 μA however, the neutron background in the laboratory from the moderated neutrons escaping from the shield rose above the level of exposure recommended in NBS 72 (1960). Since the majority of the experiments with DT neutrons were performed at less than 20 μA the shield was suitable for the present report.

§2.3.5 Contamination of the DD and DT Neutron Beams

§2.3.5(a) Deuterium Build-up in Tritium Targets

When the targets are fresh neutrons are produced by the reaction of the incident deuterons with the tritium. Some of the deuterons however, can be retained in the titanium layer and hence become target nuclei producing neutrons by the DD reaction. Secondly the incident deuterons can pass through this layer into the copper backing disc where they are stopped and again act as target nuclei.

Calculations were performed to estimate the effect of deuterium build-up in the titanium. For a target current of 10 μA there are $\approx 6 \times 10^{12}$ deuterons $\text{cm}^{-2} \text{sec}^{-1}$ incident on the 0.3 cc tritium target which contains $\approx 3 \times 10^{18}$ tritium atoms/ cm^3 . If it is assumed that no deuterons, or tritium atoms, are lost other than by nuclear reactions, then after 140 hours continuous operation there would be an equal number

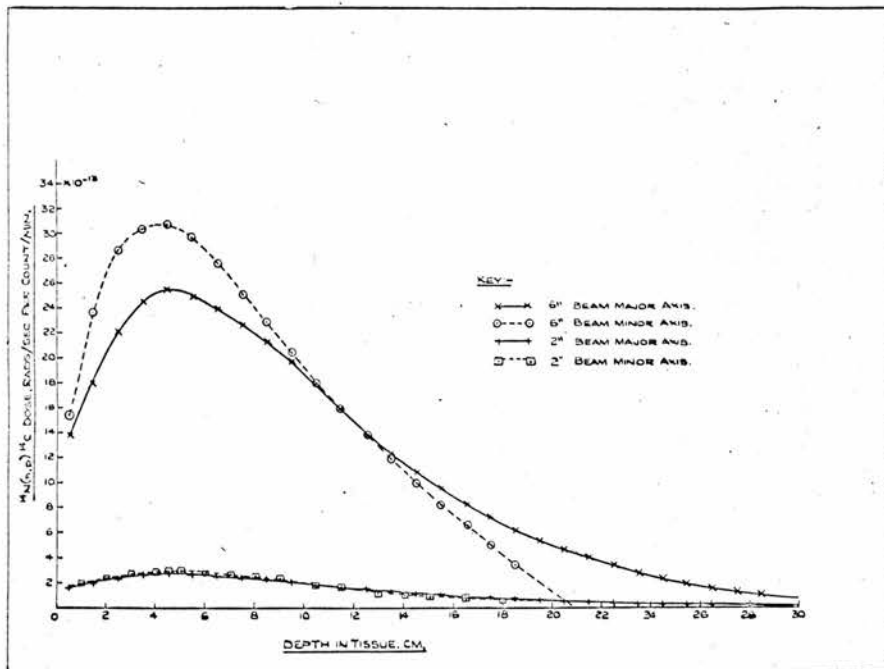


Fig. 4.2 The $^{14}\text{N}(n,p)^{14}\text{C}$ Dose for DD Neutrons Normalised to One Count per Minute on the Standard.

of deuterium and tritium atoms in the titanium layer. Since the cross-section for the DD reaction at 300 kev is 30 times lower than the corresponding DT reaction cross-section, it would take approximately 40 hours continuous operation before the DD neutron contamination of the DT beam was 1%.

In §2.3.2 it was shown that the 300 kev deuterons could pass straight through the target and still retain 228 kev. Since the copper sheet, which has a stopping power of $220 \text{ kev mg}^{-1} \text{ cm}^2$ for 228 kev deuterons, was 200 mg/cm^2 the deuterons would penetrate a few microns and then be stopped. At the end of their penetration the deuterons form a layer source from which they then diffuse through the copper and escape, or, react with other incident deuterons to produce DD neutrons. The magnitude of this effect was checked by replacing the Ti-T target backed with copper, by a plain copper disc of identical dimensions which was subjected to a $250 \mu\text{A}$ target current of 230 kev deuterons and the neutron flux emitted from the 6 in. beam collimator exit was measured at 10 min. intervals. The neutron flux was found to increase gradually with time reaching saturation after 240 mins. during which time approximately 0.8 coulomb/cm^2 of deuterons had impinged on the copper disc. This is in excellent agreement with the observations of Campbell (1954) Gabrysh (1960) and Paic (1963) who found that the neutron flux saturation was reached for several materials after a bombardment of the order of 1 coulomb/cm^2 of deuterons. The saturation neutron flux, measured with a disc of NE 102 phosphor, and expressed in units of $\text{n cm}^{-2} \text{ sec}^{-1}$

per count min^{-1} , was compared with the neutron flux emitted from a fresh Ti-T target at 10 μA target current. After correction for the difference in the target current the neutron flux from the copper was found to be 0.5% of the flux from the TiT target which agrees favourably with the 0.7% calculated from the data of Paib (1963). The conclusion is, therefore, that for 10 μA target current a 100 hours continuous operation would be required before the saturation level of the contaminating DD neutrons would be reached, at which point the DD neutrons would contribute only 1/2% to the total neutron flux. This conclusion is based on the assumption that the neutron yield from the Ti-T target as a function of beam current remains constant with time. In practice this is not the case, and the yield rapidly decreased in the first few hours operation after which it becomes fairly stable. Since the yield would not decrease by more than 10% in the time considered, after 100 hours the contamination would still be less than 5%.

The experimental time for any one Ti-T target was less than 50 hours. Recoil proton spectra observed with the NE 102 flux detectors observed at various intervals during the experiments showed no significant change in shape. It was concluded therefore that the contamination of the DT neutron beams by DD neutrons could be neglected.

§2.3.5(b) Tritium Absorbed in Beam Tubes

The build-up of deuterons in a deuterium target does not appreciably affect the DD neutron beams, although in both Ti-D and Ti-T targets the neutrons so produced must have a lower energy than 2.5 Mev since the

effective deuteron energy is lower for the deuterons entering the copper disc.

A second source of contamination of a DD beam could be neutrons from the DT reaction due to tritium from previous experiments being absorbed in the surface of the beam tube. This was checked by first cleaning the inside of the beam tube and then evacuating the system over 48 hours during which time any tritium present should be removed. The proton recoil spectrum produced by neutrons from a fresh Ti-D target was then observed over a period of a day during which time no change in the spectrum shape was recorded. The Ti-D target was replaced with a Ti-T target which was subjected to a 100 μ A target current of deuterons for 5 hours which should be equivalent to 10 μ A at 50 hours. This was then replaced with a second fresh Ti-D target and the proton spectrum shape observed. During the first few hours of operation at 100 μ A there was a contribution from the DT neutrons produced by tritium still present in the walls of the beam tube but this rapidly fell to negligible proportions after four hours. Hall and Poole (1965) checked for tritium contamination by lining the beam tube with foil from which samples were taken after exposure and found to contain tritium. The tritium in the beam tube desorbed after some time and passed into the pumping system.

§2.4 Thermal Neutron Production

A thermal neutron beam was required to find the diffusion lengths of thermal neutrons in tissue-equivalent liquid. The source was obtained by inserting a 6 cm thick block of polythene, 6 in. square, in the 6 in.

horizontal collimated beam aperture and using 2.5 Mev neutrons from the DD reaction. The front face of the shield was covered with 0.05 cm thick cadmium sheet so that only thermal neutrons which emerged from the polythene block were incident on the polythene container filled with tissue-equivalent liquid. The beam contained thermal neutrons, plus fast neutrons which can be discriminated against, hence leaving essentially a pure thermal beam (Chapter 7).

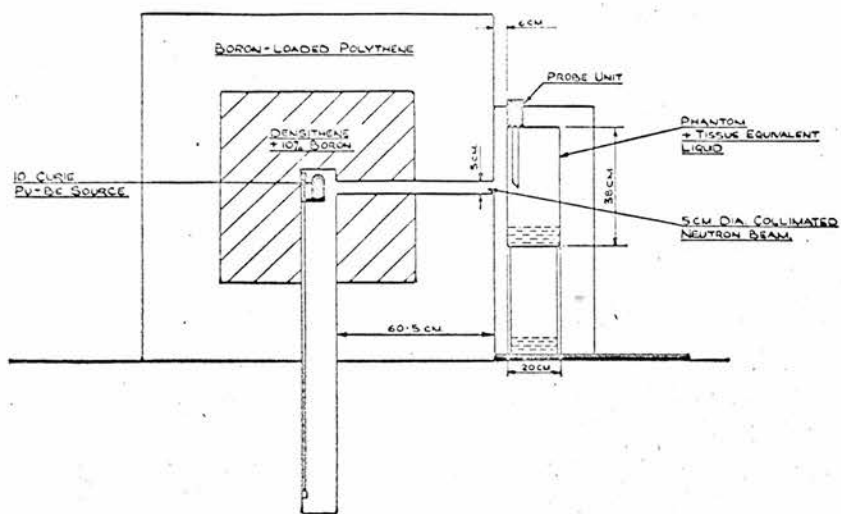


Fig. 3.1. Schematic diagram of irradiation conditions.

CHAPTER THREE

NEUTRON DEPTH DOSE MEASUREMENTS IN A TISSUE-EQUIVALENT PHANTOM
FOR AN INCIDENT Pu-Be SPECTRUM§3.1 Neutron Irradiation Conditions

Theoretical calculations of the energy deposition by neutrons at depth in a body have been made by several authors, in each case the incident neutrons were in the form of a broad monoenergetic beam (Biram 1949 and 1962, Mitchell 1947(b), Snyder 1950, Snyder and Neufeld 1955 and Tait 1949). The 10 curie Pu-Be metal alloy source used in the experiments was not monoenergetic but since the energy spectrum shape is well known (Stewart 1955) the monoenergetic theoretical results were weighted and integrated over the spectrum range to provide theoretical results for the Pu-Be source.

The neutron facility is shown schematically in Fig. 3.1. Its design allows well collimated horizontal beams of various dimensions to be selected. The body was simulated by a polythene phantom which consisted of an elliptical cylinder, 38 cm high with a 20 cm minor axis and a 29 cm major axis, standing on two cylindrical legs. The polythene was 0.65 cm thick and the legs and torso were filled with a tissue-equivalent liquid (Rossi and Failla 1956) whose composition is shown in Tables 3.1 and 3.2.

Table 3.1Chemical Composition of Tissue-Equivalent Liquid

Compound	% by Weight
Water	56.9
Glycerol	28.4
Urea	7.6
Sucrose	7.1

The tissue-equivalent liquid can be represented by a molecule with empirical formula $C_6 H_{40} O_{18} N$. This is easily seen by considering the relation

$$C_x H_y O_z N_w = (H_2 O)_a + (C_3 H_8 O_3)_b + (N_2 C H_4 O_3)_c + (C_{12} H_{22} O_{11})_d$$

where the subscripts a, b, c, d refer to the percentage weight of the molecule in question divided by its molecular weight. The empirical solution is $(C_{1.305} H_{9.754} N_{0.252} O_{4.42})_n$ and hence $C_6 H_{40} O_{18} N$ is the required formula.

The percentage by weight and atomic composition of the tissue-equivalent liquid of density 1.12 g/cc is compared with the standard man composition (N.B.S. Handbook 63), of density 1.00 g/cc in Table 3.2.

Table 3.2

Atomic Composition of Tissue

Element	Tissue Equivalent Liquid $\rho = 1.12 \text{ g/cc}$		Standard Man $\rho = 1.00 \text{ g/cc}$	
	% by weight	atoms/g	% by weight	atoms/g
H	9.83	5.88×10^{22}	10	5.98×10^{22}
C	15.66	0.786×10^{22}	18	0.903×10^{22}
N	3.53	0.151×10^{22}	3	0.129×10^{22}
O	71.07	2.68×10^{22}	65	2.45×10^{22}
Others	-	-	4	-

The phantom was placed in such a way that the beam was perpendicular to the surface at the mid-point, with the front surface of the phantom 6 cm from the collimator exit.

Preliminary tests with lithium iodide and plastic phosphor detectors indicated that, under experimental conditions, scatter from the legs and other surroundings was less than 0.5% and could be neglected.

§3.2 Flux Measurements

When the source was calibrated using the standard manganous sulphate bath technique, the flux of fast neutrons at the exit of the 2 in. diameter collimated beam was found to be $(5.30 \pm 0.50) \times 10^2 \text{ n cm}^{-2} \text{ sec}^{-1}$, and using a 0.64 cm thick disc of NE 102 plastic phosphor it was $(5.44 \pm 0.11) \times 10^2 \text{ n cm}^{-2} \text{ sec}^{-1}$ (§2.2.3). The flux measured using a thin slab of the phosphor, 2.44 cm in diameter and 0.05 cm thick

with a calculated neutron detection efficiency of 0.64%, was $(5.48 \pm 0.12) \times 10^2$ n cm⁻² sec⁻¹ in the 2 in. beam and $(8.09 \pm 0.16) \times 10^2$ n cm⁻² sec⁻¹ in the 6 in. beam. There is seen to be excellent agreement between the flux values obtained using the different sized phosphors. The corresponding fluxes were taken to be 5.46×10^2 and 8.09×10^2 n cm⁻² sec⁻¹ for the 2 in. and 6 in. beams respectively.

Thermal neutron flux measurements were obtained using LiI crystals. The detector was constructed by mounting a 4 mm diameter \times 4 mm thick LiI(Eu) crystal, 96% enriched in ⁶Li, directly on to a 1.25 cm diameter perspex light guide. The crystal, which was virtually 100% efficient, absorbed thermal neutrons by the ⁶Li(n, α) ³H reaction and produced a peak in the spectrum at 4.8 Mev with a resolution of 10%. Gamma radiation was largely discriminated against, as only a small fraction of its energy can be deposited in a thin crystal. The perspex light guide was 23.0 cm long to allow the crystal to be dipped into the tissue-equivalent liquid and traverse the horizontal plane through the mid-point of the collimator with the minimum disturbance of the neutron field. The probe assembly was suspended from a wooden frame and could be moved accurately along runners to any position on the beam axis.

A measurement of the percentage of thermal neutron flux present in the incident beam was obtained from count rates observed when the probe was placed at the collimator exit when (a) a 0.05 cm thick sheet of cadmium was placed over the tube, and (b) when the collimator exit was

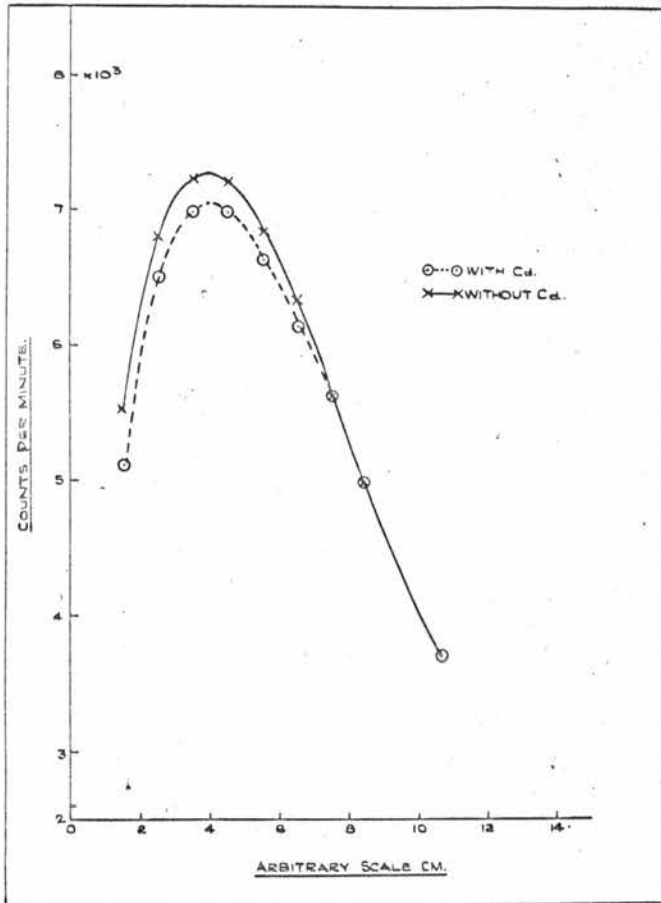


Fig. 3.2 Error Due to Thermal Neutrons in Beam.

uncovered. The ratio of the thermal flux to the fast flux was found to be less than 0.25% for both beams.

§3.3 Thermal Neutron Distribution at Depth in Tissue

Preliminary measurements were made of the thermal neutron distribution in the tissue-equivalent liquid when the phantom was placed 6 cm from the 6 in. square beam exit, with and without cadmium over the hole. The thermal component in the beam was found to contribute to the distribution at depth to a distance of 7 cm from the phantom front surface (Fig. 3.2). Measurements were obtained, therefore, with a cadmium sheet over the beam exit, to remove incident thermal neutrons and allow normalization of the results to one incident fast neutron per cm^2 per sec on the phantom front surface, for comparison with the theoretical results for a Pu-Be source. The latter were deduced by weighting the monoenergetic values (Snyder and Neufeld 1955) for the spectrum shape (Stewart 1955).

Count rates were recorded for both beams at different depths in tissue when (a) the major axis was normal to the beam, and (b) the minor axis was normal to the beam.

These measurements were repeated with the crystal covered with 0.05cm thick cadmium foil to correct for the small percentage of neutrons that were detected above the cadmium cut-off.

The difference in the count rates is the number of thermal neutrons at depth in tissue, but these must be multiplied first by an inverse square law factor. This factor, which varies in value between 1 and 2,

allows for the divergence of the beam between the source and point of measurement in the phantom. Other correction factors to be applied are for,

- (1) the effective surface area of the crystal,
- (2) flux attenuation by the perspex probe,
- (3) flux depression and self shielding,
- (4) neutron scattering and leakage through the shielding.

§3.3.1 Effective Crystal Surface Area

In the first measurements of thermal flux at depth in the phantom it was found that a 1 cm diameter \times 0.1 cm thick LiI crystal had a definite directional response. Calculations indicated that a 4 mm \times 4 mm crystal would have a more uniform response; consequently, tests were conducted by placing a 7.5 cm diameter polythene sphere over the crystal which lay at the centre. The sphere provided a source of thermal neutrons by moderating the incident fast beam. Count rates were recorded at various distances from the collimator exit with the assembly positioned at various angles to the beam. Results proved that the small crystal's response was isotropic and, therefore, the flux was calculated using the total surface area of the crystal as the effective area of detection.

Information on the anisotropy of the thermal neutron flux at depth in the phantom was obtained by comparing count rates observed with the detector for (a) the bare crystal, and (b) various parts of the crystal covered with cadmium foil. The results proved that throughout the phantom the thermal neutrons were symmetrically distributed about the

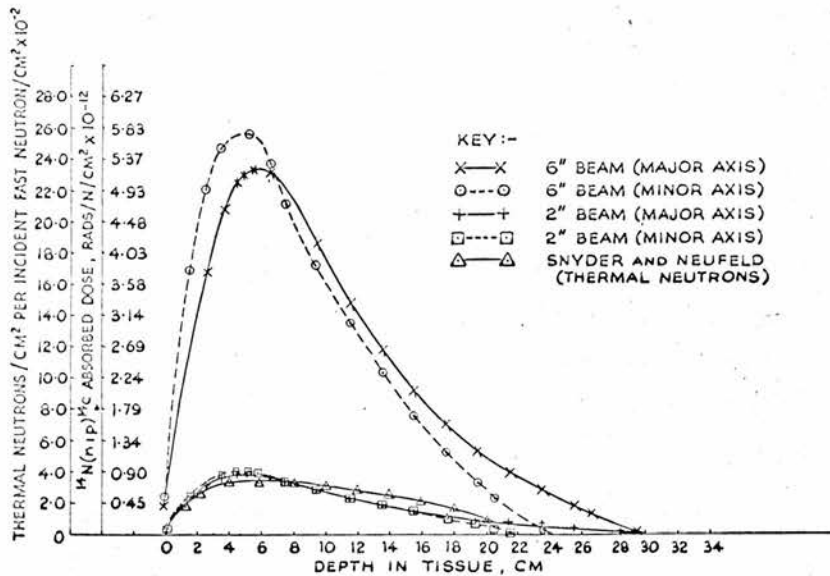


Fig. 3.3. Depth distribution of the thermal neutron flux and the ¹⁴N(n,p)¹⁴C dose in rads produced for each fast neutron per cm² incident on the front surface of the tissue. The dose calculation is described in Section 3.4.1. Note that Snyder's curve shown here is for the number of thermal neutrons and not the thermal neutron flux density.

beam axis. Along the beam axis, however, past the peak, 60% of the thermal neutrons travelled in the beam direction and 40% travelled in the opposite direction. The percentage distribution confirms the observed gradient of the thermal flux at depth in the phantom. This can be seen in Fig. 3.3 which shows the thermal neutron flux (after corrections have been applied) normalised to one incident fast neutron per cm^2 per second for the major and minor axes of both beams.

§3.3.2 Flux Attenuation by the Perspex Probe

The small LiI probe was replaced by a larger probe consisting of a 2.5 cm diameter \times 2 mm thick LiI(Eu) crystal, having a net detection efficiency of 96.4%, attached to a 23.0 cm long \times 2.54 cm diameter perspex rod.

This gave a faster count rate without any appreciable loss in efficiency. Count rates were observed at several positions in the phantom for (a) the probe alone, and (b) the probe plus a second identical perspex rod placed directly below the probe. The results for the 2 in. and 6 in. beams proved conclusively that there was no degradation of the thermal neutron flux due to the presence of the perspex light pipe. For example, at the most sensitive position, namely the peak, both the 2 in. and 6 in. beams gave a "flux attenuation" of $0.3 \pm 0.3\%$ of the observed flux. It was concluded that no correction was required.

§3.3.3 Flux Depression and Self Shielding

Several theories have been developed to account for the perturbation of the thermal neutron flux when a neutron detector is placed in

its field (Bothe 1943, Skyrme 1961). Neutrons which normally pass through the area of measurement more than once may be absorbed in the detector and so only make a fraction of their normal contribution to the total flux. This is known as flux depression. There may also be some attenuation of neutrons in the detector itself, giving a self-shielding effect.

A method has been developed to measure experimentally the flux depression and self-shielding factors and compare them with theory. Since calculation of these effects requires knowledge of the total mean free path and the diffusion length of thermal neutrons in tissue this shall be discussed more fully in Chapter 7. The flux depression factor for the 4 mm \times 4 mm crystal was found to be 1.10 and for the 2.5 cm \times 0.2 cm crystal it was 1.50. The observed thermal neutron flux must be multiplied by the appropriate factor to give the true flux.

§3.3.4 Neutron Scattering and Leakage through the Shielding

The small LiI detector was placed between the front surface of the phantom and the neutron collimator exit. Count rates were taken with pieces of cadmium, the same size as the piece over the collimator exit, placed symmetrically at various positions round the phantom. There was no difference in the count rates so it was concluded that the cadmium over the collimator did not depress the thermal flux.

When count rates were taken with (a) just the hole covered by cadmium foil, and (b) the whole front face of the shield covered with cadmium foil, the count rates dropped by less than 1%. The leakage of

the thermal neutrons through the shield was, therefore, less than 1% of the absorbed thermal neutron flux and also the number of neutrons scattered from the phantom on to the shield face and back again was negligible.

§3.4 Thermal Depth Dose

§3.4.1 $^{14}\text{N} (n, p) ^{14}\text{C}$ Depth Dose

Since thermal neutrons react with nitrogen by (n, p) reactions to form ^{14}C , the number of such reactions taking place in 1 gram of tissue is proportional to the thermal neutron flux density. The reaction is exothermic releasing 620 Kev which is shared between the ^{14}C nuclei and the recoiling protons. This energy is absorbed in less than 10 mg/cm² of tissue and hence the absorbed dose can be calculated on the basis that all the energy is deposited at the site of the reaction.

The absorbed dose D was calculated from the relation

$$\begin{aligned} D &= N\sigma\phi \times 0.62 \times 1.6 \times 10^{-8} \\ &= 2.24 \times 10^{-11} \phi \text{ rad/sec} \end{aligned} \quad \text{..... (3.1)}$$

where N is the number of nitrogen nuclei per gram of tissue (1.29×10^{21} atoms/g), σ is the (n, p) cross-section at 0.025 eV (1.75 barns) and ϕ is the thermal neutron flux.

Fig. 3.3 shows the absorbed dose due to the (n, p) reactions, normalised to one incident fast neutron per cm² at the surface, for the 2 in. and 6 in. beams. The thermal neutron distribution according to Snyder's theoretical values is included for comparison. The doses for the major axis are compared with Snyder's in Fig. 3.4.

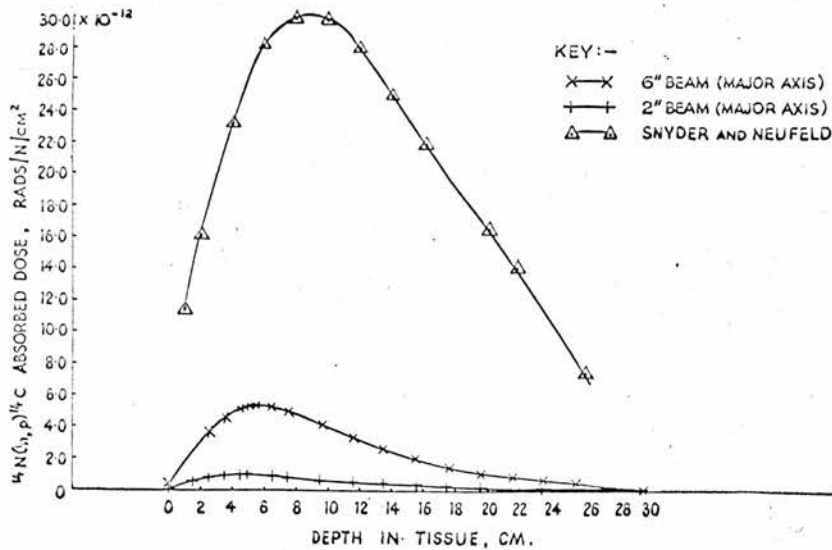


Fig. 3.4. Comparison of measured $^{14}\text{N}(n,p)^{14}\text{C}$ dose for collimated beams fired along the major axis with that calculated from Snyder's data based on the thermal neutron flux density.

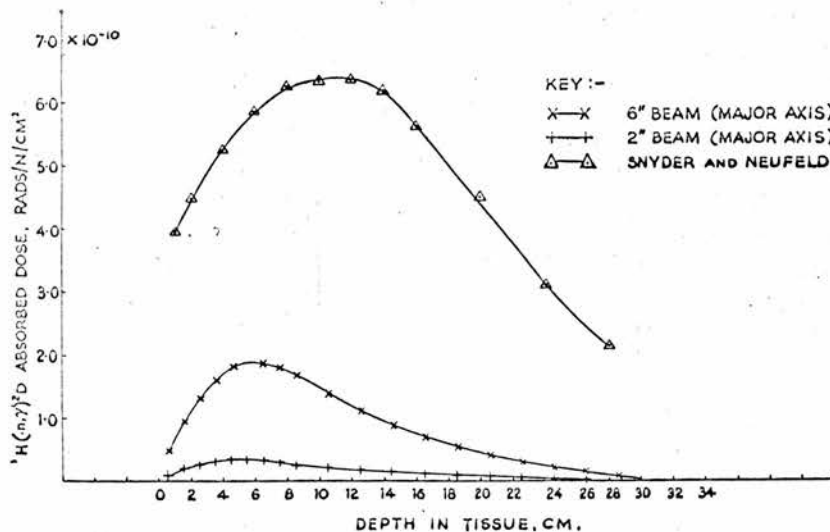


Fig. 3.5. Comparison of measured $^1\text{H}(n,\gamma)^2\text{D}$ dose in the phantom due to collimated beams of Pu-Be neutrons and that calculated from Snyder's data.

§3.4.2 $^1\text{H}(n, \gamma)^2\text{D}$ Depth Dose

The γ -ray released by the (n, γ) reaction has an energy of 2.23 Mev and, because of its penetrating nature, it is difficult to assess the dose. Normally the dose is calculated from a formula devised by Taylor (1954) in which the mass attenuation coefficient is assumed. In the present work the dose in the liquid was calculated from an equation similar to (3.1) where N is now the number of hydrogen atoms per gram of tissue (5.88×10^{22} atoms/g), σ is the (n, γ) cross-section (0.34 barns), ϕ is the thermal flux and the 0.62 Mev has been replaced by an energy factor. To obtain this energy factor the 2.23 Mev γ -ray dose in air was assumed to observe the inverse square law and a correction factor, based on the work of Wooten, Shalek and Fletcher (1954) on the ratio of dose deposition in air to that in water was applied. A numerical integration was then performed to obtain the total $^1\text{H}(n, \gamma)^2\text{D}$ dose in rads per incident fast neutron per cm^2 . The dose can be obtained directly using the Chapelcross Fortran programme CXF 148 with the I.B.M. 7090 computer (Appendix 1). The doses calculated followed a similar trend for the major and minor axes to the dose observed for the $^{14}\text{N}(n, p)^{14}\text{C}$ reaction. The $^1\text{H}(n, \gamma)^2\text{D}$ doses obtained for the 2 in. and 6 in. beams fired along the major axis are compared with the broad beam results of Snyder and Neufeld (Fig. 3.5).

§3.5 Fast Neutron Recoil Proton Dose

The detector was constructed from NE 102 plastic phosphor which is composed of a small percentage of scintillating chemicals in a poly-

vinyltoluene base, and polyvinyltoluene sheet. A thin disc of the phosphor, 2.44 cm diameter \times 0.15 cm thick and weighting 0.729 g was sandwiched between two 2.54 cm diameter discs of polyvinyltoluene each 0.4 cm thick. This has the advantages of being one of the most efficient plastic phosphors for neutron detection and also very fast, with a decay time of 3×10^{-9} secs. Since the phosphor and its surroundings have the same atomic composition the detector satisfies Bragg-Gray conditions for absorbed dose measurements. This was mounted on a 2.54 cm diameter perspex light pipe 23 cm in length, and fitted to a conventional phototube assembly. A Laben 512-channel analyser was used to analyse the pulses produced by proton recoils in the scintillator.

Since the specific hydrogen content is only 16% less than that of tissue and the electron densities are within 3%, the actual energy deposited in tissue can be calculated accurately from measurements made with the phosphor, provided the fraction of scattered neutrons can be determined. Another advantage is its relatively poor response to γ -rays. Measurements using both an ^{241}Am and a ^{22}Na source showed this to be zero.

The energy response of the phosphor is non-linear for all particles except electrons. The response S of the scintillator to a particle of energy E depends on the excitation density produced by the particle, and hence on the specific energy loss dE/dx of the particle along its path length x . Since dE/dx depends on the particle in question and varies along the primary column reaching a maximum near its end

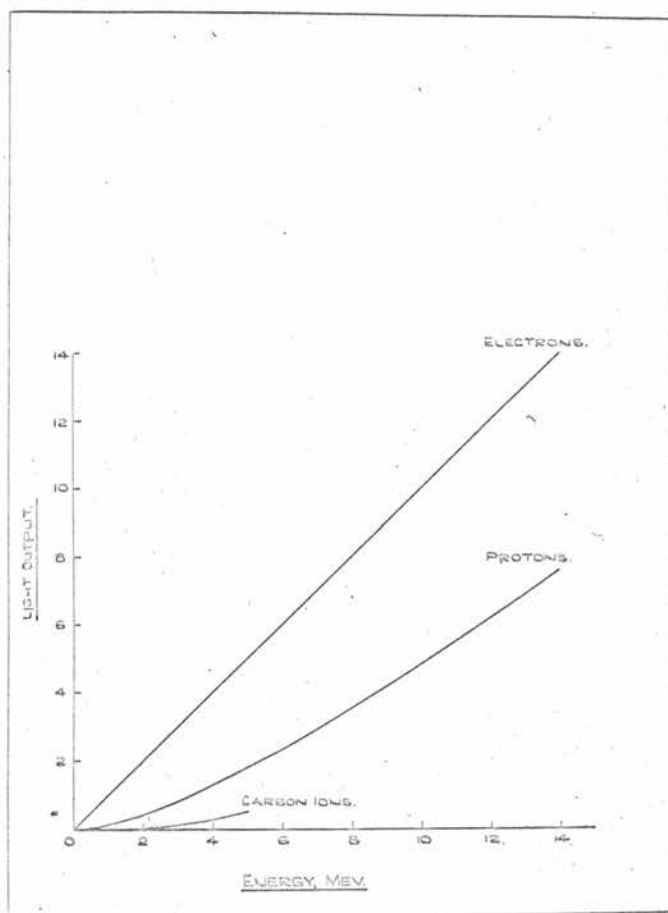


Fig. 3.6 Response of the NE 102 Plastic Phosphor.

(Bragg Curve), $\frac{S}{L}$ is not in general directly proportional to E. Several different forms for the relation between pulse height and energy have been proposed (Birks 1951, Chou 1952, Wright 1953). The formula proposed by Birks has been used in this report,

$$\frac{dS}{dx} = \frac{A \frac{dE}{dx}}{1 + kB \frac{dE}{dx}} \quad \dots (3.2)$$

The specific response $\frac{dS}{dx}$ is equal to $A \frac{dE}{dx}$ modified by the factor $(1 + kB \frac{dE}{dx})^{-1}$ to allow for primary quenching. A and kB are constants.

The response curve for protons, which is well known (Evans and Bellamy 1959, Gettner and Selove 1960), was used to correct the observed pulse height spectra of the proton recoils. Energy calibration was effected by observing the proton recoil spectrum which had an end-point energy corresponding to the maximum neutron energy for the Pu-Be source, i.e. 10.86 Mev.

The non-linear response was advantageous in preventing carbon, nitrogen and oxygen recoils contributing to the proton pulse spectrum. The maximum energy of a carbon recoil atom is approximately $\frac{2}{7} E_n$ i.e. for Pu-Be it is 3.10 Mev. The pulse height response to carbon ions relative to the response to electrons of the same energy was found experimentally by Steuer and Wenzel 1965. Fig. 3.6 compares the response of the NE 102 phosphor to electrons, protons and carbon ions. From the data of Steuer and Wenzel a 3.10 Mev carbon ion produces a pulse which is only 5% of the corresponding electron pulse height and from Evans and Bellamy (1959), a 3.10 Mev proton would have a

corresponding pulse height 30% that of the electron. The ratio of the recoil carbon ion to the proton pulse heights is therefore 1:6. A 3.1 Mev proton produces a pulse $1/6$ th the height of a 10.86 Mev proton and hence the 3.1 Mev carbon ion produces a pulse only $1/36$ th the height of the maximum proton recoil pulse. Carbon recoils, therefore, only affect the recoil proton spectra to a maximum channel number $1/36$ th the end point channel and can be biased out. Similarly for oxygen and nitrogen recoils.

Some difficulty was experienced in determining the proton contribution at the low energy end of the spectrum, which showed a pronounced increase of counts with decreasing energy as a result of the large wall effect associated with Bragg-Gray detectors, the non-linear energy response, and losses in the light pipe. This was resolved by converting the count rates to energy and plotting the differential energy spectrum. At the lower channel numbers the results lay along a straight line which was extrapolated to zero and enabled the energy below the bias level to be deduced. This correction amounted to 20% in the worst instance and could be determined within 10% causing an uncertainty of 2% in the total energy measurements.

It is instructive to consider another effect caused by the non-linear response of the scintillator. The published response curves for the recoil ions have been produced on the assumption that they lose all their energy in the phosphor. The response can be calculated for protons using range-energy data. Gooding and Pugh (1960) have produced a formula

for $\frac{dE}{dx}$ for protons over the energy range 1 Mev to 160 Mev although experiments indicate that it would probably hold for lower energies.

The relation is

$$\frac{dE}{dx} = 17.91 x^{-0.448} \text{ Mev cm}^2 \text{ g}^{-1}$$

where the range x is in g/cm^2 and the energy is in Mev. The constant k_B for NE 102 was found by Evans and Bellamy to be $10^{-2} \text{ g cm}^{-2} \text{ Mev}^{-1}$.

Substituting for k_B and $\frac{dE}{dx}$ in equation (3.2) and replacing S/A by P yields the proton response relation

$$P = \int_{E_{x=\min}}^{E_{x=\max}} (1 + 17.91 \times 10^{-2} x^{-0.448})^{-1} dE$$

where the energy E for $x = \min$ is usually zero corresponding to a proton of zero range and energy.

Since the range x is equal to $k^1 E^\gamma$, where $k^1 = 2.245 \times 10^{-3} \text{ g/cm}^2$ and $\gamma = 1.724$, then the pulse height P is

$$P = \int_{E_{\text{final}}}^{E_{\text{initial}}} (1 + 4.45 E^{-0.775})^{-1} dE \quad \dots (3.3)$$

This is the most general form for the relation between the pulse height and the proton energy deposited in the phosphor. E_{initial} is the energy of the proton when it enters, or is produced in, the phosphor, and E_{final} is its energy when it leaves the phosphor. If the proton is stopped in the phosphor, $E_{\text{final}} = 0$. To integrate the expression

$$P = \int_0^{E_{\text{initial}}} (1 + 4.45 E^{-0.775})^{-1} dE \text{ it is necessary to add the pulse}$$

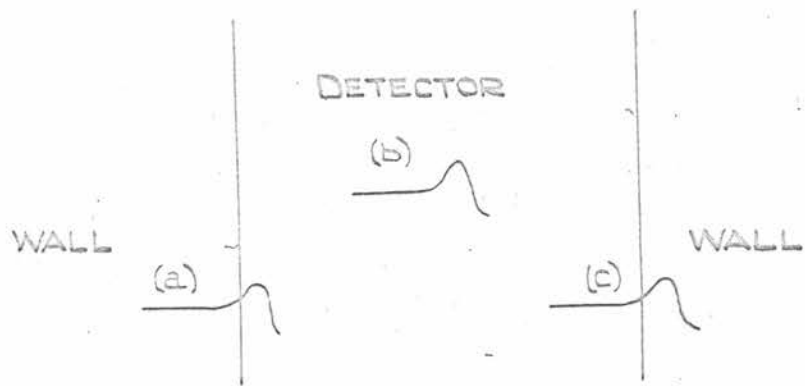


Fig. 3.7 Proton Tracks in Phosphor.

height for a proton of 0.5 Mev to the integral taken between the limits of 0.5 Mev and E_{initial} , due to the limitation on the dE/dx relation of Gooding and Pugh.

During private discussion with H. H. Rossi (Columbia University) it was realised that the dE/dx dependence would give rise to a further correction to the measured energy deposition. Consider the three proton tracks of equal energy E shown in Fig. 3.7. Proton (a) loses a fraction f of its energy E in the phosphor thus the pulse height corresponds to the integration of equation (3.3) between the limits $E_{\text{final}} = 0$ and $E_{\text{initial}} = \text{proton of energy } f.E$. The pulse height is simply that of a proton of energy $f.E$ and accounts for the large increase in counts at low energy end of the proton spectra. Proton (b) has the whole of its track lying in the phosphor and would correspond to a pulse height for a proton energy E . The exception is track (c) where in this case the densely ionising section of the track lies outside the phosphor. The pulse height for this proton can be obtained by integrating equation (3.3) over the track length in the phosphor.

Pulse heights have been compared for these three possibilities, in Table 3.3.

An indication of the magnitude of the effect on the recoil proton dose due to protons of type (c) can be obtained by assuming that statistically there is an equal number of tracks of type (a) and (c). Protons (a) and (b) produce pulses which provide a true measure of the dose, but those of type (c) with the same energy produce larger pulses due to the

exclusion of the Bragg peak, and hence an overestimation of the dose. Pulse heights are compared for the three possibilities in Table 3.3.

Table 3.3

Comparison of Pulse Heights

Proton Energy MeV	Relative Pulse Height		Equivalent Energy to Proton (c) MeV	Fractional Overestimation of the Energy
	Protons (a) and (b)	Proton (c)		
1	8.1	45.6	3.5	3.50
2	20.3	85.5	5.3	2.65
3	36.7	123.7	6.7	2.23
4	56.6	160.0	7.9	1.98
5	79.5	194.5	9.0	1.80
6	105.1	227.0	10.0	1.67
7	133.2	257.4	10.9	1.56
8	163.6	285.5	11.5	1.44
9	196.1	311.1	12.2	1.36
10	230.5	333.9	12.7	1.27
11	266.9	353.9	13.2	1.20
12	305.1	370.3	13.6	1.13
13	345.0	382.5	13.9	1.07
14	386.5	386.5	14.0	1.00

The equivalent energy is the energy required by a proton of type (a) or (b) to produce the same pulse as the protons of type (c). This is

the energy used in the dose calculation, and the fractional overestimation of the energy is given in the final column of the table. The average overestimation of the dose due to type (c) protons is 70%. The fraction of protons produced in the detector which can escape through the walls is approximately 10% for 14 MeV incident neutrons (Young 1965). When allowance is made for the protons which can enter the phosphor from the Bragg-Gray surroundings the overestimation in the dose is found to be 4%. For Pu-Be neutrons the error would be much lower and for DD neutrons it is negligible. Since the magnitude of this effect is not appreciable it is intended to leave a more detailed investigation to a later date.

As a check on the validity of the linear extrapolation, integral spectra were plotted for three different applied photomultiplier voltages and extrapolated to zero bias volts where they intersected to give the total number of protons produced in the detector. The method is similar to that accepted for α , β and γ absolute counting in scintillators (Brinkman 1961). The total number of protons from the integral spectrum, agreed within the statistical error, with the number calculated from the differential spectrum. Furthermore, measurement of the flux in the plastic phosphor based on the linear extrapolation method agreed with independent measurements.

The absorbed dose at depth was measured under the irradiation conditions already described. Proton spectra were recorded for the major and minor axes of the phantoms for both the 2 in. diameter beam and the

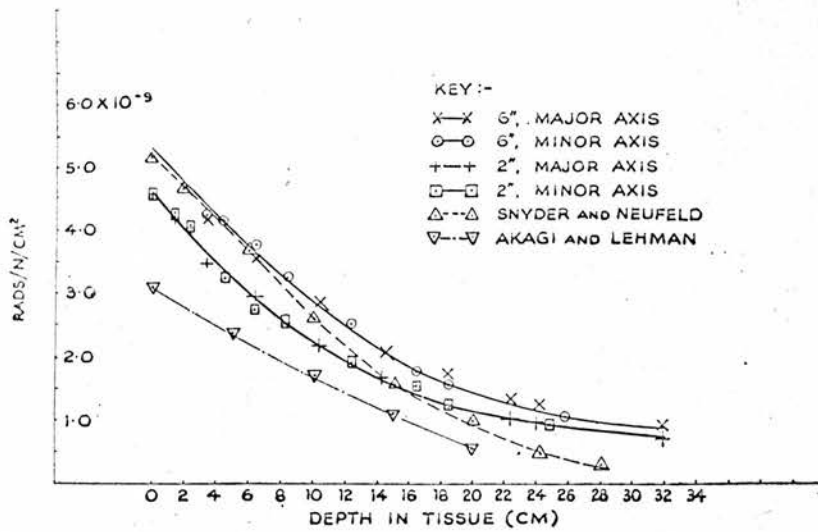


Fig. 3.8. Recoil proton dose deposited in tissue per incident fast neutron per cm^2 at various depths below the surface of a tissue-equivalent phantom.

6 in. square beam. There was no detectable change in the energy absorbed when an identical light pipe was placed in the mirror image position of the perspex probe, also there were no counts recorded from the polyvinyltoluene discs when the phosphor was removed. It was therefore concluded that no correction was necessary for the presence of the probe. Fig. 3.8 shows the results obtained when the spectra were converted to total energy and the dose is expressed as rads per incident fast neutron per cm^2 .

The dose measurements can be obtained directly from the measured proton recoil spectra using Chapelcross Fortran programme CXF 157 and the I.B.M. 7090 computer (Appendix 2).

§3.6 Discussion of Results

§3.6.1 Thermal Neutrons

Snyder and Neufeld (1955) deduced the absorbed dose distribution by first calculating the total number of thermal neutrons produced at depth in an infinitely wide 30 cm thick slab of tissue for an infinitely wide incident beam of fast neutrons. From the total number of thermal neutrons occurring at depth, the thermal neutron collision density was calculated and the results normalised to one incident fast neutron per cm^2 per sec at the surface.

The experimental results were therefore determined in terms of thermal neutron flux per incident fast n $\text{cm}^{-2} \text{sec}^{-1}$, and compared with theory in Fig. 3.3. From this ratio the $^{14}\text{N}(n, p) ^{14}\text{C}$ and $^1\text{H}(n, \gamma) ^2\text{D}$ doses at depth were calculated and plotted in Figs. 3.4 and 3.5

respectively.

Since the $^{14}\text{N}(n, p)^{14}\text{C}$ and $^1\text{H}(n, \gamma)^2\text{D}$ doses were calculated by multiplying the observed thermal neutron flux by the product of the energy released in the reactions and the appropriate abundance ($n \sigma$), it was justifiable to use the atomic composition of the standard man, rather than that of the liquid, to determine the abundance. Smith and Boot (1961) noted that this then allowed direct comparison with the ^{14}N curves of Snyder and Neufeld. The latter used a nitrogen abundance of 4% compared to 3% for the standard man, but Smith and Boot showed that they also used a lower cross-section than in this report, and hence the nitrogen abundance was approximately identical to within 4%.

The energy released in the ^{14}N reaction is deposited locally, but energy released in neutron capture by hydrogen can be deposited over a wide region since the γ quanta have a mean free path of 22 cm in tissue. The maximum thermal neutron dose position therefore need not necessarily coincide.

If no correction for flux depression is made with the LiI detector in the narrow beam, the observed count approaches the number of thermal neutrons present at the point of measurement. When the correction is applied the neutron flux is obtained.

When the number of thermal neutrons instead of neutron flux was measured at depth in the phantom and compared with Snyder's theoretical predictions there was found to be good agreement between the 2 in. beam experimental results and theory, both in the position of the maximum and

in the absolute number of thermal neutrons at depth in the phantom. The 2 in. beam results are expected to be closest to the theoretical assessment of the number of thermal neutrons produced, because the detector is small compared with the incident beam and gives an average neutron measurement over its sensitive area, yet the beam is sufficiently narrow so that contributions due to neutron diffusing from the sides are kept small.

There was a marked increase in the flux of the 6 in. beam due to thermal neutrons, produced by fast neutrons in the more distant parts of the beam, diffusing into the detector from the sides. If absorption losses are neglected, the ratio of thermal neutron flux per incident fast $n \text{ cm}^{-2} \text{ sec}^{-1}$ produced by the 6 in. beam should be equal to the ratio of the beam areas, viz. 11.4:1. The observed ratio was, however, 6:1 which indicated a greater loss of neutrons through the phantom wall in the larger beam irradiation. This conclusion is borne out by the fact that the flux measured at the peak along the major axis was 10% less than along the minor axis for the 6 in. beam compared with less than 2% difference for the 2 in. beam.

Broad beam conditions can be simulated by scaling up the dose for the 6 in. square beam by a factor dependent on the area. The factor should be not greater than six but, since greater losses of neutrons from the phantom are bound to occur for a broad beam, it should be much lower.

The variation of dose with phantom shape and beam size shall be

discussed in detail in Chapter 6. It shall be shown that by considering two group theory that the position of the thermal neutron flux peak can be predicted from the equation,

$$x_{\max} = \frac{L_R L_D \ln L_R/L_D}{L_R - L_D} \dots\dots (3.4)$$

where x_{\max} is the peak position of the flux along the axis of the beam, L_R is the relaxation length of the incident fast neutrons and L_D is the diffusion length of the thermal neutrons, for the tissue-equivalent liquid.

The peak position x_{\max} can only be calculated for the 2 in. beam since the theory is based on an incident parallel beam of neutrons incident on the material. For the Pu-Be 2 in. beam $L_R = 9.80$ cm and $L_D = 2.68$ cm and hence $x_{\max} = 4.80$ cm. The experimental peak occurs at 4.6 cm which shows good agreement with the two group theory prediction.

The $^{14}\text{N}(n, p)^{14}\text{C}$ dose is also a maximum at 4.6 cm since it is directly proportional to the thermal neutron flux, however, according to the theory of Snyder it should be about 9 cm. The discrepancy is possibly due to the method used in calculating the ^{14}N thermal neutron dose from the neutron collision density. Snyder neglects to average the thermal neutrons over a Maxwellian distribution of energies, and also, more important, neglects the effect of chemical binding of the elements on the scattering or transport cross-section (§7.2).

The diffusion length used to determine x_{\max} is for tissue-equivalent

liquid which differs slightly in composition to body tissue. The actual position of the maximum of the thermal neutron flux will depend on the parameters of body tissue but the difference is expected to be much less than 10%.

It is concluded that the predicted dose of Snyder and Neufeld is an upper limit and, further, that the maximum dose occurs nearer the phantom face, i.e. at approximately 4.6 cm rather than the 9 cm theoretical depth of Snyder. The results of Aceto and Churchill (1963), Akagi and Lehman (1963) and Smith and Boot (1961) also show the peak to be nearer the front of the phantom. Similar conclusions are reached regarding the $^1\text{H}(n, \gamma) ^2\text{D}$ absorbed dose.

§3.6.2 Fast Neutrons

The results in Fig. 3.8 show that the energy deposited at depth is the same for a beam traversing the major or minor axis. A comparison of the 6 in. and 2 in. beam results shows also that there is less dependence on the beam size for the amount of energy deposited than is observed for thermal neutrons. This is to be expected since the recoil protons produced by fast neutrons have a short range and the energy is distributed locally. It is concluded, therefore, that neither the extra mass of liquid at the sides when a specific beam is fired along the minor axis, nor the greater depth of liquid when the same beam is fired along the major axis, cause any appreciable scattering of fast neutrons which will contribute to the absorbed dose.

However, the recoil dose from the 6 in. beam compared with the dose

from the 2 in. beam is consistently 15% higher throughout depth in the phantom. This is due to more neutrons being scattered into the detector from the remote parts of the 6 in. beam than from the 2 in. beam. As is to be expected, the scatter effect is very much smaller than observed in the thermal measurements.

The 6 in. beam should correspond closely to Snyder's broad beam conditions for the following reason. It is found that an increase in beam size from 2 in. diameter to 6 in. square (i.e. a factor of 11.4 to 1 in area) increases the proton dose by 15%. A further factor of 5 increase in area is required for whole torso irradiation and, by extrapolation, this would increase the dose by less than 10%, i.e. the 6 in. beam should approach within 10% of the broad beam conditions.

Fig. 3.8 shows that the 6 in. beam dose measurements agree very well with Snyder's calculations to a depth of 10 cm but decrease less rapidly at greater depths. The discrepancy may be due to experimental error, theoretical over-estimation for removal of energy from the beam, or error in the neutron spectrum shape (Stewart 1955) at higher energies. It has been emphasized by J. W. Smith (private communication) that the average neutron energy from the Pu-Be source must be equal to or greater than the average absorbed energy per neutron deduced from the area under the proton depth dose curve. Calculations from the 6 in. beam results in Fig. 3.8 show this to be 4.74 Mev when a 10% correction is included for extrapolation to infinite depth and 6% for energy lost to heavy recoils.

Relaxation lengths for the 2 in. and 6 in. beams can be calculated using the empirical formula

$$D_x = D_0 e^{-x/L} \quad \dots (3.5)$$

where D_x is the fast neutron proton dose at depth x , D_0 is the surface dose and L is the relaxation length. The relaxation length for the 2 in. beam is used in determining the thermal neutron flux peak position, while the relaxation length for the 6 in. beam allows the total proton dose to be estimated by integrating equation (3.5) from $x = 0$ to $x = \infty$. The values of the relaxation lengths obtained were 9.80 cm for the 2 in. beam and 15.0 cm for the 6 in. beam.

On examination of the depth dose curve it should be noted that for values of $x < 3$ cm depth, the dose curve departs from the exponential relation and the value of D_0 used in equation (3.5) is in fact the extrapolated value of the exponential curve.

The total energy deposited by the 6 in. beam using this approximation technique is 4.76 Mev which agrees favourably with the ~~4~~ 4.74 Mev already calculated. Such excellent agreement is rather fortuitous as the Pu-Be dose measurements are only approximately exponential with depth.

Since Stewart finds the average energy of Pu-Be neutrons to be only 4.4 Mev, a separate estimate of the average energy of the Pu-Be neutrons was obtained by measuring the average proton energy directly in a thin slab of plastic phosphor which covered the 2 in. collimator. The

average neutron energy was deduced from the formula $\bar{E}_p = \bar{E}_n (\cos \theta)^2$ to be 4.72 ± 0.09 Mev. Confirmation of the result was obtained by deducing the flux from the same measurements when precise agreement was found with the earlier measurements. Adjustment of the theoretical results for the difference in average neutron energy would not fully account for the discrepancy between experiment and theory at depth in the phantom. Recent work on the Pu-Be neutron spectrum shape (§2.2) by Anderson (1963), Geiger (1964) and St. Romain (1962) indicated that the average neutron energy was 4.4 Mev, but that 15% of the neutrons had energies below 1 Mev as against the 9% predicted by Stewart (1955). Large Pu-Be sources can be expected to have an even larger percentage of low energy neutrons (Heertje 1964). The detectors used here would not see the majority of these neutrons which have energies less than 0.3 Mev. If 20% of the neutrons are assumed to have energies below 1 Mev, the average energy of the remaining neutrons is 4.8 Mev which is in excellent agreement with the dose measurements.

When the depth dose curves are normalized to unit dose at the phantom face, the 6 in. and 2 in. beam curves agree to within $\pm 5\%$ throughout the depth while the deviation from the theoretical results is clearly demonstrated. The results of Akagi and Lehman (1963) indicate a similar trend of dose with depth but the absolute dose is only 60% of the theoretical, which could be due to failure to correct for low energy events below the instrument bias. The proton dose attenuation with depth has a half-thickness value of 10 cm for all the experimental and

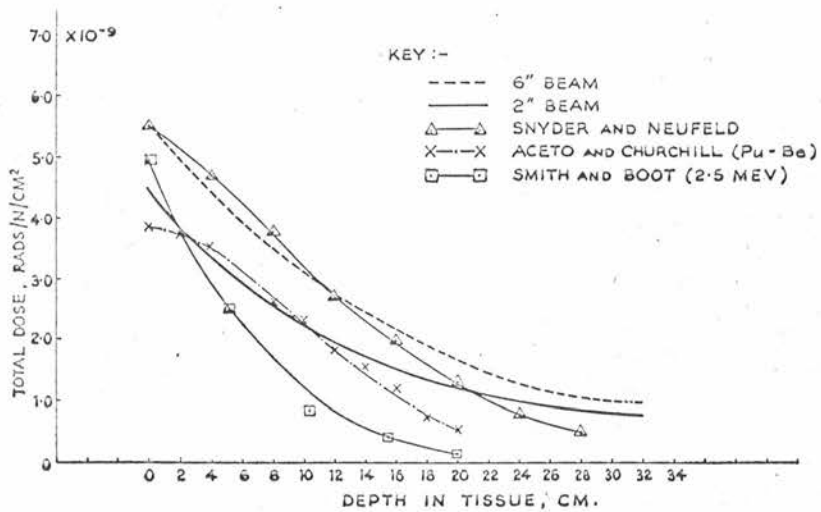


Fig. 3.9. Comparison of published results for the total dose in rads due to fast neutrons.

theoretical curves in Fig. 3.8.

A comparison of the total fast neutron dose at depth in a tissue-equivalent phantom for a Pu-Be source, measured by Aceto and Churchill (1963) and this report is shown in Fig. 3.9. The dose for a 2.5 Mev beam is included for comparison (Smith and Boot 1962).

An uncollimated point source of Pu-Be was used by Aceto and Churchill who corrected for the inverse square divergence giving effectively results for an infinitely narrow beam. The 2 in. beam in this work comes closest to these conditions and the results compare favourably to about 14 cm, beyond which the curves rapidly diverge. When the results of Aceto and Churchill, and Akagi and Lehman are normalised to the dose at the front surface of the phantom, they confirm the greater divergence at depth for Pu-Be neutrons than indicated by theory, although there is a wide spread in the experimental results.

§3.7 Dose Equivalent for Proton Recoils

The dose equivalent (DE) in rems is given by the product of the quality factor (QF) and the absorbed dose in rads measured at a depth in tissue.

The definition of Quality Factor is discussed fully in the Report of the R.B.E. Committee (1963) and is associated with "the definition of maximum permissible dose and with the concepts underlying the additivity of different types of radiation exposure" for radiation protection purposes. It is not a straight forward definition because the biological effects produced are influenced by the conditions of exposure and the

quality of radiation. It is "intended as the value which ensures that the risk from a maximum permissible dose of high linear energy transfer, LET, never exceeds that from a maximum permissible dose of Low LET reference radiation".

The committee also recommended that for the purpose of specifying the radiation quality the basic parameter should be the "Stopping Power" i.e. LET_{∞} and that the quality factor should be related only to LET in water. Table 3.4 shows the LET-QF relationship.

Table 3.4

LET_{∞} Kev/ μ in water	Q.F.
< 3.5	1
3.5 - 7.0	1-2
7.0 - 23	2-5
23 - 53	5-10
53 - 175	10-20

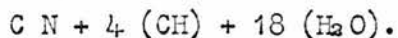
The QF values currently recommended by the R.B.E. committee are approximated by the linear relation

$$QF = 0.8 + 0.16 \bar{L}, \text{ where } \bar{L} \text{ is the dose average LET} \quad \dots (3.6)$$

This should give a conservative assessment for chronic exposure and the highest R.B.E. of importance "and is valid for LET values ranging to 100 Kev/ μ of water".

That the quality factors can be calculated on the basis of linear energy transfer in water has been demonstrated by Cowan (1964). The

composition of tissue $C_5 H_{10} O_{18} N$ was assumed to be expressed equally well by



The stopping powers of C, CH and H_2O for protons are given in the tables of Rich and Madey (1954) and since the stopping power of nitrogen is almost identical to that for carbon, CN can be replaced by $2(C)$. The stopping power of tissue for protons was calculated from the known stopping power of the constituent elements. Table 3.5 shows the comparison between the calculated stopping power for soft tissue, and the stopping power of water from Rich and Madey (UCRL-2301). If the accuracy of the data in UCRL-2301 is taken into account then the stopping powers can be assumed equal.

Table 3.5

Proton Energy	$(LET_{\infty})_{\text{Tissue}}$	$(LET_{\infty})_{\text{Water}}$	Water % Difference
1 Mev	276.6	279.4	1.0
10	46.56	46.91	0.8
100	7.337	7.397	0.8

Alternatively the slowing down of protons can be calculated from the relativistic stopping power formula, using the values 18, 78, 85 and 98 electron volts respectively for the mean excitation energy of hydrogen, carbon, nitrogen and oxygen (Fano 1963). Turner (1964) did this using the composition given in Table 3.2 for the standard man. The values obtained for LET_{∞} by this method are compared with the

corresponding LET's for water in Table 3.6.

Table 3.6

Proton Energy	(LET _∞) Standard Man	(LET _∞) Water	Water % Difference
1 Mev	268.05	279.4	4.1
10	45.19	46.91	3.7
100	7.139	7.397	3.5

The percentage difference is slightly larger this time but still small enough to be neglected. Thus it can be seen that the stopping power of water makes a good approximation to that of tissue.

Before discussing the derivation of the relevant QF for the present experiments it is appropriate to discuss the significance of the term 'average LET'. There are at present three definitions commonly used for 'average LET' ($\overline{\text{LET}}$) in neutron dosimetry.

- (1) The LET of a particle of the mean energy of the proton recoils. If the average proton energy is \bar{E} then $\overline{\text{LET}} = \bar{E}/R$ where R is the range of a proton of energy \bar{E} in water. This value of $\overline{\text{LET}}$ is convenient because it can be measured experimentally at depth in tissue by observing the proton energy spectra (e.g. KERMA).
- (2) The mean value of LET with respect to dose, i.e.

$$\overline{\text{LET}} = \frac{\int_0^{\infty} L \cdot D(L) \cdot dL}{\int_0^{\infty} D(L) \cdot dL} \quad \dots (3.7)$$

where $D(L).dL$ is the fraction of the total dose D delivered over a given range dL of LET. This is the \bar{L} used in equation (3.6).

(3) The mean value of LET with respect to track length, i.e.

$$\overline{\text{LET}} = \frac{\int_0^{\infty} L.T(L).dL}{\int_0^{\infty} T(L).dL} \dots\dots (3.8)$$

where $T(L).dL$ is the fraction of aggregate track length T associated with a given range dL of LET.

For chemical and biological effects the chief interest lies in the proportion of total dose deposited in different LET intervals. Mean LET is therefore of limited use but mean LET values determined on the basis of definitions (2) and (3) above are biologically more significant than a mean LET given by the first definition. Here LET includes all energy transfers (delta rays, excitation, ionization etc.) between the proton recoil and the surrounding molecules.

The only direct method of experimentally measuring the dose average LET to date was developed by Rossi and Rosenzweig (1953) who used a tissue-equivalent, spherical proportional counter filled with methane gas at low pressure to compute the LET distributions. The method, although ingenious, is difficult to operate in practice and the minimum practicable dimensions necessary for the counter (~ 4 in. diameter) make it unsuitable for depth dose studies.

§3.7.1 Mean LET - for Radiation Protection

The mean LET as defined by $\overline{\text{LET}} = \bar{E}/R$ is of no value to radiobiologists

as it does not give a sufficiently detailed account of the dose structure i.e. distribution of dose as a function of LET. It would, however, provide a very simple method of determining the quality factor for use in radiation protection. An attempt was therefore made to determine an approximate mean LET from the dose measurements. It was hoped that by using a thin phosphor (0.15 cm thick) that for a large number of recoil events entering and leaving, or stopping in, the phosphor that the statistical averaging process would provide the correct average LET calculated on the basis of E/R_E where E is the energy recorded in the kicksorter channel and R_E the corresponding range. This should not be confused with the specific energy loss, dE/dx , of the particle along its path length x (Chapter 5).

The \overline{LET} calculated in this manner although similar to definition (1) differs in that in this case the proton energy includes that due to residual protons i.e. wall and end effect in the phosphor, whereas definition (1) is for first collisions only (i.e. kerma).

The absorbed dose in rads has been determined at depth in the body. To determine the dose average LET it is necessary to analyse the dose at each point as a function of LET. This is complicated by the non-linear response of the phosphor to the recoil protons. In determining the dose due to the recoil protons use was made of the fact that the maximum energy the proton could have was 10.86 Mev. Each channel's width therefore corresponded to a definite energy increment which was different for every channel. A typical graph of energy against channel

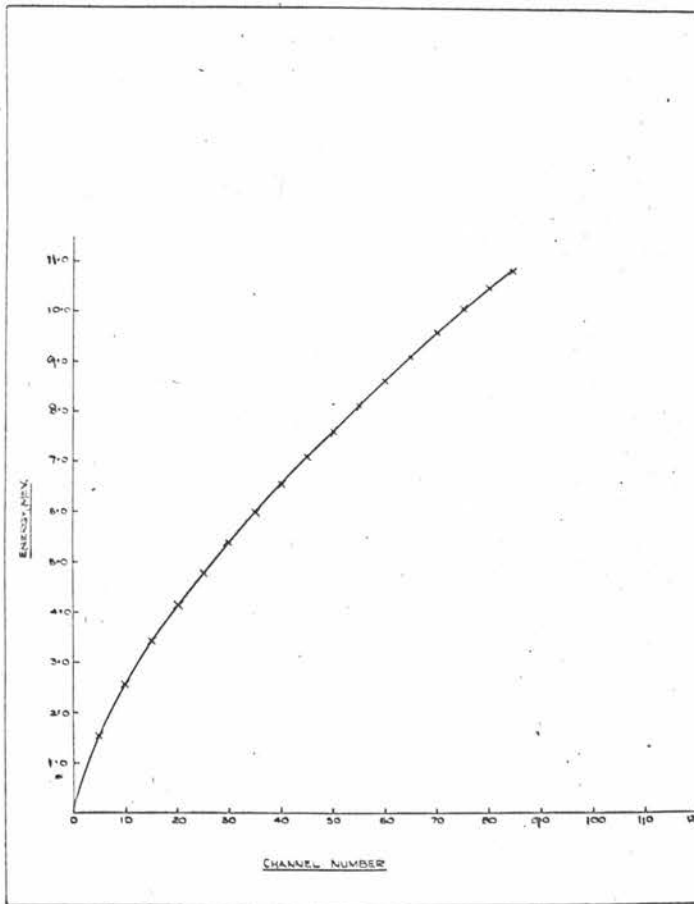


Fig. 3.10 Calibration of Channel Width in Terms of Proton Energy.

number is shown in Fig. 3.10. Channel number 85 corresponds to 10.86 Mev and using the data of Evans and Bellamy the 'energy' of each channel was computed. From the range energy relation $R = k^1 E^{\gamma}$ and the definition that LET is E/R_E , the LET interval ΔL corresponding to each channel width was calculated, and hence the dose D_C in each channel can be converted to dose per unit LET interval i.e. D_L , where

$$D_L = \frac{D_C}{\Delta L}$$

The dose D_L was plotted against the LET, L , in the form of a histogram. A typical graph is Fig. 3.11. A smooth curve was drawn through the histogram such that the area under the curve was equal to the total dose at that point

$$\text{i.e. } \int_0^{\infty} D_L dL = \text{total dose.}$$

The mean value of LET with respect to dose was found using the Chapelcross Fortran programme CXF 157 to compute \overline{LET} from

$$\overline{LET} = \frac{\int_0^{\infty} L \cdot D_L \cdot dL}{\int_0^{\infty} D_L \cdot dL} \quad \dots (3.9)$$

The \overline{LET} values calculated in this manner were found to be constant at all depths in the tissue to within $\pm 5\%$. The 2 in. beam \overline{LET} was 40 Kev/ μ and for the 6 in. beam it was 46 Kev/ μ .

Since this is approximately the same as determining the \overline{LET} by dividing the total energy deposited in the detector by the number of

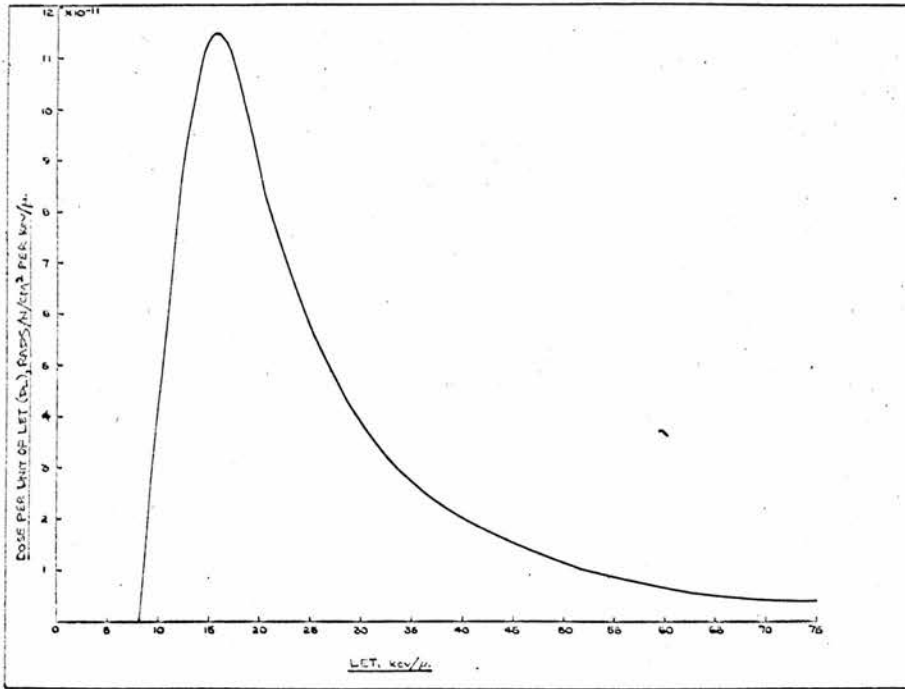


Fig. 3.11 Dose per Unit LET Interval Plotted Against the LET.

protons depositing the energy, to find the average proton energy, and then dividing this by the corresponding range, calculations were carried out to find the average energy.

The average proton energy deposited in the detector by the 2 in. beam was found to be 1.17 ± 0.02 Mev where the error was the standard deviation of the mean. This value was constant at all depths in the tissue to within a 4.5% spread in results, confirming the findings of the group at Hammersmith Hospital that the energy spectrum of a poly-energetic fast neutron beam remains essentially the same to a depth of 15 cm in a tissue-equivalent phantom (Field 1964, 1965). Since a 1.17 Mev proton has a range of 29μ in water, the corresponding average LET (\bar{L}_2 in.) at depth is $40 \text{ Kev}/\mu$ of water.

Similarly when the tissue was irradiated by the 6 in. beam it was found that the average proton energy was also constant with depth but was of lower magnitude, viz. 1.02 ± 0.01 Mev with a spread of 3% in the results. The fact that the absorbed dose is higher for the 6 in. beam, yet the average proton energy is lower for the 6 in. beam when compared with the 2 in. beam, verifies the deduction that neutrons are scattered from the more remote parts of the beam into the detector. If scattering is assumed to be negligible for the 2 in. beam conditions, it can be deduced that 29% of the protons contributing to the dose deposited by the 6 in. beam were produced by scattered neutrons which produce an average proton energy of 0.64 Mev. The remainder of the dose is deposited by 71% of first collision protons having an average

energy of 1.17 Mev. The net average LET (\bar{L}_e in.) from the two components is 45 Kev/ μ of water.

Since both methods of calculating the average LET for the 2 in. and 6 in. beams give (40 ± 2) Kev/ μ and (45 ± 2) Kev/ μ respectively, the second method which is very much simpler should be adopted. The average LET obtained in this manner for the 2 in. beam closely approaches in magnitude the dose average LET, \bar{L} used in equation (3.6). Since the spectrum was sensibly constant at depth in the phantom, \bar{L} for Pu-Be neutrons was deduced from the curves published by Rossi and Rosenzweig (1955(b)) and enabled a QF to be obtained for comparison with the present results. \bar{L} was found to be 42.4 Kev/ μ of water corresponding to a QF of 7.6. When \bar{L} for the 2 in. beam was substituted into equation (3.6) the QF was 7.2.

The value of \bar{L} found from Rossi's data is valid for an incident parallel beam and is attributed only to first collision neutrons. It cannot, therefore, be applied to the 6 in. beam results where scattered neutrons contribute a significant fraction of the dose and produce higher LET proton recoils which increase the QF. The QF for the 6 in. beam with $\bar{L}_{ET} = 45$ Kev/ μ was 8.0.

The "dose as a function of LET" graphs obtained using the method outlined above should not be confused with the curves published by Rossi (1955(b)) or the theoretical curves of Boag (1954). This is due to the assumption made that LET could be approximated to E/R , instead of dE/dx . The former is always greater than the latter which results in

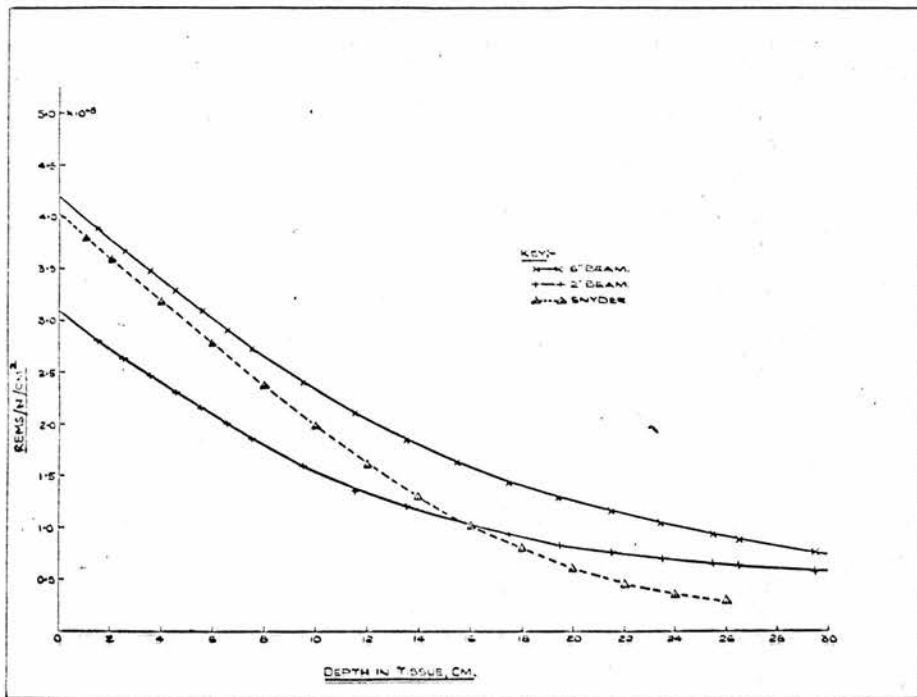


Fig. 3.12 Dose equivalent for proton recoils at depth in tissue. The total dose equivalent for proton recoils, $^{14}\text{N}(n,p)^{14}\text{C}$ and $^1\text{H}(n,\gamma)^2\text{D}$ events is effectively the same curve since the capture reactions contribute less than 1%.

a spectrum which overestimates the peak magnitude and position by approximately 50%. Curves based on dE/dx shall be discussed in Chapter 5.

It is concluded that this method is quite suitable for determining the \overline{LET} for Radiation Protection purposes.

§3.7.2 Dose in Rems

Dose equivalents of the proton recoils for the 2 in. and 6 in. beams calculated from the absorbed dose and QF values determined for $\overline{L}_{2\text{in.}}$ and $\overline{L}_{6\text{in.}}$ are plotted in Fig. (3.12).

The sum of the DE for the three components is essentially the same as shown in Fig. (3.12) since the $^1\text{H}(n, \gamma) ^2\text{D}$ events contributed a maximum of 0.6% and the $^{14}\text{N}(n, p) ^{14}\text{C}$ component was negligible. Snyder calculates a maximum of 2% of the DE due to $^1\text{H}(n, \gamma) ^2\text{D}$ events and less than 1% due to $^{14}\text{N}(n, p) ^{14}\text{C}$ reactions.

The theoretical DE curves (broad beam conditions) should be compared with the 6 in. beam results. If the quality factors used by Snyder for monoenergetic neutrons (N.B.S. Handbook 63, 1957)[†] are adjusted to the Pu-Be neutron spectrum, a value of 7.9 is obtained which is sensitive to the weighting factors employed in the calculations. This shows excellent agreement with the present experimental QF of 8.0 and Rossi's experimental value of 7.6. There is very good agreement between the

[†]Note: There is a discrepancy between the absorbed dose (rads) given in Figs. 4A and 5A in Handbook 63 and Figs. 3 and 5 in Snyder and Neufeld (1955). The latter are used in Fig. 3.12 with QF = 7.9.

experimental and theoretical dose equivalent at the surface but a discrepancy of a factor of 2.5 occurs at the back of the phantom.

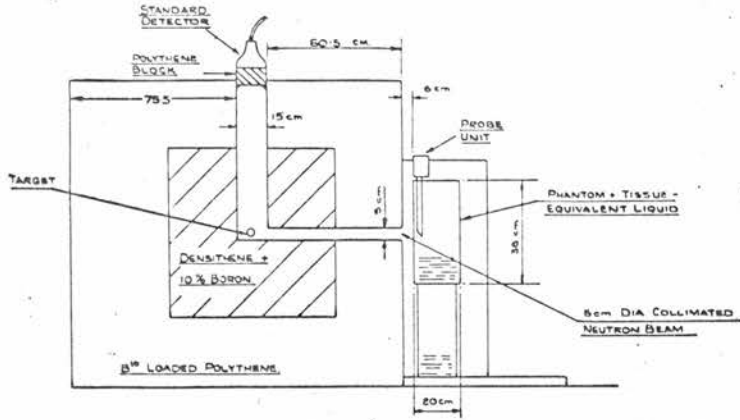


Fig. 4.1 Schematic Diagram of the Irradiation Conditions.

CHAPTER FOUR

EXTENSION OF DEPTH DOSE MEASUREMENTS TO IRRADIATION
BY MONOENERGETIC DD AND DT NEUTRON BEAMS§4.1 Introduction

The amount of energy deposited at depth in a tissue-equivalent phantom was discussed in detail in Chapter 3 for incident collimated beams of polyenergetic neutrons from a Pu-Be source. It is the purpose of the present discussion to include the additional information obtained when similar measurements were made for irradiation of the phantom by monoenergetic DD and DT neutrons. The neutron facility was described previously in Chapter 2 and the irradiation conditions (Fig. 4.1) remained virtually the same as in the Pu-Be experiments. The essential difference was the introduction of a LiI(Eu) detector as a reference standard to which all the experimental data could be normalised (§2.3.3).

The components of absorbed dose due to the 2.5 Mev DD neutrons can be compared directly with the theory of Snyder and Neufeld (1955). The 14.1 Mev DT neutron dose measurements can, however, only be compared with the 10 Mev theoretical dose curves of Snyder, and where appropriate, with the 14.1 Mev kerma calculations of Randolph (1957). The 10 Mev dose curves of Snyder should provide a fair comparison to the 14 Mev components of dose since, according to Randolph the proton recoil dose from elastic collisions, for kerma, is only 69.5% of the total recoil dose. This corresponds to a kerma of 4.62×10^{-7} erg g^{-1} per n cm^{-2} compared to 4.50×10^{-7} erg g^{-1} per n cm^{-2} for 10 Mev neutrons.

Secondly the thermal neutron components of the dose are slowly varying functions of incident neutron energy.

The mean value of the fast neutron fluxes incident on the phantom (§2.3.3) for the DD source were 0.18 ± 0.014 n cm⁻² sec⁻¹ per c min⁻¹ on the standard for the 2 in. beam and 0.31 ± 0.025 n cm⁻² sec⁻¹ per c min⁻¹ for the 6 in. beam. The corresponding DT fluxes were 0.70 ± 0.056 n cm⁻² sec⁻¹ per c min⁻¹ for the 2 in. beam and 1.21 ± 0.097 n cm⁻² sec⁻¹ per c min⁻¹ for the 6 in. beam. These fluxes were used to calculate the absorbed dose in units of rads per incident fast neutron per cm² where the components of absorbed dose were measured using the detectors and techniques described in Chapter 3.

§4.2 Thermal Neutron Depth Dose

§4.2.1 Thermal Neutron Distribution at Depth in Tissue

A LiI crystal was used to determine the thermal neutron flux at depth in the phantom (§3.2). Count rates were recorded for the 2 in. and 6 in. beams at different depths in the phantom for both sources. These measurements were repeated with the crystal covered with 0.05 cm thick cadmium foil to correct for the percentage of neutrons detected above the cadmium cut-off. The difference in count rates was the number of thermal neutrons at depth in tissue, which had to be multiplied by an inverse square factor to allow for the divergence of the beam between the source and the point of measurement in the phantom. After correcting for flux depression and self-shielding effects the true flux was 1.10 times the measured flux.

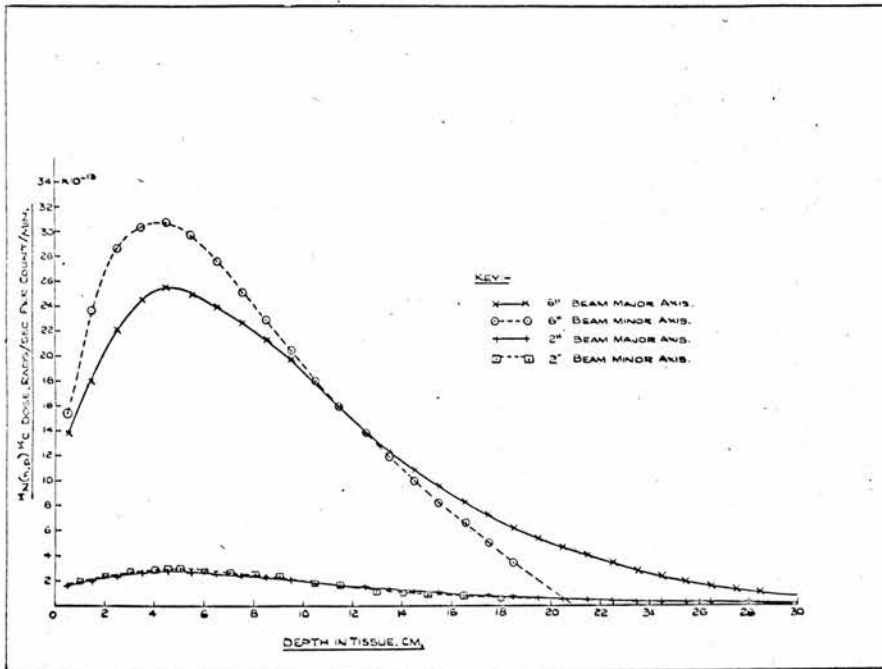


Fig. 4.2 The $^{14}\text{N}(n,p)^{14}\text{C}$ Dose for DD Neutrons Normalised to One Count per Minute on the Standard.

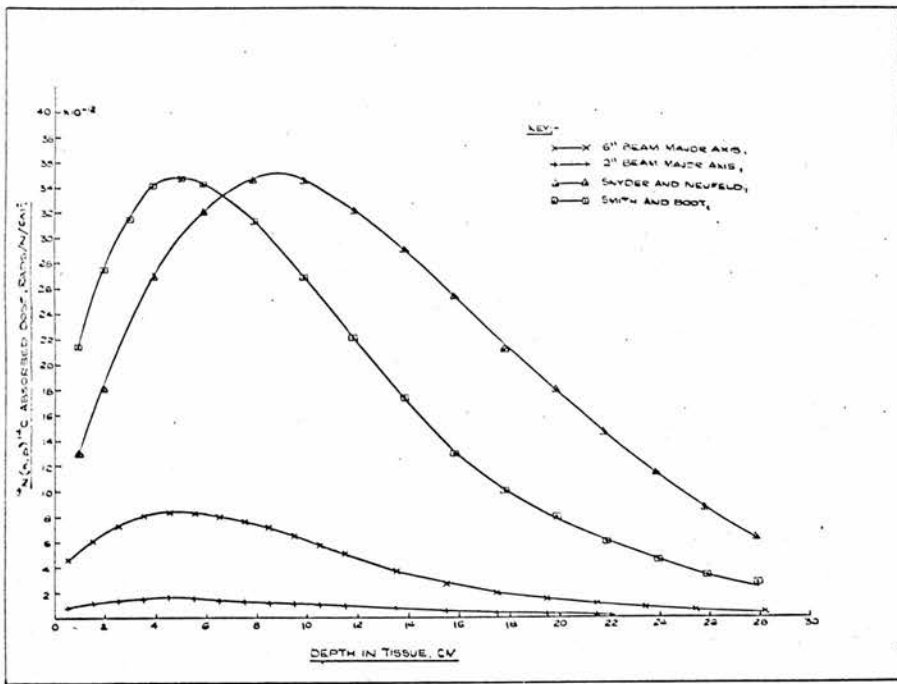


Fig. 4.3 The $^{14}\text{N}(n,p)^{14}\text{C}$ Dose for DD Neutrons in Rads/n/cm 2 .

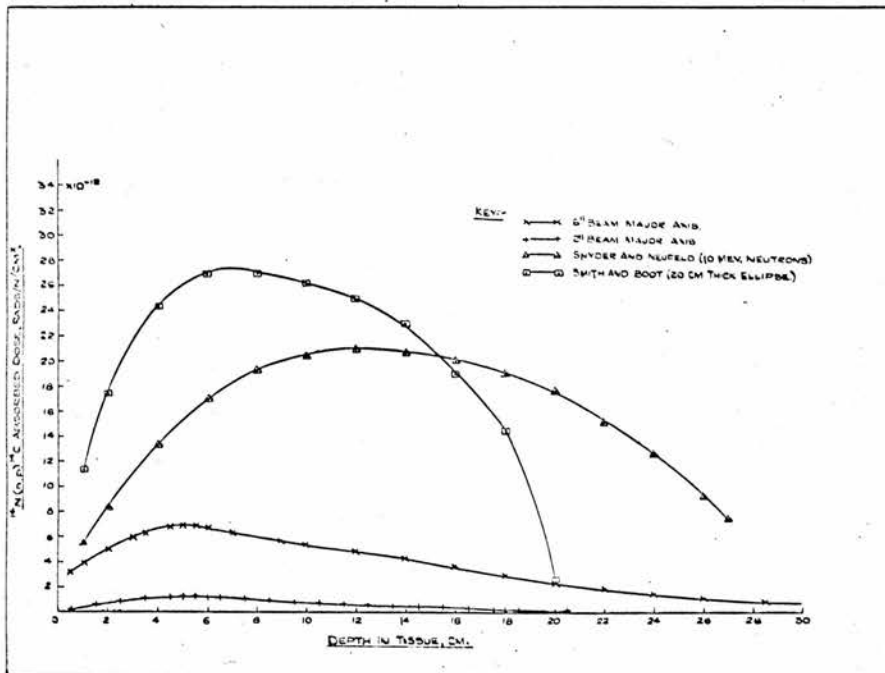


Fig. 4.4 The $^{14}\text{N}(n,p)^{14}\text{C}$ Dose for DT Neutrons in Rads/n/cm 2 .

§4.2.2 $^{14}\text{N}(n, p)^{14}\text{C}$ Dose

The absorbed dose, D , due to thermal neutron reactions with nitrogen is directly related to the corrected thermal flux, ϕ , by the relation

$$D = 2.24 \times 10^{-11} \phi \text{ rad/sec} \quad \dots\dots (3.1)$$

Fig. (4.2) shows the absorbed dose for DD neutrons due to the ^{14}N reaction normalised to one count per min. on the standard. The graph for DT neutrons is similar. In both cases the major axis dose for the 6 in. beam is approximately 15% lower than the minor axis dose, at the peak position, while for the 2 in. beam the difference is only 2 to 3%. There is also a marked increase in the dose for the 6 in. beam compared to the 2 in. beam as can be seen more clearly in Fig. 4.3 for DD neutrons and Fig. 4.4 for DT neutrons, where the doses for the major axis have been expressed in units of rads per incident fast neutron per cm^2 . It was suggested in §3.6.1 that if absorption losses were neglected the ratio of the thermal neutron flux per incident fast neutron per cm^2 produced by the 6 in. beam to that for the 2 in. beam should be equal to the ratio of the beam areas, viz. 11.4 : 1. The observed ratio is, however, approximately 6 : 1 which is in agreement with the Pu-Be data. This, together with the smaller dose for a beam along the major axis, indicates a greater loss of neutrons through the phantom wall, and also by absorption in the phantom, for broad beam irradiation. A more complete discussion will be given in Chapter 6. At present, however, it is postulated that an indication of the dose due to an infinitely wide beam incident on the phantom can be obtained by scaling up the 6 in.

beam results by a factor of 4. This yields a dose of $\approx 33 \times 10^{-12}$ rads per $n \text{ cm}^{-2}$ for the 2.5 Mev DD neutrons and $\approx 28 \times 10^{-12}$ rads per $n \text{ cm}^{-2}$ for the 14 Mev DT neutrons. These values indicate that Snyder's data can be used to determine the $^{14}\text{N}(n, p) ^{14}\text{C}$ dose due to a broad beam of neutrons incident on a human.

The maximum dose is seen (Figs. 4.3 and 4.4) to occur nearer to the phantom front surface than was predicted by Snyder. For example the 2 in. DD beam maximum dose lies at 4.8 cm rather than the 9 cm theoretical value. Smith and Boot (1961) also found the peak for 2.5 Mev neutrons to be about 5 cm. When the peak position was calculated from equation (3.4).

$$x_{\text{max}} = \frac{L_R L_D \ln L_R/L_D}{L_R - L_D}$$

where L_R was 9.2 cm it was found to be 4.7 cm. Similarly the peak position for the DT 2 in. beam calculated using $L_R = 13.5$ cm was 5.4 cm which compares favourably with the experimental value of 5.5 cm. This method cannot be used to determine the peak position for the 6 in. beam since the beam is diverging.

The conclusions are those of §3.6.1 that the predicted dose of Snyder and Neufeld is an upper limit and that the maximum dose occurs nearer to the front surface of the phantom.

§4.2.3 $^1\text{H}(n, \gamma) ^2\text{D}$ Dose

The method used to determine the absorbed dose from the penetrating gamma rays released in the $^1\text{H}(n, \gamma) ^2\text{D}$ reactions was detailed in §3.4.2

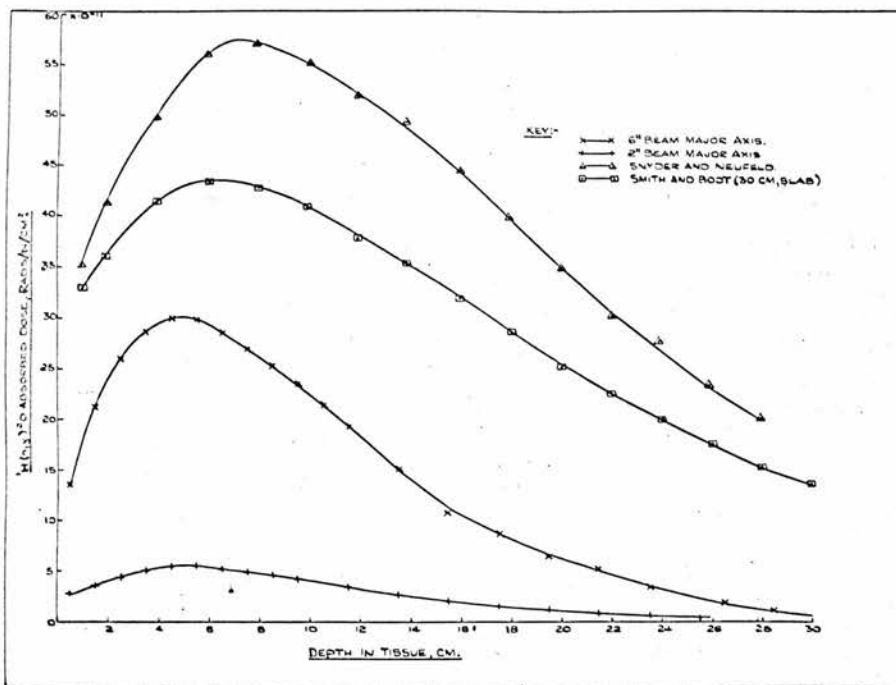


Fig. 4.5 The ${}^1_0\text{H}(n,\gamma){}^2\text{D}$ Dose for DD Neutrons in Rads/n/cm².

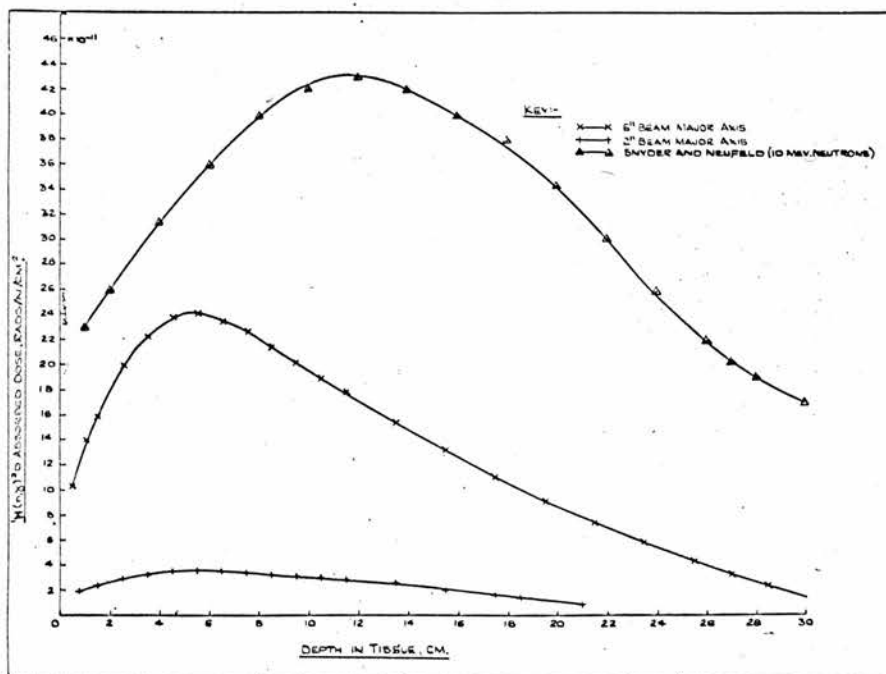


Fig. 4.6 The ${}^1_0\text{H}(n,\gamma){}^2\text{D}$ Dose for DT Neutrons in Rads/n/cm².

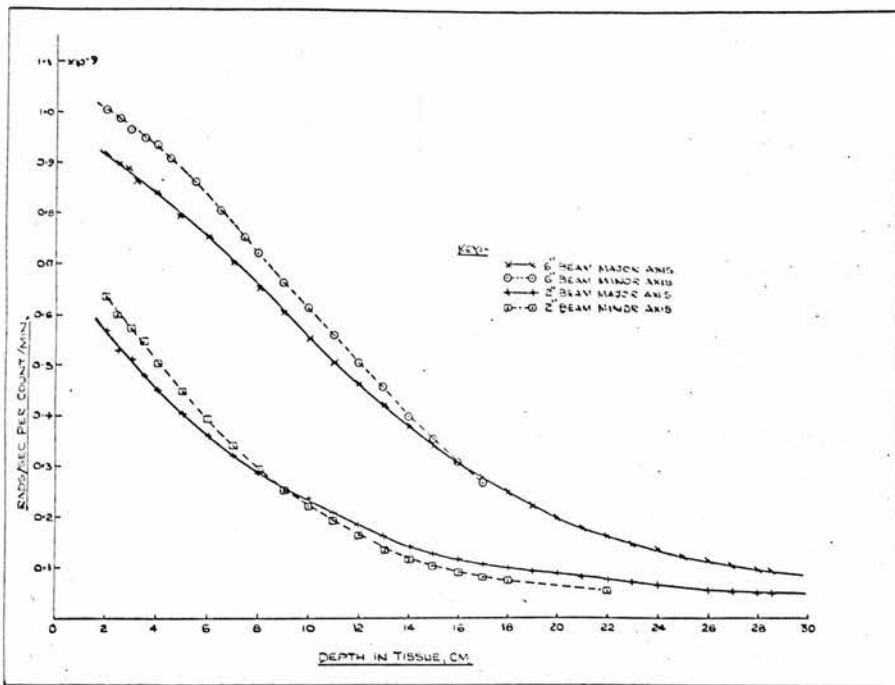


Fig. 4.7 The Recoil Proton Dose for DD Neutrons Normalised to One Count per Minute on the Standard.

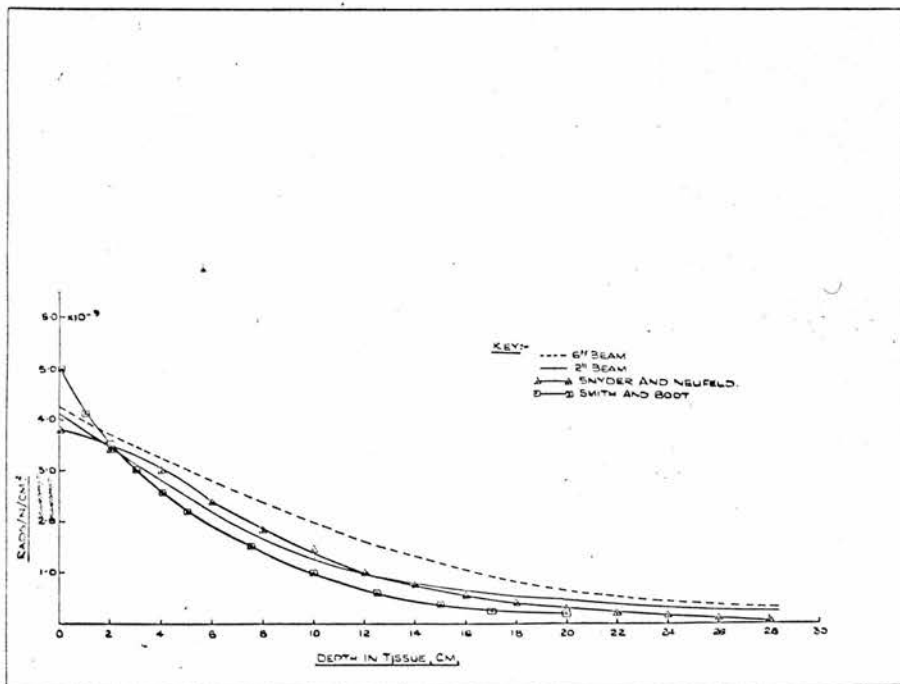


Fig. 4.8 Comparison of Published Results for the Recoil Proton Dose in Rads due to DD Neutrons.

and the results were obtained from the I.B.M. 7090 computer. The calculated doses followed a similar trend to the $^{14}\text{N}(n, p) ^{14}\text{C}$ dose curves. Figs. 4.5 and 4.6 show the $^1\text{H}(n, \gamma) ^2\text{D}$ doses obtained for the 2 in. and 6 in. DD, and DT beams, respectively, fired along the major axis. The theoretical curves of Snyder and Neufeld are included for comparison. Similar conclusions are reached for the $^1\text{H}(n, \gamma) ^2\text{D}$ dose.

§4.3 Fast Neutron Proton Recoil Dose

The Bragg-Gray detector described in §3.5, which consisted of a thin disc of NE 102 plastic phosphor sandwiched between discs of polyvinyltoluene, was used to measure the absorbed dose due to recoil protons from fast neutron elastic collisions.

§4.3.1 DD Proton Recoil Dose

Fig. 4.7 shows the relative doses for the DD beams before normalization to one incident fast n $\text{cm}^{-2} \text{sec}^{-1}$. The minor axis dose is greater than the major axis dose to approximately 16 cm for the 6 in. beam and 9 cm for the 2 in. beam, after which it slowly falls below the major axis dose. The maximum difference, which is due to more neutrons being scattered into the detector from the remote parts of the beam, is less than 15%.

The absorbed dose, in rads per neutron per cm^2 , for the 2 in. and 6 in. beams is compared with the results of Smith and Boot who used nuclear emulsion detectors, and with the theory of Snyder and Neufeld, in Fig. 4.8. There is good agreement between the 2 in. beam curve and Snyder's theoretical curve. As in Fig. 3.8, the corresponding Pu-Be

graph, the 2 in. and 6 in. beam curves enclose Snyder's to about 15 cm depth in tissue. The data of Smith and Boot would appear to be inaccurate due to the possible reasons stated in their report. The main source of error lying in the estimations of the fast neutron flux present and hence in the calibration of the nuclear emulsion detectors. Secondly, the curve in Fig. 4.8 was obtained by taking the mean of their experimental values and a predicted upper limit to the dose. The latter was calculated on the basis that the maximum kinetic energy available for proton recoils from neutrons of energy E_n , was E_n . This was an over-estimation of the true upper limit since they assumed that all the energy E_n was deposited in the 30 cm and that there were no heavy recoils due to carbon, nitrogen or oxygen. It was also simply an upper limit to the integrated proton recoil dose and was therefore not necessarily an upper bound at all depths in the phantom. From the experimental evidence of the neutron dose for various sources measured using the nuclear emulsion technique the dose is consistently under-estimated if Snyder's theory is correct. Since the present measurements support the theory, or at least suggest that the true dose is equal to or greater than that predicted by theory, the emulsion technique is shown to be unsatisfactory.

The relaxation lengths calculated from equation (3.5) were found to be 9.2 cm for the 2 in. beam and 10.3 cm for the 6 in. beam. The average neutron energy from the DD source must be equal to or greater than the average absorbed energy per neutron due to proton, carbon, nitrogen, and oxygen recoils. The proton recoil dose when extrapolated to

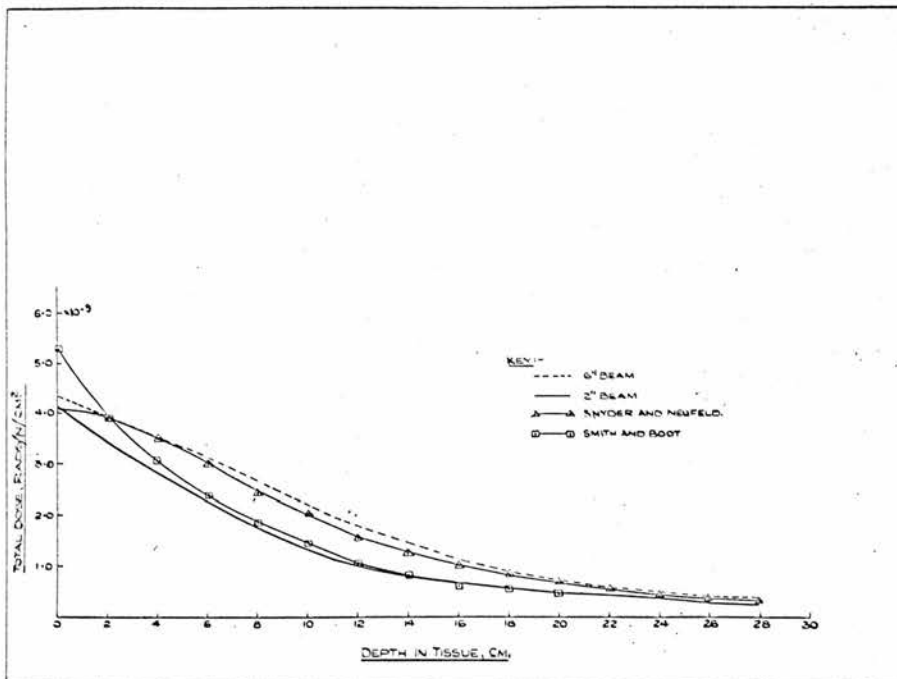


Fig. 4.9 Comparison of Published Results for the Total Dose in Rads due to DD Neutrons.

infinity contributes 2.32 Mev for the 6 in. beam. When a 7% correction is applied to account for the energy lost due to heavy recoils the total neutron energy is 2.48 Mev which is in excellent agreement with the incident neutron energy of 2.5 Mev and provides support to the experimental measurement of the dose curve.

The surface dose from the 6 in. beam is 4.25×10^{-9} rads per n cm^{-2} . Since the first collision proton recoil dose as defined in NBS 85 is 3.05×10^{-9} rads per n cm^{-2} , the ratio of the multiple collision dose to kerma is 1.39. Snyder, in NBS 63, estimated that this ratio would be 1.29. The difference in the two ratios is due to the difference in the experimental and theoretical surface doses for multiple collisions. This becomes negligible if Snyder's curve is extrapolated smoothly back to the surface instead of bending over.

There is seen to be good agreement between the theory of Snyder and the present experimental measurements although it would appear that Snyder under-estimates the dose at depth after about 15 cms and over-estimates the flattening out of the curve near the front surface of the phantom.

A comparison of the total fast neutron dose at depth in a tissue-equivalent phantom, measured by Smith and Boot (1961) and this report, is shown in Fig. 4.9. This dose is the sum of the three components measured.

§4.3.2 DT Proton Recoil Dose

Fig. 4.10 shows the relative doses for the 2 in. and 6 in.

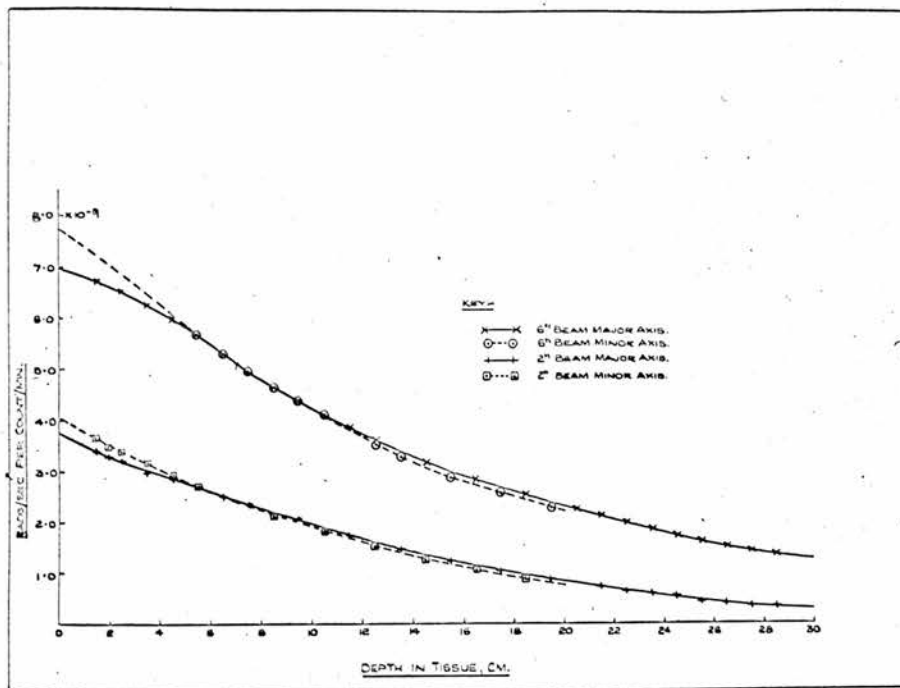


Fig. 4.10 The Recoil Proton Dose for DT Neutrons Normalised to One Count per Minute on the Standard.

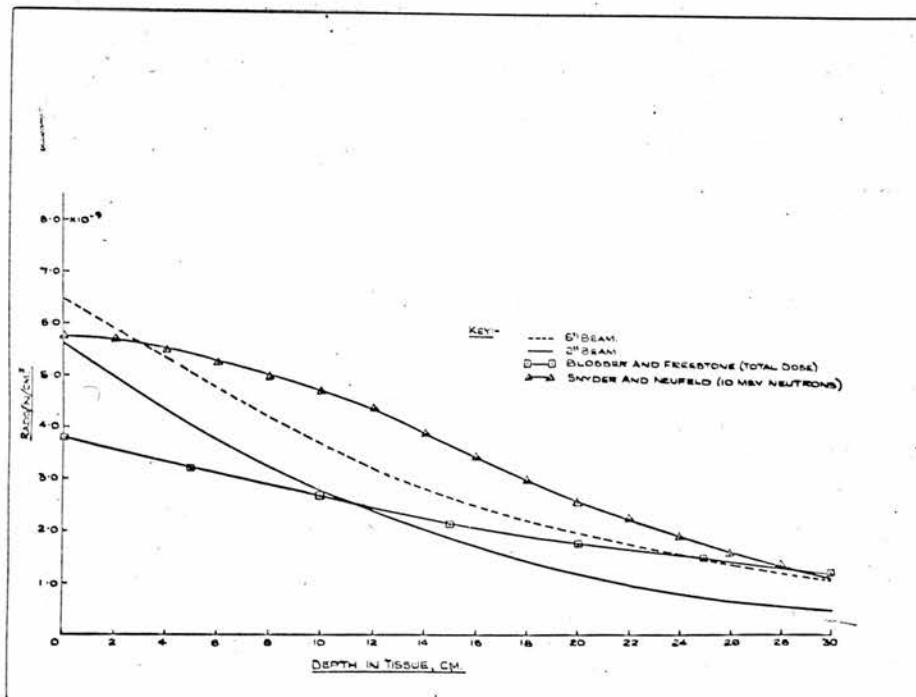


Fig. 4.11 Comparison of Published Results for the Recoil Proton Dose in Rads due to DT Neutrons.

collimated beams of DT neutrons. The curves show similar effects to the DD curves. Once again the minor axis dose is greater than the major axis dose at the front of the phantom, decreasing towards the back. The maximum difference is less than 10%.

There has been no theory published for 14 Mev multiple collision depth dose curves. The DT measurements were compared therefore with Snyder's 10 Mev values. The comparison is shown in Fig. 4.11. The dose distribution can again be approximated to exponential curves. The relaxation lengths are 13.5 cm for the 2 in. beam and 16 cm for the 6 in. beam. When the kinetic energy deposited by the proton recoils for the 6 in. beam was calculated and allowance was made for the extrapolation to infinite depth, the energy was found to be 6.1 Mev. Randolph's theory (1957) on the kerma of 14.1 Mev neutrons, in which he considered both elastic and inelastic scattering, stated that 69.5% of the total dose in tissue liquid was due to the hydrogen present. Since the present measurements indicated that the average proton energy and hence spectrum shape of the incident neutrons did not change appreciably with depth it can be assumed that the maximum proton recoil contribution to the total dose would not exceed 69.5% throughout the phantom. The kinetic energy released due to proton recoils was deduced from Randolph's calculations to be less than or equal to 9.8 Mev.

The surface dose for the DT 6 in. beam is 6.4×10^{-9} rads per cm^{-2} which is 1.38 times the first collision dose calculated by Randolph. Snyder does not extend his calculations to 14 Mev but, in

NBS 63 the ratio of multiple collision dose to first collision dose is fairly constant above 2 Mev and the 10 Mev ratio is equal to the 2.5 Mev ratio. This is also true for this report where the ratio is virtually the same for both the DD and DT neutrons.

Snyder's curve for 10 Mev neutrons provides an upper limit to the dose due to 14 Mev neutrons. Blosser and Freestone (1963) measured the total dose using an ethylene filled ionisation chamber at various depths in a sphere filled with water. According to Randolph's theory (1957) for 14 Mev neutrons interacting with water, the total dose is 1.08 times that for tissue liquid. For comparison with the present report Blosser and Freestones' results have been corrected to give the dose due to the hydrogen present in tissue by multiplying by 0.64. The kinetic energy of the incident deposited by the proton recoil reaction was calculated to be 6.0 Mev which agrees favourably with the 6.1 Mev calculated above. The shape of the dose curve, however, bears no resemblance to the 2 in. and 6 in. beam curves, also the surface dose is only 3.8×10^{-9} rads per cm^{-2} which is less than the kerma predicted by Randolph. The discrepancy remains unresolved and it must be assumed that the NE 102 phosphor technique which has proved successful for Pu-Be and DD neutrons will also provide the DT recoil proton dose.

§4.4 Dose Equivalent for Proton Recoils

The method used to calculate the dose equivalent for proton recoils, detailed in §3.7, required a knowledge of the quality factor which could be approximated by the linear relation

$$QF = 0.8 + 0.16 \bar{L}$$

where \bar{L} was the dose average LET.

In §3.7.1 \bar{L} for Pu-Be neutrons was determined by plotting a graph of the dose per unit LET interval (D_L) against the LET, (L) and computing \bar{L} from the equation.

$$\bar{L} = \frac{\overline{LET}}{LET} = \frac{\int_0^{\infty} L \cdot D_L \cdot dL}{\int_0^{\infty} D_L \cdot dL}$$

It was found, however, that \bar{L} calculated in this way agreed within a few percent of the average LET calculated by dividing the total energy deposited in the detector by the number of protons depositing the energy, and then further dividing this average proton energy by the corresponding range in water.

Since this second method is very much simpler to use than the first, the dose average LET was first calculated by the two methods at four positions in the phantom for each of the 2 in. and 6 in. DD and DT neutron beams. The two \overline{LET} values obtained for each position were found to be in agreement with each other to within $\pm 3\%$. It was therefore concluded that the dose average LET for radiation protection purposes could be calculated at each point of interest by the second simple averaging procedure. The \overline{LET} values determine the quality factor and hence the proton recoil dose equivalent.

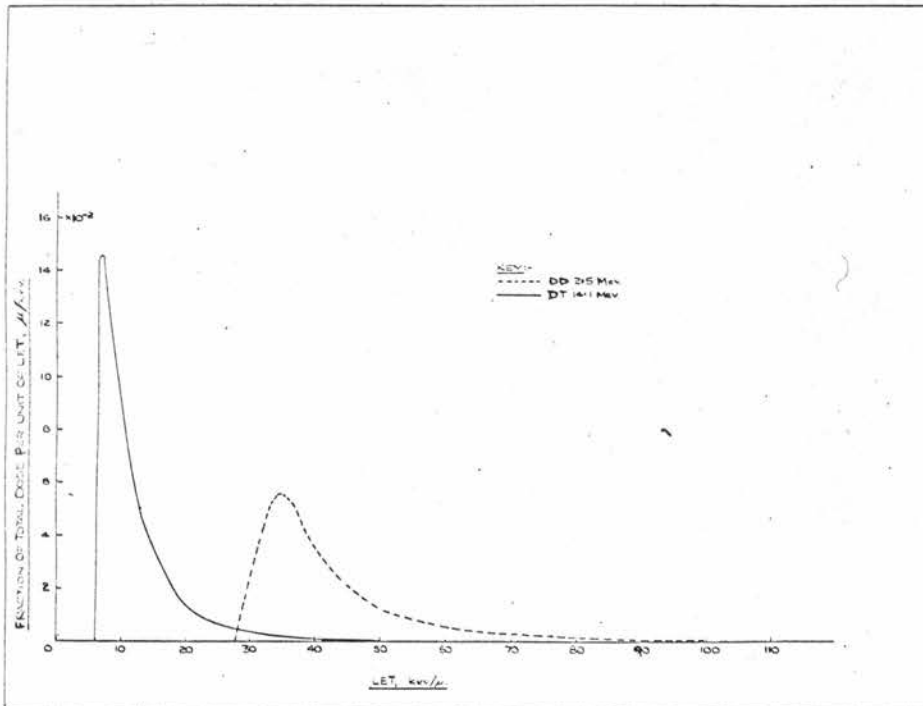


Fig. 4.12 Dose per Unit LET Interval Plotted Against the LET.

§4.4.1 Quality Factors

The quality factor for the DD source shall be considered first. The average proton energy was found to remain constant with depth in the tissue-equivalent liquid to 20 cm, beyond which it slowly decreased. This was true for both the 6 in. and 2 in. beams. Within the experimental limit it was the same for both beams, 0.93 ± 0.01 Mev, which corresponded to an average LET of $47.0 \text{ kev}/\mu$ of water and a quality factor of 8.32. Beyond 20 cm the average proton energy decreased slowly, giving a maximum quality factor at 30 cm of 8.7. This decrease in average energy is in agreement with Field (1965) who suggests that the neutron spectrum shape for an incident monoenergetic beam slowly softens at depth in the phantom due to scattering of the neutrons. A typical graph of D_L as a fraction of the total dose ($\int_0^\infty D_L dL$) plotted against the LET is shown in Fig. 4.12 for DD and DT neutrons. The area under both curves is unity. The experimental quality factor 8.32 is in excellent agreement with the proton recoil quality factor 8.20 calculated from Snyder's data in NBS 63 for 2.5 Mev neutrons.

Rossi (1955(b)) has published data on the dose as a function of LET for 3 Mev DD neutrons using his tissue-equivalent spherical proportional counter. The quality factor calculated from this data is 8.06 which should be compared with the value of 7.84 for 3 Mev neutrons taken from Randolph (1964). The quality factor should be lower than the quality factor for 2.5 Mev neutrons, and from interpolation of the quality factors in NBS 63 it was calculated to be 7.8 ± 0.2 . The experimental

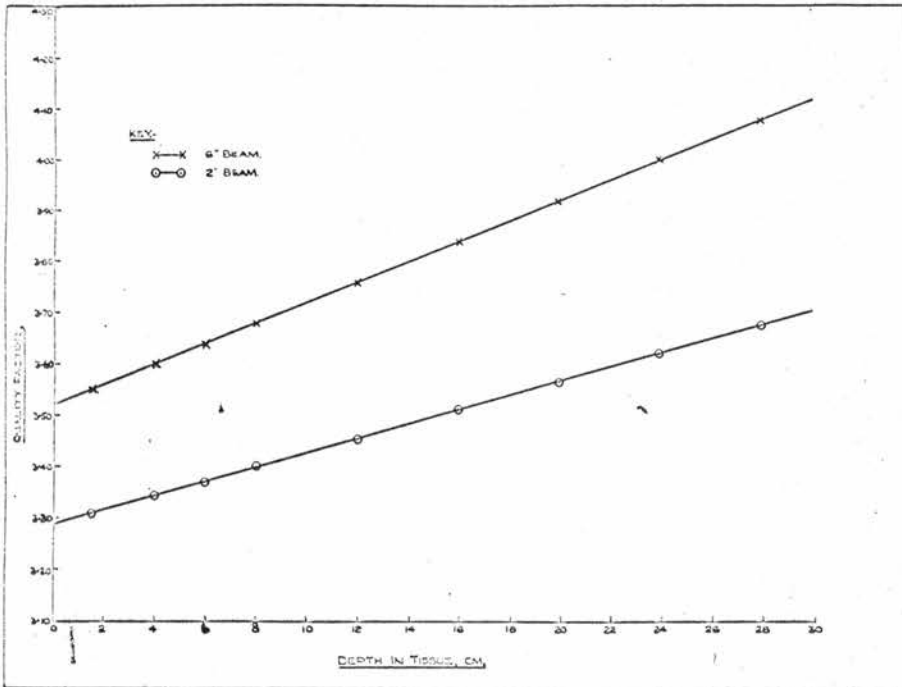


Fig. 4.13 The Quality Factor for DT Neutrons as a Function of Depth in the Phantom.

quality factors from the present report and from Rossi's data can therefore be assumed to agree.

The quality factor was calculated in the same way for the DT beams. The average proton energy did not remain constant but gradually decreased with increasing depth in the phantom for both the 2 in. and 6 in. beams. The calculated quality factor as a function of depth in the phantom could be fitted to a straight line equation in each case. Fig. 4.13 shows the quality factor values. Neutrons from the 6 in. beam, due to a larger percentage of scattered neutrons, have a softer spectrum than the neutrons from the 2 in. beam and therefore have a higher quality factor. This was also seen to be true for Pu-Be neutrons but the effect was not so marked for DD neutrons where the 6 in. beam energy was only just marginally lower than the 2 in. beam energy.

The average proton energy at the surface of the phantom was 4.52 ± 0.04 Mev for the 2 in. beam and 4.05 ± 0.04 Mev for the 6 in. beam. The magnitude for the 6 in. beam was therefore 10% less than that for the 2 in. beam. The quality factors for the beams as a function of depth could be approximated by the equations

$$QF = 0.014X + 3.29 \text{ for the 2 in. beam, and}$$

$$QF = 0.020X + 3.52 \text{ for the 6 in. beam}$$

where X was the depth in tissue.

The maximum variation in the quality factor in the phantom was for the 6 in. beam where it rose from 3.52 to 4.12 which represented an increase of 17%. The corresponding increase for the 2 in. beam was less

than 13%. Bateman et al (1961) found values of \bar{L} from RBE measurements for several neutron energies and extrapolated to 14 Mev to obtain a value of \bar{L} equal to 20 kev/ μ which corresponds to a quality factor of 4. Conger et al (1958) calculated \bar{L} for protons to be 16 kev/ μ , with a quality factor of 3.36. This was later modified by Randolph (1964), using the stopping power of protons given by Neufeld and Snyder (1961), to give \bar{L} equal to 25 kev/ μ and QF equal to 4.8. Since the stopping power values of Neufeld and Snyder have not yet been verified experimentally, this value for \bar{L} may be over-estimated. When the quality factors for protons in NBS 63 were extrapolated to 14 Mev the quality factor was found to be 3.8 ± 0.5 . This must, however, be considered only as a rough estimate due to the lack of sufficient data.

A survey of the literature has not produced evidence of any direct attempt to measure or estimate the quality factor of proton recoils produced by 14 Mev neutrons. The quality factors quoted above were inferred from the energy average LET values published by the various authors who were interested primarily in LET values for RBE measurements. The accuracy of the quality factors determined experimentally for 14 Mev neutrons cannot, therefore, be compared directly with any published evidence. Indirect calculations indicate that they are of the correct order of magnitude.

It is concluded that when the quality factors for the 6 in. beams are determined experimentally they agree with the theoretical predictions of Snyder. Further, the error in assuming that the quality factor remains

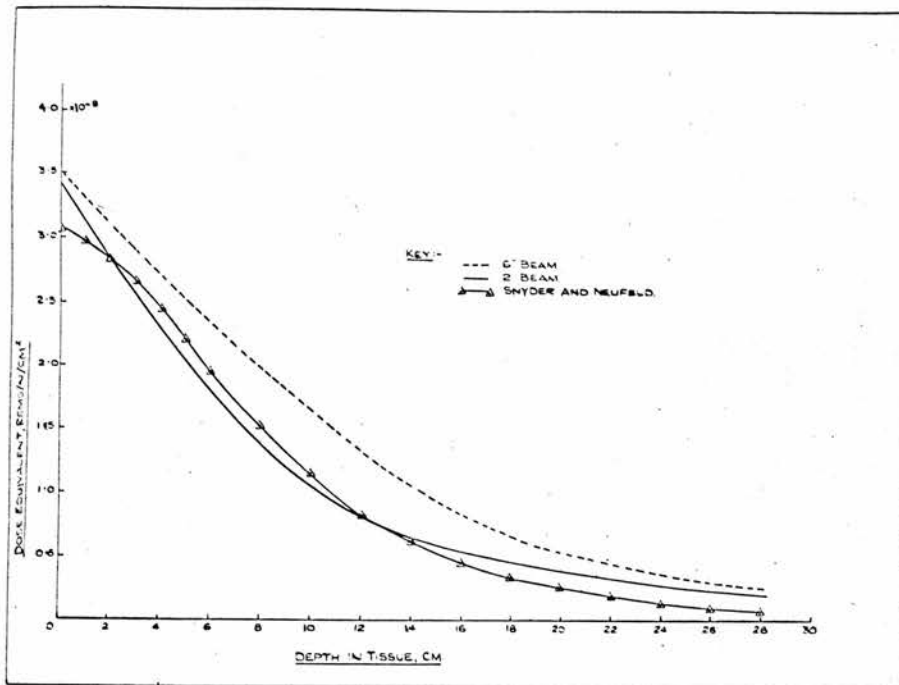


Fig. 4.14 Dose Equivalent for Proton Recoils from DD Neutrons. The total dose equivalent for proton recoils, $^{14}\text{N}(n,p)^{14}\text{C}$ and $^1\text{H}(n,\gamma)^2\text{D}$ events is effectively the same curve since the capture reactions contribute less than 2%.

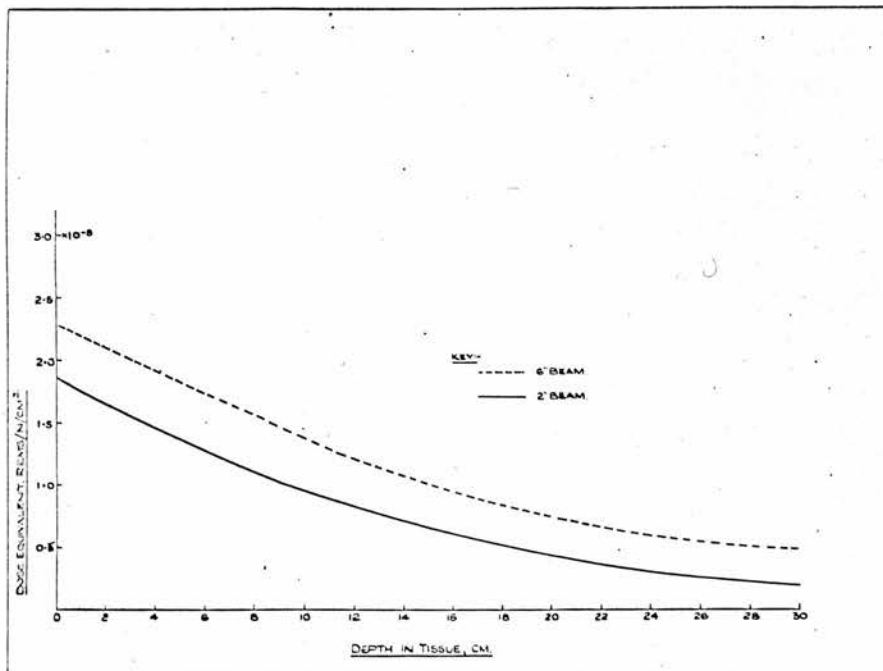


Fig. 4.15 Dose Equivalent for Proton Recoils from DT Neutrons. The total dose equivalent for proton recoils, $^{14}\text{N}(n,p)^{14}\text{C}$ and $^1\text{H}(n,\gamma)^2\text{D}$ events is effectively the same curve since the capture reactions contribute less than 2%.

constant with depth is less than 5% in the worst position which is at the back of the phantom. The average error will therefore be considerably lower. The simplicity of operation and relative compactness of the NE 102 Bragg-Grey detector compared to Rossi's 4 in. diameter counter and the associated complex analysis of the pulse heights, suggests that the NE 102 technique is more suitable for general use, although both methods give the same results. The phosphor, for example, could be used to determine the $\overline{\text{LET}}$ at various depths in a rat, whereas the proportional counter dimensions set a limitation on its usefulness.

§4.4.2 Dose in Rems

The dose equivalent of the proton recoils for the 2 in. and 6 in. DD beams, calculated from the absorbed dose and the quality factor 8.32, are compared with Snyder's theoretical dose equivalent from NBS 63 in Fig. 4.14. Since the quality factor 8.20 from Snyder's data was almost the same as that determined in this report Fig. 4.14 is essentially the same as Fig. 4.8 with the ordinate multiplied by 8.32 and expressed in rem instead of rads.

The ${}^1\text{H}(n, \gamma) {}^2\text{D}$ events contribute a maximum of 1.4% to the total rem dose for the three components, and the ${}^{14}\text{N}(n, p) {}^{14}\text{C}$ contribution is less than 1/3%. Theoretically Snyder calculated a maximum of 3% for the ${}^1\text{H}(n, \gamma) {}^2\text{D}$ reaction and 2% for the ${}^{14}\text{N}(n, p) {}^{14}\text{C}$ reaction. The sum of the dose equivalents for the three components, is therefore, approximately the same as shown in Fig. 4.14 for the proton recoils alone.

Fig. 4.15 shows the dose equivalent of the proton recoils for the

2 in. and 6 in. DT beams. The absorbed dose at depth was multiplied by the appropriate quality factor for that position determined from Fig. 4.13. Since the contribution to the total rem dose of the three components was again $< 1/3\%$ for the $^{14}\text{N}(n, p) ^{14}\text{C}$ reaction, and $< 1.2\%$ for the $^1\text{H}(n, \gamma) ^2\text{D}$ reaction, Fig. 4.15 is essentially the total rem dose of the components.

§4.4.3 Quality Factor for the Total Dose

Quality factors for the total dose, which includes contributions from all types of reactions, e.g. the carbon, nitrogen and oxygen recoils which have been neglected in the present report, can be found in NBS 63 for neutrons up to 10 Mev energy. No value, however, is recommended for 14 Mev neutrons. It is the purposes of this section to suggest a possible value. The 14 Mev case is complicated by the fact that there are 17 nuclear reactions contributing to the LET distribution. The first collision dose can be divided into the 69.5% contribution from recoil protons, and the 30.5% produced by all other ionising products. Randolph (1964) calculated that the energy average LET for recoil protons was 25 kev/ μ and for heavy ions it was 362 kev/ μ . The over-all energy average LET was therefore 128 kev/ μ . The equation used to determine the recoil proton quality factors

$$QF = 0.8 + 0.16 \bar{L}$$

is, however, only valid up to 100 kev/ μ of water (Report of the R.B.E. Committee 1963). It is postulated therefore, that the following method may provide a satisfactory estimate of the quality factor for the total

dose due to 14 Mev neutrons.

When the fraction of the total recoil first collision dose due to recoil protons was calculated from NBS 85, for neutron energies up to 10 Mev, it was found to be equal, to within a few percent, to the corresponding fraction of the total recoil absorbed dose in the phantom calculated from Snyder's data. The quality factor for the total recoil dose (neglecting the $^{14}\text{N}(n, p)$ ^{14}C and $^1\text{H}(n, \gamma)$ ^2D contributions) can therefore be calculated by weighting the quality factors for the recoil protons and the heavy recoils by their percentage of the total recoil first collision dose. For example, in the case of the 2.5 Mev neutrons, 93% of the dose is due to recoil protons with a quality factor of 8.2, and 7% is due to heavy ion recoils with a quality factor of 20. The weighted quality factor is therefore 9.0. This can be compared with the value 8.0 quoted in NBS 63. The difference is due to neglecting the $^1\text{H}(n, \gamma)$ ^2D contribution which is quite an appreciable fraction of the dose at 2.5 Mev. When the calculation is applied to 10 Mev neutrons, however, where the $^1\text{H}(n, \gamma)$ ^2D dose is becoming insignificant, the quality factor obtained is 6.9 which compares very favourably with 6.5 from NBS 63. The agreement should be even better at 14 Mev. Since the quality factors for the proton recoils obtained experimentally using the NE 102 phosphor, have agreed with the NBS 63 quality factors for the Pu-Be and DD sources, the 6 in. beam DT quality factor 3.52 shall also be assumed to be correct. The quality factor for the total dose can therefore be calculated to be 8.5.

It is concluded that for broad beam irradiation the quality factors in NBS 63 should be applied to the total absorbed dose to obtain the total dose equivalent in rems. Further it is suggested that the quality factor for 14 Mev neutrons should be 8.5 on the assumption that the quality factor for the recoil protons, at the surface of the phantom, obtained in this report is correct.

CHAPTER FIVE

THE LET DISTRIBUTION OF THE RECOIL PROTON DOSE

§5.1 Introduction

The LET concept was discussed in some detail in §3.7, and in §3.7.1 a mean LET suitable for determining the quality factor to be used in radiation protection was calculated. The absorbed dose is a measure of the total energy imparted by ionising particles to unit mass of the irradiated material. Since the biological effect for a given absorbed dose depends on the type of radiation used, a more explicit description of the radiation quality is required for radiobiological and radiochemical experiments. This is achieved by determining the dose as a function of the linear energy transfer, LET, and expressing it as the fraction of the total dose deposited in different LET intervals. In some radiobiological experiments which depend on a particle traversing a particular structure, the emphasis is on the distribution of track length with respect to LET. The present discussions shall be confined to the former distribution.

In §3.7.1 the dose per unit LET interval, D_L , was plotted against the LET, L . These graphs were produced on the assumption that the LET could be approximated to E/R , where E was the observed energy of the recoil proton with corresponding range R in water. While this approximation was adequate for the determination of the mean LET to be used in the quality factor calculation, it will not give the true distribution of dose with respect to LET. The latter requires the fractional

distribution of the dose with LET for each recoil ion to be integrated over the complete recoil particle spectrum and weighted to provide the fractional distribution for all the ions. The LET in this case must be defined exactly as the specific energy loss dE/dx .

The comparison between the two absorbed dose distributions can be illustrated more clearly by consideration of the principles involved. The LET for a 1 Mev proton, for example, defined as $L_r = E/R$ is 46.5 kev/ μ , whereas the LET defined as $L_x = dE/dx$ is 27.3 kev/ μ . This is not an anomaly however, since it is well known that the specific energy loss of a particle increases towards the end of its track and then falls to zero when the particle is stopped. The LET, L_x quoted is the value of dE/dx at the maximum range but as the proton slows down it will have a distribution of dE/dx 's. It can readily be shown that the mean dE/dx is equal to E/R ,

$$\text{i.e. } L_r = \frac{E}{R} = \overline{L_x} = \frac{\int_0^R L_x dx}{\int_0^R dx}$$

Thus the 1 Mev proton should have a distribution of energy deposited with LET, L_x , or, as in the approximation of §3.7.1, it can be represented as depositing all its energy E at a mean LET, L_r . The distribution of dose, D_L , as a function of LET, L_r , in §3.7.1 is clearly seen to be the distribution of dose as a function of the mean dE/dx . That is to say the graph (Fig. 3.11) is a plot of the absorbed dose per unit interval of LET, $\overline{L_x}$, against the LET, $\overline{L_x}$. The distribution to be discussed in this section,

which is of interest in radiobiological experiments, is the absorbed dose per unit interval of LET, L_x , against the LET, L_x . The fraction of the total dose is simply obtained by dividing the ordinate by the total dose.

It is obvious from this discussion that the lowest value of $\overline{L_x}$ must always be greater than the lowest L_x . This is why the distribution as a function of L_x over-estimates the theoretical peak position (§3.7.1).

The theoretical treatment of Boag (1954), and Snyder (1964), shall be compared with the experimental data of Rossi (1955), and with this report.

§5.2 Theoretical Treatment of the Distribution of Dose in LET

Boag (1954) computed the LET distribution of protons liberated in water by neutrons for two extreme irradiation conditions. When the dimensions of the irradiated material are small compared to the mean free path of the neutrons in it, each neutron may be assumed to collide only once producing recoil protons which are stopped in the material. On the other hand, when the neutron mean free path in the material is small compared to the sample size multiple collisions may occur. This situation was approximated to by considering an infinite medium containing a uniformly distributed fast neutron source. The LET was calculated from the equation

$$L(E) = \frac{7.93}{E} \ln(31.2E) \quad \dots (5.1)$$

where E is in Mev and the LET is in kev/u.

When the incident neutron energy is E_0 , the recoil protons take any

energy ϵ between zero and E_0 with equal probability, provided only first collisions take place. Each proton with an energy greater than $\epsilon + d\epsilon$ will have to traverse the energy range $\epsilon + d\epsilon$ to ϵ in coming to rest. From this, and the knowledge that the average energy dissipated per collision is $E_0/2$, Boag calculated the first collision distribution function ϕ_s of the LET of protons produced in water by monoenergetic neutrons to be

$$\phi_s [L(\epsilon)] = \frac{2 \epsilon^2 [1 - \epsilon/E_0]}{7.93 E_0 [\ln(31.2 \epsilon) - 1]} \quad \dots (5.2)$$

The distribution function ϕ_M for the multiple collision case when a monoenergetic source is uniformly distributed in an infinite medium was calculated in the same way. The essential difference is that all of the energy E_0 is now dissipated. The function was found to be

$$\phi_M [L(\epsilon)] = \frac{\epsilon^2 \ln(E_0/\epsilon)}{7.93 E_0 [\ln(31.2 \epsilon) - 1]} \quad \dots (5.3)$$

Finally the first collision distribution function ϕ_{mixed} for an incident beam of mixed energies was found to be

$$\phi_{\text{mixed}} [L(\epsilon)] = K \left\{ \int_{\epsilon}^{E_0} \int_{\epsilon}^{E_0} \frac{\sigma(E) F(E)}{E} dE d\epsilon \right\} \frac{d\epsilon}{dL} \quad \dots (5.4)$$

where E = neutron energy in Mev,

K = normalising constant,

$\sigma(E)$ = neutron elastic collision cross-section,

$F(E)$ = energy distribution of incident neutrons,

and
$$\frac{d\epsilon}{dL} = \frac{\epsilon^2}{7.93 [\ln(31.2 \epsilon) - 1]}$$

Boag considered only the dose distribution for recoil protons since they contribute most of the dose (≈ 70 to 90%). The distribution for protons, can however, be very different from the distribution for the total dose when the $^{14}\text{N}(n, p) ^{14}\text{C}$ and $^1\text{H}(n, \gamma) ^2\text{D}$ reactions and also heavy recoils are included. At low neutron energies, say 1 Mev, the thermal reactions become important, while at 14 Mev the recoil proton dose is only 70% of the total dose and the heavy recoil contribution is appreciable. This problem is at present being investigated by Snyder (1963, 1964), but due to the extreme complexity of the problem only a few preliminary results have so far been published. Fortunately some of these were for 2.5 Mev neutrons.

Snyder employed Monte-Carlo-type techniques to calculate the LET spectrum of total dose from monoenergetic beams of neutrons incident on tissue cylinders. The data obtained for a homogeneous cylindrical phantom, diameter 30 cm and height 60 cm, assumed to have the standard man composition, can be compared with the data from this report. The theory includes the $^{14}\text{N}(n, p) ^{14}\text{C}$ and $^1\text{H}(n, \gamma) ^2\text{D}$ reactions, and heavy recoils. The anisotropy of angular scattering is allowed for, but inelastic scattering is not included. The histories of 10,000 neutrons incident on the curved surface of the phantom parallel to a diameter were followed through the phantom which had been divided into 150 regions. The total dose was averaged over each region and then sub-divided into doses delivered in various ranges of LET. The formulas used for this analysis can be found in the report by Snyder (1963) which also includes

a graph of the LET against particle energy for carbon, hydrogen, nitrogen and oxygen recoils. This graph shows that the heavy recoils contribute to the dose over a very wide range of LET.

Snyder's (1964) histograms of the distribution of the total dose with LET for 2.5 Mev neutrons can be modified to allow direct comparison with the LET distribution for the recoil protons from elastic collisions obtained from this report. This can be seen from consideration of the processes which contribute to the dose. The recoil protons from elastic collisions can have any energy from 0 to 2.5 Mev which covers the LET interval from 13 kev/ μ . The heavy recoils, which have energies less than 1 Mev, can extend to several hundred kev/ μ . Proton recoils from the ^{14}N reaction have an energy of about 0.6 Mev and LET range of 38 kev/ μ to 91 kev/ μ . Finally the gamma rays from the (n, γ) reactions have an LET of about 3 kev/ μ and do not extend above 10 kev/ μ . In Snyder's 1964 report the LET scale is divided into intervals defined by the points of subdivisions 0, 3.5, 7, 15, 25, 35, 50, 62.5, 75, 87.5, 100 and 200 kev/ μ . If the contribution to the total LET dose below 7 kev/ μ and above 100 kev/ μ is neglected, the portion of the dose left is essentially due to the recoil protons. A correction must still be applied, however, for the small percentage of the dose due to the $^{14}\text{N}(n, p)^{14}\text{C}$ protons and the heavy recoil contributions below 100 kev/ μ .

§5.3 Comparisons of the Experimental Techniques

A method of experimentally determining the LET spectrum of dose, developed by Rossi and Rosenzweig (1955(a)), was discussed in §1.7.

The detector was a spherical proportional counter with tissue-equivalent plastic walls and filled with tissue-equivalent counting gas at low pressure. Pulses produced by the counter were analysed according to their height and the dose, $D(L)$ dL , delivered per interval of LET, dL , was calculated from a formula in which the pulse height spectrum was differential with respect to pulse height. The dose distributions obtained experimentally (Rossi and Rosenzweig, 1955(b)) for Pu-Be, Po-B and 3 Mev neutrons did not agree exactly with Boag's calculations. This was partly due to the impossibility of simulating the theoretical concept of the LET of a particle at a point, and partly due to the contribution from heavy recoils measured experimentally but not included in Boag's theory. If the sample of the track observed experimentally is small there will be large variations in the LET from particles of equal energy due to the discontinuous nature of the collision process. When the sample size is increased the ionising particle may lose so much energy that it can no longer be assumed to have a single LET. The LET spectrum actually present in tissue of equivalent dimensions, which will never quite agree with Boag's theory.

This technique is the only method to be found in the literature. All of the work reported by Rossi and Rosenzweig has been biased towards determining the first collision dose, and hence the distribution of dose with LET for direct comparison with the theory of Boag. This is partially due to the physical dimensions of the proportional counter which restrict its use for determining the multiple collision dose at depth in

a phantom.

The NE 102 detector used in this report is not large and it is suggested that the LET spectrum for the recoil proton dose can be determined from the experimental dose measurements. The spectra so obtained will not agree exactly with Boag's theoretical predictions but will provide a picture which is representative of the events that would actually take place in tissue. While Rossi's distributions will resemble Boag's first collision dose treatment, the NE 102 detector measurements must resemble the multiple collision dose analysis.

Due to the multiple collisions, the recoil proton spectra, as a function of energy, do not assume rectangular distributions but are greatly enhanced at low proton energies. Wall and end effects in the phosphor also increase the number of low energy protons at the expense of the high energy protons. This will therefore lower the peak of the dose distribution as a function of LET compared to Boag's first collision treatment. The proton dose distribution as a function of LET can be calculated directly from the experimental data already used to determine the absorbed dose at depth in tissue. The technique of determining the latter was described in Chapter 3. Proton recoil spectra, measured at various depths in the tissue-equivalent phantom using a Laben multi-channel height analyser, were corrected for the energy response of the phosphor and heavy recoils using Appendix (2). From the applied corrections the true number of recoil protons per channel, for each channel, were obtained. The proton dose LET spectrum

can now be determined for monoenergetic neutrons by modifying Boag's first collision dose theory. Each proton whose energy, determined by the phosphor, exceeds $\epsilon + d\epsilon$ must traverse the energy range $\epsilon + d\epsilon$ to ϵ in coming to rest. The proportion of the total energy dissipated is therefore $d\epsilon/\bar{E}_p$ where \bar{E}_p is the average proton energy which has already been calculated for the neutron sources involved in this report in order to determine the quality factor. For example, for DD neutrons it was 0.93 Mev. When there are N protons with energy greater than $\epsilon + d\epsilon$ the proportion is $Nd\epsilon/\bar{E}_p$ and if these N protons represent the fraction, F, of the total number of protons, then the recoil proton distribution functions using the NE 102 phosphor, $\phi(L)_{NE\ 102}$, can be obtained from the relation

$$\left[\frac{F}{\bar{E}_p} \cdot \frac{d\epsilon}{dL} \right] dL = \phi(L)_{NE\ 102} \cdot dL \quad \dots (5.5)$$

This is similar to Boag's formulation for the first collision dose

$$\left[\frac{2}{E_0} \cdot N(\epsilon) \cdot \frac{d\epsilon}{dL} \right] dL = \phi(L)_s \cdot dL \quad \dots (5.6)$$

where the fraction of recoil protons above energy E is $N(\epsilon)$, and E_0 is the incident neutron energy.

Thus by equating (5.5) and (5.6)

$$\phi(L)_{NE\ 102} = \frac{F}{2} \cdot \frac{E_0}{\bar{E}_p} \cdot \frac{1}{N(\epsilon)} \phi(L)_s \quad \dots (5.7)$$

The quantity $\frac{\phi(L)_s}{N(\epsilon)}$ can be obtained for any neutron energy using Appendix (3) which is a computer programme designed to operate on an I.B.M. 1620 computer. The programme will provide Boag's distribution

functions for monoenergetic neutrons defined by equations (5.2) and (5.3), as well as the factor $\frac{\phi(L)_s}{N(\epsilon)}$.

The recoil proton distribution function can therefore be obtained from equation (5.7) for any monoenergetic neutron source at any point in the phantom. Boag's theory for fast neutron beams of mixed energies has not been modified to suit the NE 102 detector measurements for the Pu-Be source. This is due to lack of knowledge of $F(E)$, the energy distribution of incident neutrons, in equation (5.4). Rossi and Rosenzweig (1955(b)) calculated ϕ_{mixed} from equation (5.4) for Pu-Be neutrons using the data of Perlman (1946) for $F(E)$. Since the latter report has not yet been obtained at Chapelcross, the Pu-Be data could not be analysed.

The proton recoil dose distribution as a function of LET was therefore calculated from equation (5.7) for the DD and DT neutron beams and compared with theory.

§5.4 The Experimental Distribution of Dose Using the NE 102 Detector

§5.4 (a) For DD Neutrons

The fraction of the absorbed dose per unit interval of LET, $\phi(L)_{\text{NE 102}}$, was calculated for the 2 in. and 6 in. beams traversing the major and minor axes of the phantom. The average recoil proton energy (§4.4.1) was 0.93 ± 0.01 Mev up to 20 cm depth in the phantom, beyond which it gradually decreased. When the values obtained for $\phi(L)_{\text{NE 102}}$ for the major and minor axes of both beams were compared, they were found to be independent of the axes. It was also seen that the dose

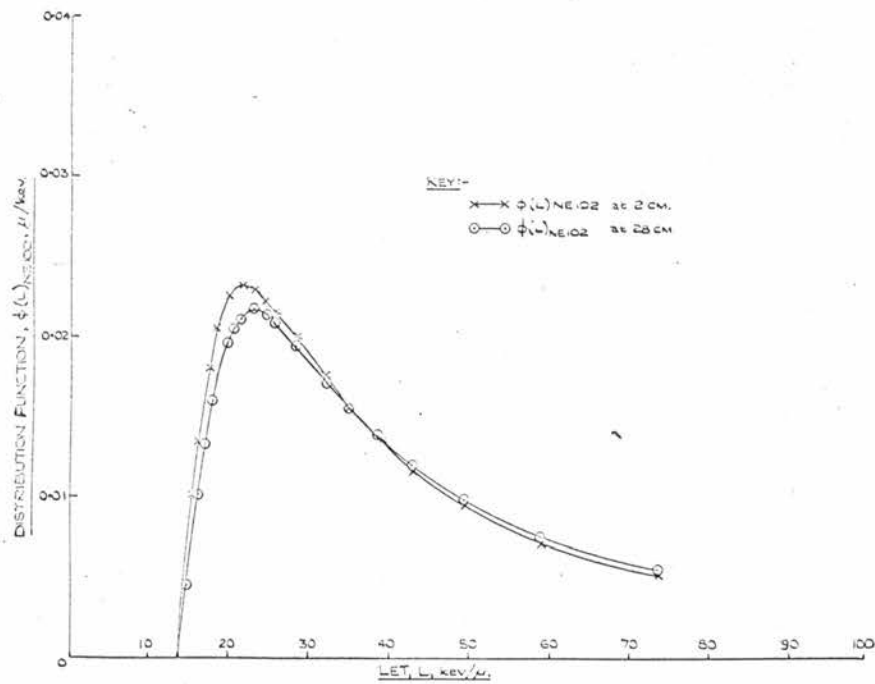


Fig. 5.1 LET Distribution of Absorbed Energy for DD Neutrons.

distribution curve was essentially the same for both the 2 in. and 6 in. beams when determined at the same point. The two curves could not be separated statistically, but the 6 in. beam distribution was consistently 2% higher in the peak. This is due to the 6 in. beam recoil proton energy being slightly lower than the average 0.93 Mev. The discussion shall now be restricted to the 2 in. beam major axis dose calculations.

The variation of the distribution shape with depth in tissue is illustrated in Fig. 5.1. At the back of the phantom, where the average recoil proton energy decreased to 0.86 Mev, the peak value of the distribution $(\phi(L)_{NE 102})$ also decreased and moved towards a higher LET. When the magnitude and position of the peak values were extrapolated back to 0 cm depth in the tissue the peak was found to be at $21.5 \pm 0.5 \text{ kev}/\mu$ with a magnitude of $(2.4 \pm 0.1) \times 10^{-2}$. At 28 cm depth in the tissue-equivalent phantom, the corresponding values were $23.0 \pm 0.5 \text{ kev}/\mu$ and $(2.2 \pm 0.1) \times 10^{-2}$. This is to be expected since at the back of the phantom the neutron spectrum shape will be softer than the original incident neutron spectrum. From Boag's data it can be seen that as the incident neutron energy decreases the peak magnitude ^{decreases} and moves towards a higher LET. The exact neutron spectrum shape in the phantom is, however, unknown and the experimental data must be analysed on the basis of a monoenergetic beam. Since the average recoil proton energy has only changed from 0.93 Mev to 0.86 Mev, a decrease of 8%, this assumption should not introduce too large an error in the experimental values of $\phi(L)_{NE 102}$ for protons in tissue. The result is to over-estimate the

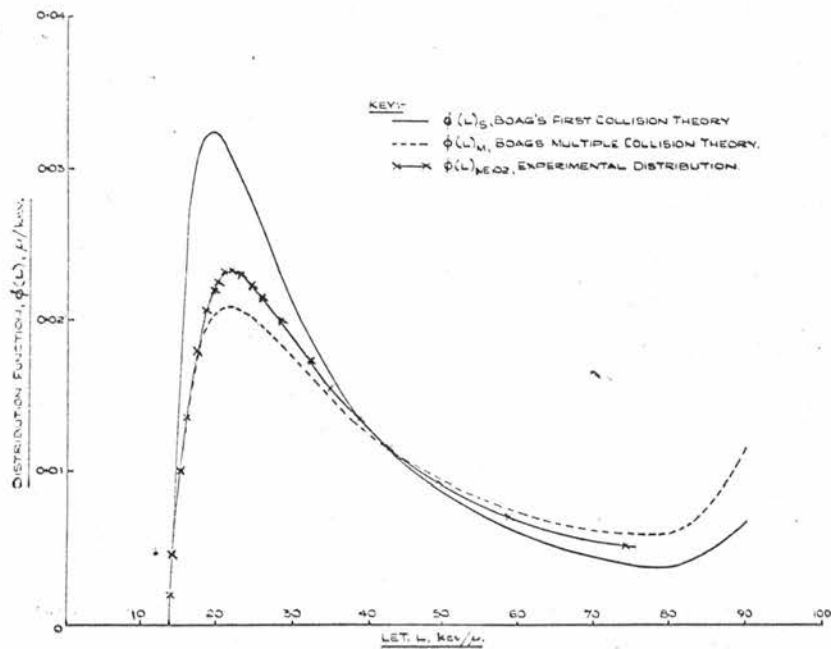


Fig. 5.2 Comparison of the Measured LET Distribution of Absorbed Energy with Boag's Theoretical Curves, for 2.5 MeV Neutrons.

magnitude of the distribution functions.

The experimental distribution of dose with LET is compared with the first collision dose and "multiple collision" dose theories of Boag in Fig. 5.2. The experimental distribution was measured at 2 cm depth in the phantom but due to the slow variation in the shape of the distribution function with depth it can be assumed to provide a measure of the distribution immediately below the phantom surface. The curve was found to lie between the two extremes predicted by Boag. Table 5.1 summarises the data obtained for ϕ_s , ϕ_m , and $\phi_{NE\ 102}$ defined by equations (5.2), (5.3), and (5.7) respectively.

Table 5.1

The Magnitude and Position of the Peak of the Dose Distribution

Distribution Function Parameter	ϕ_s (Boag)	ϕ_m (Boag)	$\phi_{NE\ 102}$ (Experimental)
Magnitude	0.0324	0.0209	0.0240 ± 0.0010
Position	19.5 keV/ μ	21.5 keV/ μ	21.5 ± 0.5 keV/ μ

The experimental distribution peak position is therefore seen to agree with the value predicted by Boag for the simulated multiple collision case, and the magnitude lies between the extreme conditions represented by the two theories. The variation between Boag's theories, and the experimental distribution at any depth can easily be found by

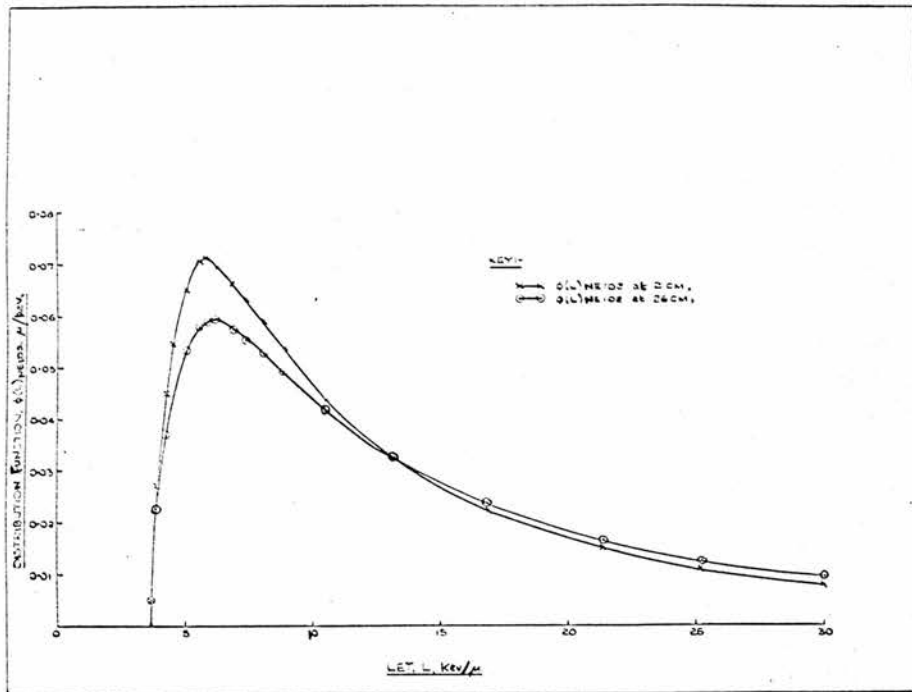


Fig. 5.3 LET Distribution of Absorbed Energy for DT Neutrons from the 2 in. Collimator.

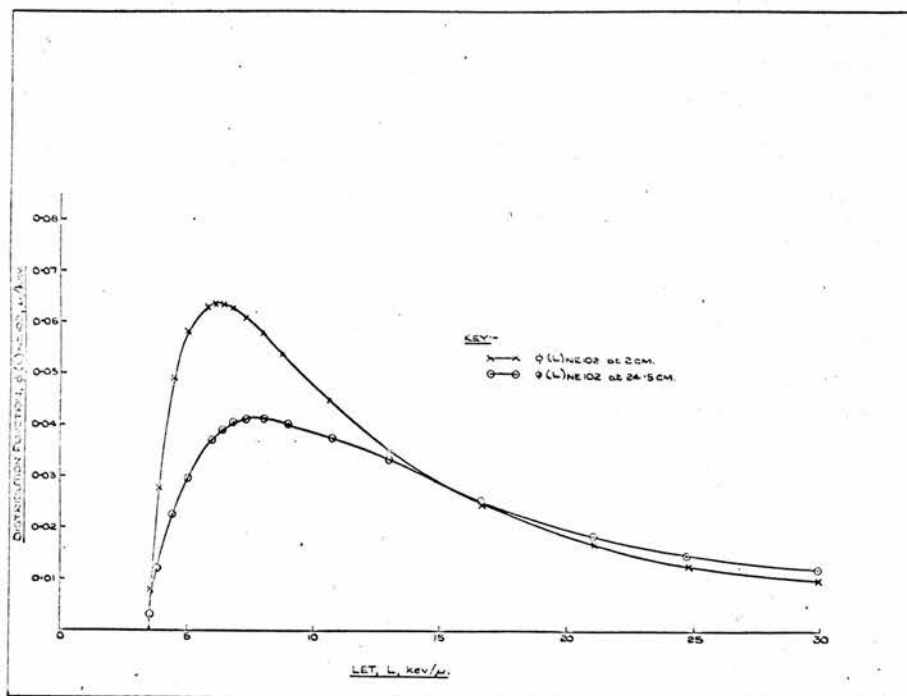


Fig. 5.4 LET Distribution of Absorbed Energy for DT Neutrons from the 6 in. Collimator.

comparing Fig. 5.1 and 5.2. It is of interest to estimate the average energy of the neutron beam at the back of the phantom. At 28 cm the LET peak occurred at 23 kev/ μ . This is the position of the peak expected for an incident monoenergetic beam of energy 2.30 Mev. It is therefore postulated that the average energy of the neutron spectrum at the back of the phantom is 2.3 ± 0.1 Mev.

§5.4 (b) For DT Neutrons

The major and minor axes values of $\phi(L)_{NE 102}$ were again found to agree. The 2 in. and 6 in. beam distribution functions, however, were quite different when determined at the same point. This is due to the difference in the average recoil proton energy which indicates a difference in the neutron spectrum. It was shown in §4.4.1 that the average proton energy varied with depth in tissue and also with the beam size.

The energy can be represented by the equations

$$\bar{E}_p = 4.52 - 0.028 x \text{ for the 2 in. beam,}$$

$$\text{and } \bar{E}_p = 4.05 - 0.035 x \text{ for the 6 in. beam,}$$

where x is the depth in the phantom.

The variation of the distribution curve with depth in tissue is shown in Fig. 5.3 for the 2 in. beam, and in Fig. 5.4 for the 6 in. beam. It can be seen that the shape changes appreciably with the depth in tissue in both cases. For the 2 in. beam, at 2 cm the peak magnitude is 0.0720, while at 26 cm it is only 0.0594. The difference between 0 cm and 30 cm position will be even greater ($\approx 25\%$). The position of the peak also changes, at 2 cm it is 5.75 kev/ μ , whereas at 26 cm it is

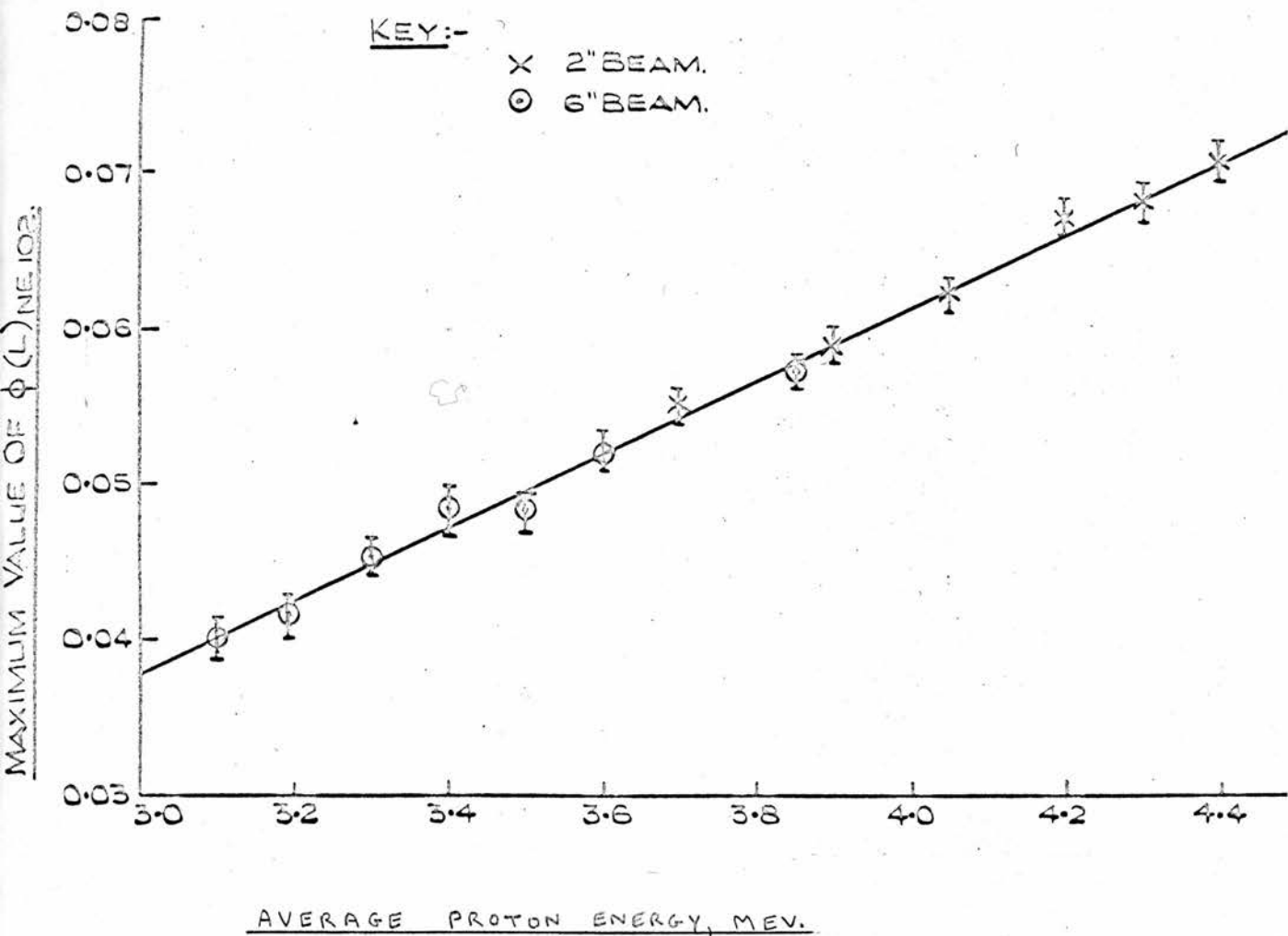


Fig. 5.5 Maximum Value of the LST Distribution as a Function of Proton Energy.

6.25 keV/ μ . Similarly, from Fig. 5.4 the magnitude of 6 in. beam distribution peak changes from 0.0634 at 2 cm to 0.0417 at 24.5 cm, with a corresponding change in position of 6.10 keV/ μ to 7.80 keV/ μ .

The magnitude of the peak was plotted against the proton energy for both beams (Fig. 5.5). It was possible to draw a straight line through the points to find the magnitude for a proton of energy 4.52 Mev. This is the value to be compared with theory since it corresponds to the position of minimum scatter of the incident beam. It was found to be 0.073 ± 0.001 and is compared with the theoretical values in Table 5.2.

Table 5.2

The Magnitude and Position of the Peak of the Dose Distribution

Distribution Function Parameter	ϕ_s (Boag)	ϕ_m (Boag)	$\phi_{NE 102}$ (Experimental)
Magnitude	0.1133	0.0719	0.0730 ± 0.0010
Position	4.95 keV/ μ	5.5 keV/ μ	5.7 ± 0.2 keV/ μ

The experimental value again lies between the two theoretical extremes. The position of the peak, however, is greater than that predicted for the "multi-collision case". This is due to scatter of the neutrons in the collimator. The beam which actually strikes the phantom has a lower average neutron energy than the initial 14 Mev. By considering Boag's multiple collision theory it would appear that

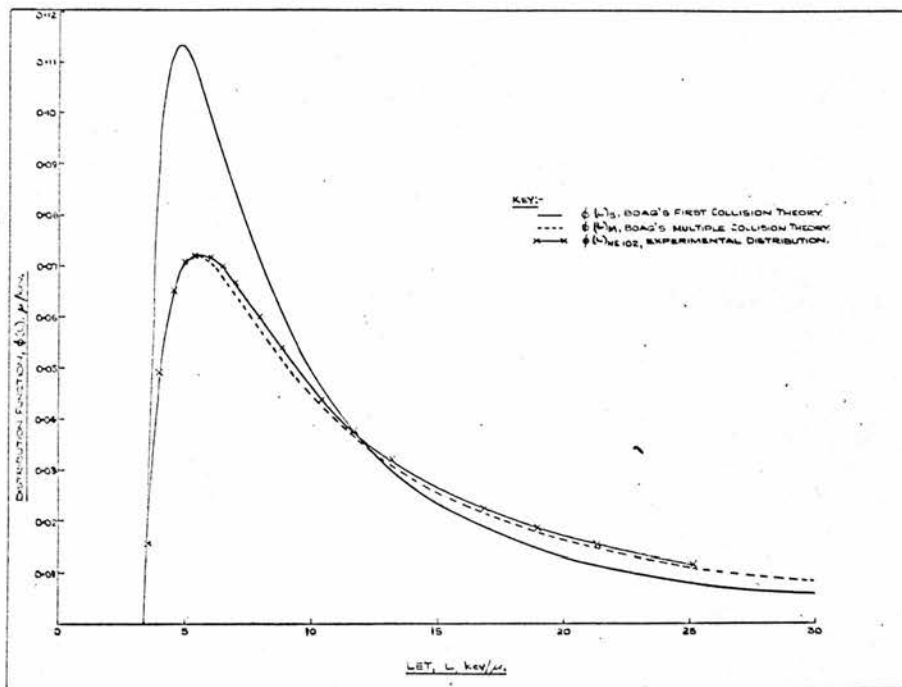


Fig. 5.6 Comparison of the Measured LET Distribution of Absorbed Energy with Boag's Theoretical Curves, for 14.1 MeV Neutrons.

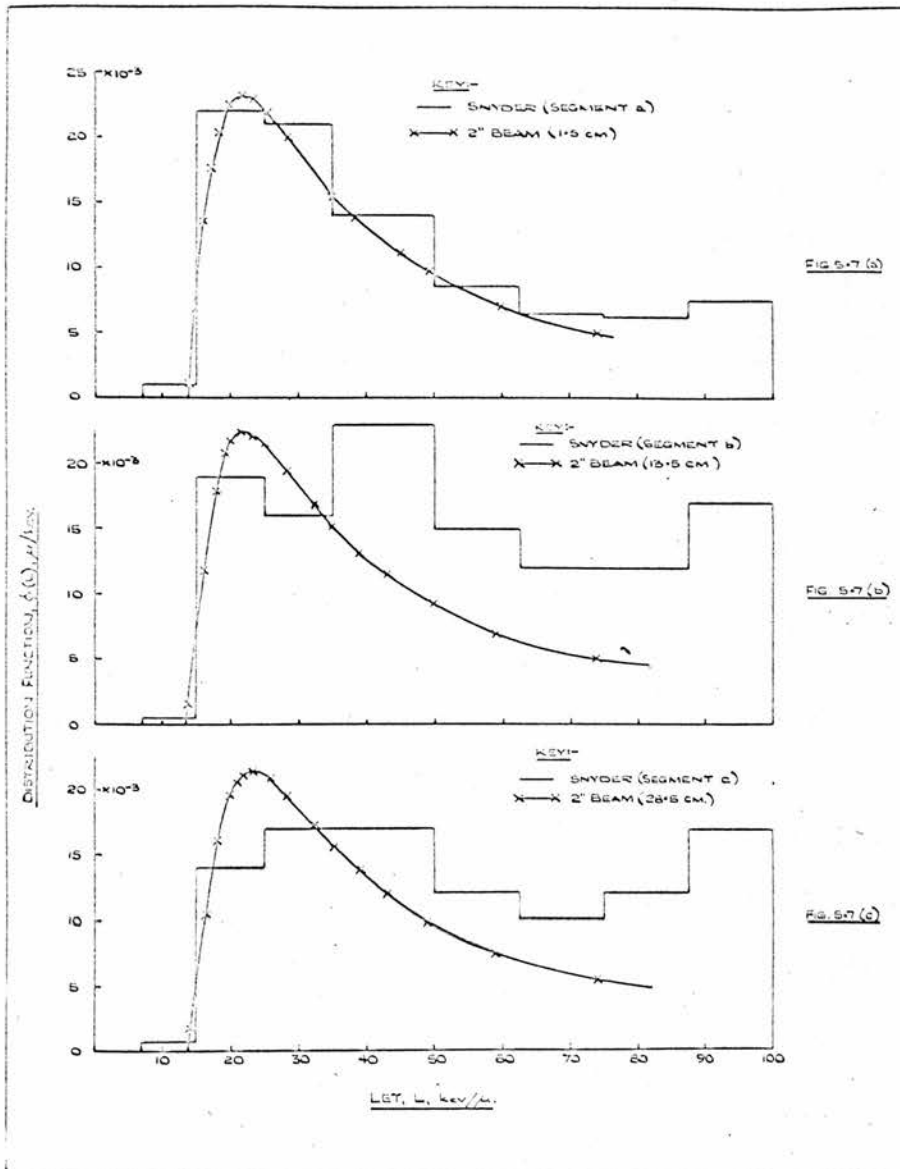


Fig. 5.7 Comparison of the Measured LET Distribution of Absorbed Energy with Snyder's Histograms, for 2.5 MeV Neutrons.

the average incident neutron energy for the 2 in. beam is 13.4 ± 0.5 Mev, and for the 6 in. beam it is 12.3 ± 0.5 Mev. The 2 in. beam 2 cm dose distribution is compared with theory in Fig. 5.6.

It can be concluded that the NE 102 phosphor technique will allow the recoil proton distribution of dose as a function of LET to be measured at any point in the phantom. The position of the peak on the surface of the phantom corresponds to the position determined by Boag's multiple collision theory, and the magnitude lies between the two extreme theories. At depth in the phantom when the average proton energy is decreasing due to the neutron spectrum becoming softer, the magnitude of the peak decreases and the curve broadens, with an increase in the value of $\phi(L)$ at high LET values. The peak position also moves to higher LET values.

§5.5 Comparison of the NE 102 Measurements with Snyder's Calculations

Snyder's data (ORNL - 3697) was modified by the method suggested in §5.2. The fraction of the dose as a function of LET was determined between the limits of $7 \text{ kev}/\mu$ to $100 \text{ kev}/\mu$ for the three positions given in the report. The dose was actually calculated for segments in the phantom and not unique positions. These segments, which shall be called a, b, and c, extended over 0 cm to 3 cm, 12 cm to 15 cm, and 27 cm to 30 cm respectively, on the top surface of the phantom. The distribution, denoted by $\phi(L)_{\text{Snyder}}$, is shown in Fig. 5.7 for segments a, b, and c.

It can be seen that the distribution changes shape drastically with

the depth in the phantom. Some of the dose is due to recoil protons from the $^{14}\text{N}(n, p) ^{14}\text{C}$ reaction. Calculations indicate, however, that this contribution is never more than 3% of the total dose. Also, the distribution of the dose with LET for these protons, which have an energy of ≈ 0.6 Mev, is fairly even. It can be concluded that their contribution does not appreciably affect the recoil proton (from elastic collisions) distribution. A second contamination is the fraction of the heavy recoil dose which lies below $100 \text{ keV}/\mu$. In NBS 63 the heavy recoil dose is approximately 7.5% of the total recoil dose at all points in the phantom. For segments a, b, and c the percentage of the total recoil dose due to heavy recoils with LET greater than $100 \text{ keV}/\mu$, is 3.3, 5.6 and 1.1% respectively, which could imply that 4.2, 1.9, and 6.4% of the total dose below $100 \text{ keV}/\mu$ is due to heavy recoils. If this is true, the effect would be to increase $\phi(L)$ at high LET at the expense of $\phi(L)$ at low LET since the total area under the distribution must be unity. This would not be sufficiently large to account for the changes shown in Fig. 5.7.

Quality factors determined for the total dose in each of the three segments are compared with the corresponding quality factors from NBS 63 in Table 5.3.

Table 5.3Comparison of Quality Factors for the Total Dose

ORNL - 3697		NBS 63	
Segment	Quality Factor	Depth in Tissue	Quality Factor
a	7.0	1.5 cm	8.0
b	6.9	13.5 cm	6.2
c	7.3	28.5 cm	3.5

Due to the large statistical errors in the data from the histograms in ORNL 3697, an uncertainty of ± 0.5 should be allocated to the calculated quality factors. From Table 5.3 the quality factors from ORNL - 3697 remain almost constant while those from NBS 63 change appreciably with depth. The large decrease in the quality factors from NBS 63 is due to the increasing importance of the $^1\text{H}(n, \gamma) ^2\text{D}$ contribution to the total dose, which varies from 10% at the front of the phantom to 70% at the back. When the data of ORNL - 3697 is modified to have the same percentage contribution to the total dose from gamma rays, as in NBS 63, the quality factor for segment c becomes 3.5 which is in agreement with the NBS 63 value. The uncertainties in the data from ORNL - 3697 are at present very large, since the computer programme is still in the preliminary stage. The only conclusions which can be reached regarding the histograms published so far is that the

Monte Carlo technique used to determine the gamma distribution underestimates the gamma contribution to the total dose.

The distribution of the dose with LET between the limits 7.0 keV/ μ to 100 keV/ μ , for a, b, and c, are compared with the distributions obtained using the NE 102 phosphor at equivalent positions. There is seen to be reasonable agreement at the front of the phantom, Fig. 5.7(a), but at the mid-point and back of the phantom, the agreement is very poor (Figs. 5.7 (b) and 5.7 (c)). The theory predicts a much larger change in magnitude and position of the peak than was actually found with the phosphor. It implies that the average energy of the neutron beam is rapidly decreasing. This is contrary to the findings of this report, and the work of Field et al (1965). It must be concluded, therefore, that the theoretical predictions of dose distribution with LET at depth in a phantom, from ORNL - 3697, are incorrect.

CHAPTER SIX

THERMAL NEUTRON DEPTH DOSE DEPENDENCE ON BEAM AND PHANTOM SIZE

§6.1 Introduction

The investigation of the thermal neutron dose at depth in a phantom from thermal neutrons produced by the moderation of Pu-Be, DD and DT fast neutrons, was extended in an attempt to find a relation between the dose and the phantom size for different collimated beams. It has already been shown that the thermal dose is much more dependent on the scattering of the incident beam than is the recoil proton dose. Hence the thermal dose can be expected to vary according to the phantom size and the collimated beam of neutrons. Since the thermal dose due to the $^{14}\text{N}(n, p) ^{14}\text{C}$ or $^1\text{H}(n, \gamma) ^2\text{D}$ reaction is directly proportional to the thermal neutron flux density, only the thermal flux need be considered. It was observed during the course of the experiments that most of the effects were common to both the Pu-Be source and the monoenergetic sources. Where this is so, detailed investigations were confined to the Pu-Be source, any relevant data for the DD and DT sources being obtained when required.

§6.2 Variation of Fast Neutron Flux with Beam Size

The neutron flux for five collimated beam sizes was determined using two slabs of phosphor, one 0.65 cm thick and the other 0.05 cm thick, for the Pu-Be source. The mean value of the fluxes is shown in Table 6.1

Table 6.1Fast Neutron Flux for Assorted Beam Sizes

Collimated Beam Diameter	Fast Neutron Flux
Inches	$10^3 \text{ n cm}^{-2} \text{ sec}^{-1}$
2	5.56
3	6.72
4	7.18
6*	8.02

*The 6 in. beam is a square beam.

The error in individual flux measurements is $\pm 4\%$ but relative to each other the error is less than 1%.

§6.3 Thermal Neutron Flux due to Assorted Beams of Incident Fast Neutrons

The thermal neutron flux was measured at various depths in a rectangular phantom, dimensions 20 cm \times 30 cm \times 40 cm, with the 4 mm thick by 4 mm diameter LiI(Eu) crystal detector described in §3.2. The irradiation conditions and techniques used were also described in Chapter 3. The values of the thermal neutron fluxes quoted below in Table 6.2 were corrected for flux depression and normalised to unit incident fast neutron flux using the fluxes in Table 6.1. The normalised thermal neutron fluxes for fast neutron beams traversing the

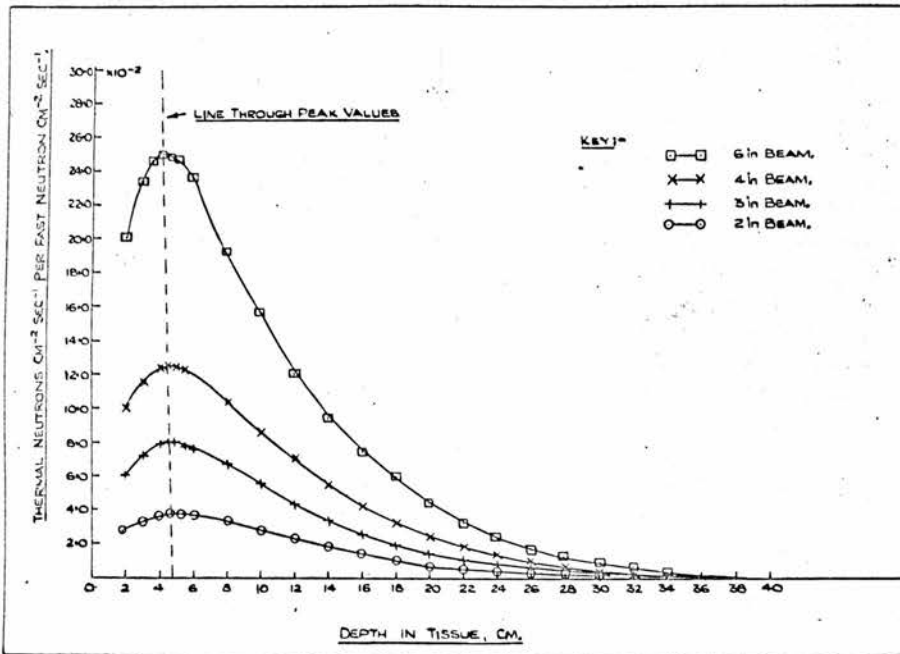


Fig. 6.1 Variation of Normalised Thermal Neutron Flux with Beam Size for Incident Pu-Be Neutrons.

major[†] axis of the phantom are shown in Fig. 6.1. The magnitude of the maximum flux for the various beams is recorded in Table 6.2 and the ratio of this flux to the corresponding flux for the 2 in. beam is compared with the beam area relative to the 2 in. beam area.

Table 6.2

(1)	(2)	(3)	(4)	(5)
Beam Diameter	Beam Area Relative to 2 in. Beam Area	Normalised Thermal Neutron Flux	Normalised Thermal Neutron Flux Relative to 2 in. Flux	Ratio of Column 4 to Column 2
inches		th. n cm ⁻² sec ⁻¹ per fast n cm ⁻² sec ⁻¹		
6*	11.44	25.00 × 10 ⁻²	6.58	0.58
4	4.00	12.46 × 10 ⁻²	3.28	0.82
3	2.25	8.05 × 10 ⁻²	2.12	0.94
2	1.00	3.80 × 10 ⁻²	1.00	1.00

*6 in. beam is a square beam.

Fig. 6.1 shows a small displacement of the peak position at depth towards the front face of the phantom as the beam diameter is increased. The thermal neutron flux peak value lies at 4.0 ± 0.1 cm for the 6 in. beam compared to 4.6 ± 0.1 cm for the 2 in. beam. This represents a

[†]Note:- The phantoms used in this experiment had rectangular cross-sections. The "major" axis is defined to be the larger of the two cross-section axis, and the minor axis is the smaller axis (cf. an ellipse).

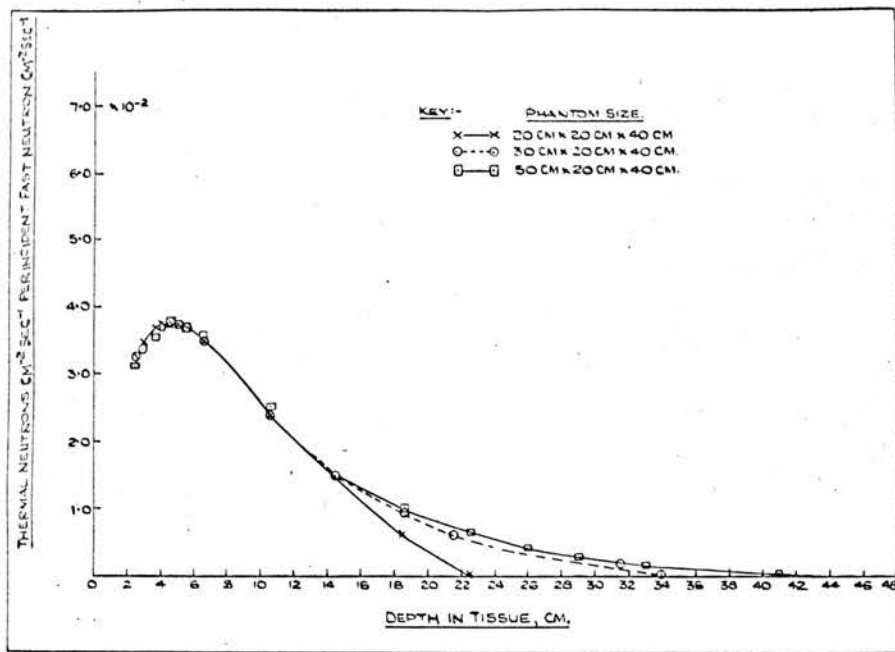


Fig. 6.2 Thermal Neutron Flux from 2 in. Beam Pu-Be Neutrons for Assorted Phantom Sizes Measured Along the Major Axis.

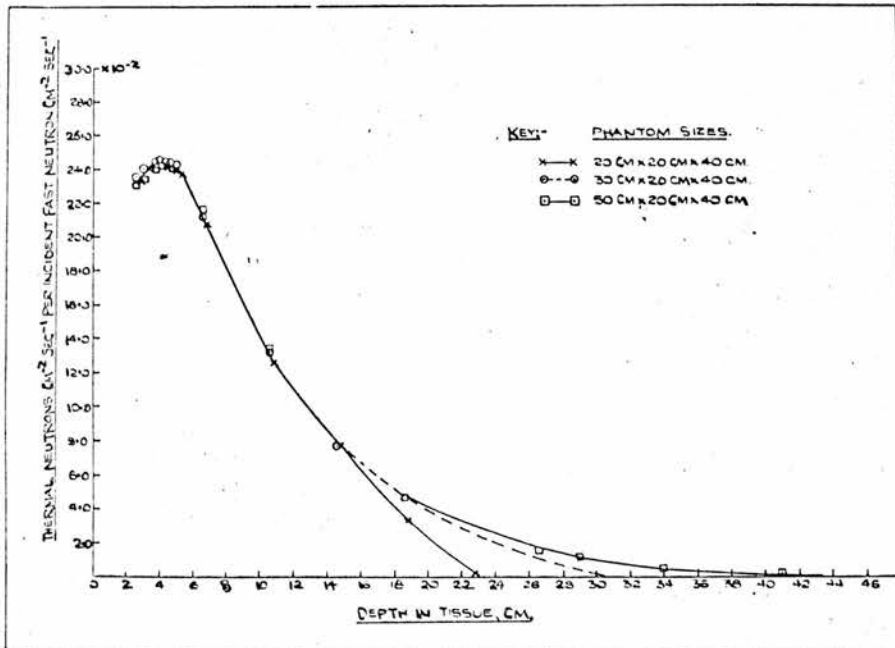


Fig. 6.3 Thermal Neutron Flux from 6 in. Beam Pu-Be Neutrons for Assorted Phantom Sizes Measured Along the Major Axis.

reduction in the position of the peak by 13% which indicates that the average energy of the beam must be decreasing with increasing beam size due to scattering of the fast neutrons in the collimator (Young 1955).

The increase in the thermal neutron flux per incident fast neutron $\text{cm}^{-2} \text{sec}^{-1}$ is due to thermal neutrons produced by the fast neutrons in the more distant parts of the beam diffusing into the detector from the sides. Neglecting absorption losses, the ratio of the thermal neutron flux normalised to one incident fast n $\text{cm}^{-2} \text{sec}^{-1}$ for the various beams to the corresponding value for the 2 in. beam should be equal to the respective ratios of the beam areas to the 2 in. beam area. The observed flux ratios (Table 6.2) are, however, always less than the area ratios which implies that there is a greater loss of neutrons through the phantom as the beam area is increased and that absorption losses cannot be neglected.

§6.4 Effect of Phantom Shape on Thermal Neutron Flux

The investigations were restricted to the 2 in. and 6 in. beams since they provided the maximum and minimum beam sizes available. The polythene phantom sizes used were 20 cm \times 20 cm \times 40 cm, 30 cm \times 20 cm \times 40 cm and 50 cm \times 20 cm \times 40 cm, where 40 cm was the height of the container, 20 cm the minor axis and the major axis was the variable.

The magnitude and position of the normalised thermal neutron fluxes, for both the 2 in. and 6 in. Pu-Be neutron beams traversing the major and minor axis of the phantoms, are summarised in Table 6.3. Fig. 6.2 illustrates the variation in the normalised thermal neutron flux when

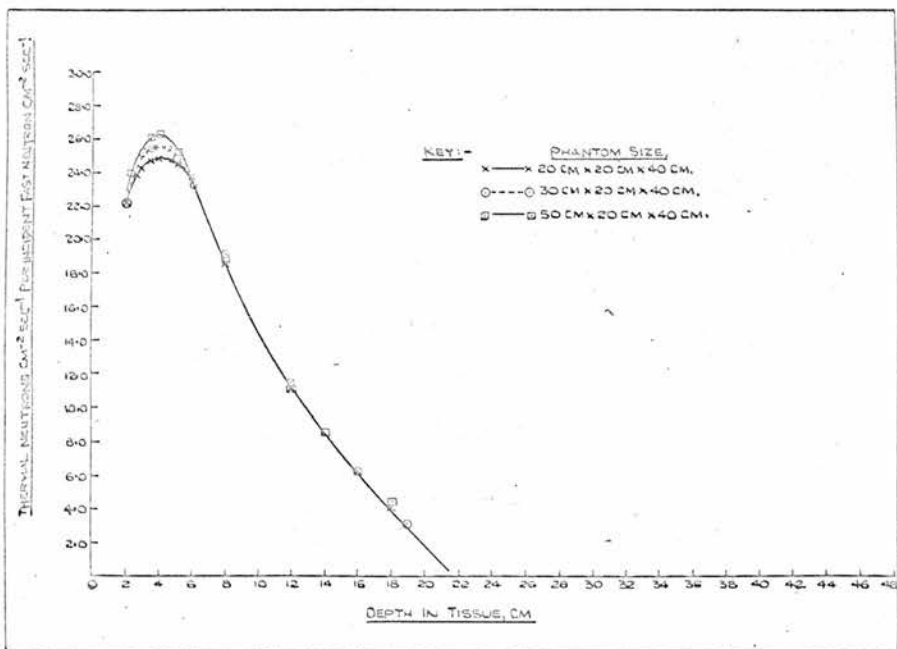


Fig. 6.4 Thermal Neutron Flux from 6 in. Beam Pu-Be Neutrons for Assorted Phantom Sizes Measured Along the Minor Axis.

the 2 in. beam traverses the major axis of the various phantoms, and Fig. 6.3 is the corresponding graph for the 6 in. beam. When the 2 in. beam traverses the minor axis the variation is too small to be measured accurately, however, the 6 in. beam data is shown in Fig. 6.4.

Table 6.3

Irradiation Conditions	Phantom Size cm × cm × cm	Thermal Neutron Flux Peak Position cm.	Thermal Neutrons $\text{cm}^{-2} \text{sec}^{-1}$ per Incident Fast Neutron $\text{cm}^{-2} \text{sec}^{-1}$
6 in. beam along Major axis	20 × 20 × 40	4.0 ± 0.1	24.5 ± 0.2
	30 × 20 × 40	4.0 ± 0.1	24.5 ± 0.2
	50 × 20 × 40	4.0 ± 0.1	24.4 ± 0.2
6 in. beam along Minor axis	20 × 20 × 40	4.0 ± 0.1	24.8 ± 0.2
	30 × 20 × 40	4.0 ± 0.1	25.5 ± 0.2
	50 × 20 × 40	4.0 ± 0.1	26.2 ± 0.2
2 in. beam along Major axis	20 × 20 × 40	4.6 ± 0.1	3.75 ± 0.05
	30 × 20 × 40	4.6 ± 0.1	3.70 ± 0.05
	50 × 20 × 40	4.6 ± 0.1	3.75 ± 0.05
2 in. beam along Minor axis	20 × 20 × 40	4.6 ± 0.1	3.75 ± 0.05
	30 × 20 × 40	4.6 ± 0.1	3.78 ± 0.05
	50 × 20 × 40	4.6 ± 0.1	3.81 ± 0.05

From Table 6.3 and Figs. 6.2 and 6.3 it can be seen that when the neutron beam traverses the major axis of a phantom, the normalised thermal neutron flux maximum value is independent of the phantom both in magnitude and position. The variation in the flux occurs for both

beams after a depth in tissue of 15 cm after which the flux decreases according to how much material is present for backscatter, i.e. the deeper the phantom the longer the flux takes to drop to the same level.

When the beam traverses the minor axis, however, although the peak position remains constant, the absolute value of the normalised flux increases with increasing minor axis, i.e. the flux increases as the phantom width increases. The most noticeable variation is in the 6 in. beam where the maximum flux for the large phantom, 50 cm \times 20 cm \times 40 cm, is 6% higher than for the small 20 cm \times 20 cm \times 40 cm phantom. The deviation from the standard man phantom, 30 cm \times 20 cm \times 40 cm is only \pm 3% for these two extremes. The maximum variation in the peak values for beams traversing the major axis to those traversing the minor axis is less than 10%.

Within the limits of the experiment the position of the peak, 4.6 ± 0.1 cm for the 2 in. beam and 4.0 ± 0.1 cm for the 6 in. beam, is not a function of phantom shape, but depends purely on the beam size and hence average energy of the incident neutrons.

§6.5 Determination of Peak Position and Magnitude

A second experiment was designed to check the effects of scattering on the measured flux. The polythene phantom this time consisted of small polythene tanks, with dimensions 12 in. \times 6 in. \times 6 in. and 6 in. \times 6 in. \times 6 in., filled with tissue equivalent liquid. The thermal neutron flux per incident fast neutron $\text{cm}^{-2} \text{sec}^{-1}$ was measured at depth for both the 2 in. diameter and the 6 in. square beam for three

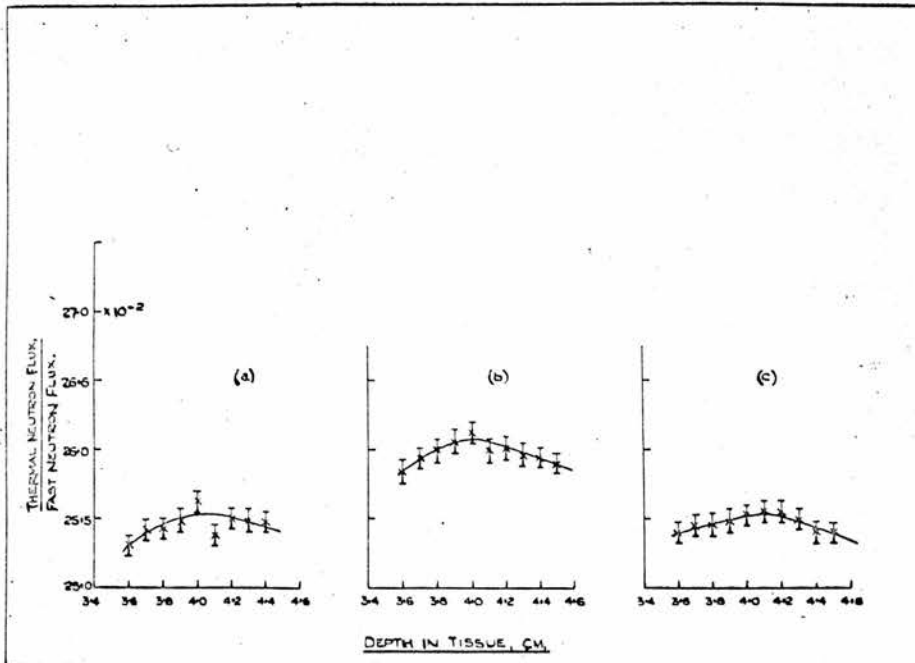


Fig. 6.5 Variation in the Thermal Neutron Peak Magnitude with Phantom Size.

irradiation conditions,

- (a) the larger phantom (12 in. \times 6 in. \times 6 in.) was placed such that the beam was incident on the broad face,
- (b) the surface area of tissue exposed to the beam was effectively doubled by placing a 6 in. \times 6 in. \times 6 in. container on either side of the large container, and
- (c) the depth of the phantom was effectively increased by placing the small containers behind the large container.

This reduced the possibility of error in setting phantoms of various sizes 6 cm from the shield face. The position of the peak was first determined to within 0.5 cm, then the thermal neutron flux was measured at intervals of 0.1 cm. The counting time was sufficient to give a statistical standard deviation error of less than 1% in the total counts.

The data obtained for incident Pu-Be neutrons is summarised in Table 6.4. Fig. 6.5 illustrates the variation in the thermal neutron peak magnitude and position for the 6 in. beam. It can be seen from the graphs for the three conditions that the peak position does not change with phantom size and remains, within the accuracy of the experiment, at 4.0 ± 0.1 cm depth in the tissue. The magnitude of the peak value for conditions (a) and (c) is the same, $(25.52 \pm 0.08) \times 10^{-2}$ thermal neutrons $\text{cm}^{-2} \text{sec}^{-1}$ per incident fast neutron $\text{cm}^{-2} \text{sec}^{-1}$ but increases to $(26.08 \pm 0.08) \times 10^{-2}$ for condition (b). This is to be expected from §6.4 since in (b) the phantom width is increased making

available more material for scatter.

Similar conclusions can be drawn for the 2 in. beam irradiations.

The peak value remains at 4.6 ± 0.1 cm and is $(3.80 \pm 0.04) \times 10^{-2}$ thermal neutrons $\text{cm}^{-2} \text{sec}^{-1}$ per incident fast neutron $\text{cm}^{-2} \text{sec}^{-1}$ for conditions (a) and (c) and $(3.85 \pm 0.04) \times 10^{-2}$ for condition (b).

Table 6.4

Beam Size	Depth in Tissue	Thermal Neutrons $\text{cm}^{-2} \text{sec}^{-1}$ per Incident Fast Neutron $\text{cm}^{-2} \text{sec}^{-1}$		
		a	b	c
2 in	4.2 cm	$3.75 \pm 0.04 \times 10^{-2}$	$3.75 \pm 0.04 \times 10^{-2}$	$3.75 \pm 0.04 \times 10^{-2}$
	4.3	3.78	3.76	3.78
	4.4	3.77	3.80	3.78
	4.5	3.79	3.83	3.79
	4.6	3.80	3.86	3.80
	4.7	3.77	3.82	3.79
	4.8	3.75	3.76	3.77
6 in	3.6	$25.30 \pm 0.08 \times 10^{-2}$	$25.84 \pm 0.08 \times 10^{-2}$	$25.40 \pm 0.08 \times 10^{-2}$
	3.7	25.45	25.95	25.45
	3.8	25.46	26.00	25.46
	3.9	25.48	26.07	25.48
	4.0	25.63	26.13	25.50
	4.1	25.38	25.99	25.55
	4.2	25.50	26.02	25.54
	4.3	25.49	25.96	25.49
	4.4	25.47	25.94	25.40
	4.5	25.47	25.90	25.40

§6.6 Two Group Theory Determination of Thermal Peak

It has been shown that the position of the thermal neutron flux maxima occurs much nearer to the surface of the phantom filled with tissue-equivalent liquid than predicted by the theory of Snyder and

Neufeld (1955). It was suggested that this could be due to the theory neglecting chemical binding effects at thermal energies.

When two group theory is considered an equation can be derived relating the thermal flux maximum position with the thermal neutron diffusion length L_D and the relaxation length L_R . This technique has been described by Block and Shon (1962). The principle is that fast neutrons produce thermal neutrons by interacting with moderating material, in this case tissue-equivalent liquid, and can be represented in two group theory by two equations (Syrett, 1958),

$$D_F \nabla^2 \phi_F - \Sigma_F \phi_F = 0 \quad \dots (6.1)$$

$$D_S \nabla^2 \phi_S - \Sigma_S \phi_S + \Sigma_F \phi_F = 0 \quad \dots (6.2)$$

Equation (6.1) represents the fast group while equation (6.2) is the thermal group. The subscripts F and S refer to the fast and thermal neutrons respectively, Σ_F and Σ_S are macroscopic removal and absorption cross-sections respectively, the D's are diffusion constants, and ϕ_F and ϕ_S are the neutron fluxes. The solution of the equation is simplified if the incident flux is incident at $X = 0$ on a semi-infinite block of moderator. Also at $X = 0$ there is assumed to be no thermal flux. When the boundary conditions are inserted and $L_F^2 = D_F/\Sigma_F$, $L_S^2 = D_S/\Sigma_S$, $L_{FS}^2 = D_S/\Sigma_F$, the solutions to the equations are

$$\phi_F = \phi_{F0} e^{-X/L_F} \quad \dots (6.3)$$

$$\text{and } * \phi_S = \phi_{FO} \left\{ \frac{L_F L_S}{L_{FS}} \right\}^2 \left[\frac{(e^{-X/L_F} - e^{-X/L_S})}{L_F^2 - L_S^2} \right] \dots (6.4)$$

where ϕ_{FO} is the incident fast neutron flux.

The tissue-equivalent phantom is not infinite, but the dimensions (30 cm × 20 cm × 40 cm) are large compared to L_F and L_S . L_F is the relaxation length of the fast neutrons in tissue which is approximately 10 cm for the Pu-Be, D-D and D-T sources and has previously been represented by L_R (§3.6.1) L_S is the diffusion length of the thermal neutrons in tissue (2.68 cm) and was previously written as L_D .

A second assumption inherent in the boundary conditions was that the beam was effectively parallel to the X-axis. This is not true for the 6 in. beam but is approached by the 2 in. beam which is well collimated. Polythene blocks loaded with boron were placed round the sides of the phantom to make certain that the flux entered from one direction only. They did not, however, appear to make any useful contribution to the depth dose measurements and were therefore not used in the determination of the thermal dose.

Since $L_R > L_D$ the second terms of equation (6.4) becomes small compared to the first and the flux ϕ_S falls off exponentially with a relaxation length characteristic of the incident fast neutron flux. The position of the maximum thermal flux is found by differentiating

***Note:** This equation is only true for a pure fast neutron source uncontaminated with thermal neutrons. When thermal neutrons are present a term $\phi_{SO} e^{-X/L_S}$ must be added.

equation (6.4) and setting it equal to zero,

$$X_{\max} = \frac{L_R L_D \ln(L_R/L_D)}{L_R - L_D} \dots\dots (6.5)$$

This equation shows that the thermal peak is a function of the fast neutron energy and also depends on the chemical binding effect of the moderator for thermal neutrons via the diffusion length.

The thermal neutron flux maxima were therefore found for the 2 in. beams of Pu-Be, D-D and D-T neutrons and compared with the maxima position calculated from equation (6.5). In each case the shield face was covered with 0.05 cm thick cadmium to remove any source of thermal neutrons. The data has already been discussed independently for the Pu-Be, and the D-D and D-T neutrons but for convenience it is collected together in Table 6.5.

Table 6.5

Comparison of Theoretical and Experimental Peak Positions

Fast Neutron Source	2 in. Beam Relaxation Length cm	Calculated Thermal Neutron Peak Position cm	Experimental Thermal Neutron Peak Position cm
D-D	9.2	4.7	4.8 ± 0.1
D-T	13.5	5.4	5.5 ± 0.1
Pu-Be	9.8	4.8	4.6 ± 0.1
Thermal Diffusion Length = 2.68 ± 0.05 cm (§7.2)			

The agreement between the experimental and calculated peak positions is excellent and would suggest that this is a better method of calculating the position of the maximum thermal neutron flux, and hence $^{14}\text{N}(n, p) ^{14}\text{C}$ dose, than Snyder's. The agreement is marginally better for the monoenergetic beams which could be expected as the proton recoil dose relation used to calculate the relaxation length is nearer to being a true exponential. It is rather fortuitous that the calculated and experimental values for the Pu-Be source show such good agreement.

Over the range of neutron energies of interest X_{max} is a slowly varying function and by substituting various values for L_S and L_D it can be shown to be more dependent on L_D than L_S . Even comparing the D-D and Pu-Be relaxation lengths and peak positions, the relaxation length has increased by about 7% for an insignificant increase in X_{max} whereas a change in the diffusion length of 7% produces a corresponding change in X_{max} of 7%. Since the diffusion length is known to at least 7% accuracy it is not surprising that the calculated values show such excellent agreement with the experimental data.

§6.7 Theoretical Prediction of the Magnitude of the Peak

It was shown in §6.2 that the magnitude of the peak value of the thermal neutron flux per incident fast neutron $\text{cm}^{-2} \text{sec}^{-1}$, calculated from experimental data for several collimated beams, did not increase in proportion to the beam area due to absorption losses. In this section an attempt has been made to predict the fraction of the thermal neutrons produced that contribute to the absorbed dose measured along

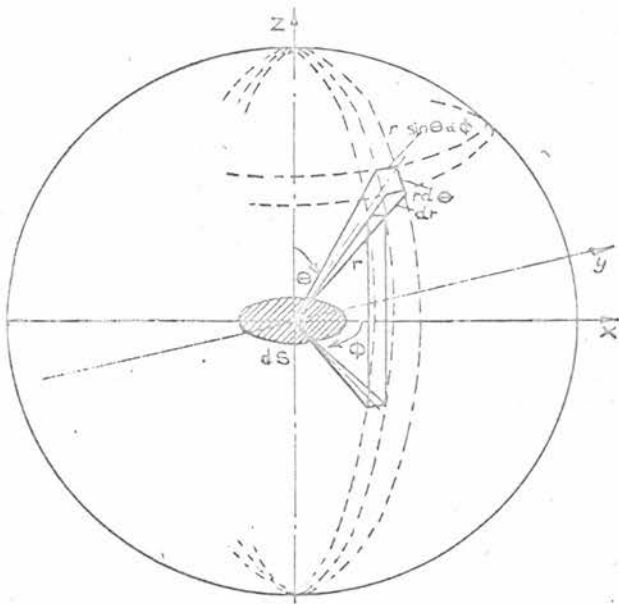


Fig. 6.6 Spherical Co-ordinates.

the axis of the phantom, in particular at the position of the peak, and to compare the fraction with the experimental values. Because the rigorous solution of this problem would be very complicated a simple approach has been assumed.

In the first instance the effect of the various beam sizes can be approximated by assuming that the fast neutrons produce spheres of thermal neutrons (in the tissue-equivalent phantom) with the radii of the spheres corresponding to the radii of the beams. The thermal neutron density is assumed to be constant (N thermal neutron/cc). Since the 6 in. beam is a 'square' collimated beam the effective radius of the sphere has been taken as 8.60 cm which is the radius of a circular collimated beam of the same area as the 6 in. beam.

Consider an element of surface, dS , at the centre of the sphere and a volume element, dV , at distance r cm from dS along a line making an angle θ with the normal to dS (Fig. 6.6). The number of neutrons in dV is $N r^2 \sin \theta d\theta d\phi dr$. Only neutrons emitted in the solid angle subtended at dV by dS will reach dS . This fraction is given by ratio of the area $dS \cos \theta$ to the total surface area of the sphere, $4\pi r^2$. The number of neutrons that leave dV in the direction of dS is therefore

$$N \frac{dS}{4\pi r^2} \cos \theta r^2 \sin \theta d\theta d\phi dr$$

Since the probability of travelling the distance r without impact, and hence absorption, is e^{-r/L_D} , the number which actually strike dS from the whole space above can be obtained by integrating r from 0 to

R, where R is the radius of the collimated beam, θ from 0 to $\pi/2$, and ϕ from 0 to 2π . The total number of thermal neutrons detected is therefore

$$2 \times \frac{NdS}{4\pi} \int_0^R e^{-r/L_D} dr \int_0^{\pi/2} \sin \theta \cos \theta d\theta \int_0^{2\pi} d\phi \dots (6.6)$$

The fraction of the total number of thermal neutrons available which are detected is given by

$$F = \frac{\int_0^R e^{-r/L_D} dr}{\int_0^R dr} \dots (6.7)$$

Since the LiI(Eu) crystal used to measure the thermal neutron flux had a finite size, the neutrons did not have to travel to $r = 0$ to be detected. Equation (6.7) was modified by setting the lower limit of the integral to 0.2 which is the radius of the crystal in cm.

The fraction F calculated for the collimated beams and the ratio of F for any beam size relative to F for the 2 in. beam are given in Table 6.6. A 24 in. wide beam which would effectively give complete irradiation of the 30 cm \times 20 cm \times 40 cm phantom is included for comparison.

Table 6.6

Beam Diameter in.	Sphere Radius cm.	Fraction of Thermal Neutrons Contributing to the Dose F	Ratio of $\frac{F \text{ Beam}}{F \text{ 2 in. Beam}}$	
			Calculated	Experimental
2	2.54	0.575	1.00	1.00
3	3.81	0.486	0.84	0.94
4	5.08	0.412	0.71	0.82
6*	8.60	0.277	0.48	0.58
24	30	0.083	0.14	-

*6 in. beam is a square beam, $\pi r^2 = 36$ sq. in.

The experimental values, taken from column 5 of Table 6.2, were obtained at the position of the peak. The formula derived so far does not stipulate where in the phantom the experimental data should be chosen for comparison with the theory. There is, however, seen to be reasonable agreement between the experimental peak values and the theory calculated on the assumption of constant density of thermal neutrons. The greatest deviation is for the 6 in. beam where the experimental value is 20% higher than predicted by theory. No experimental data was available for the 24 in. beam, but on the assumption that the relative fraction calculated, 0.14, is 20% low, the corresponding

thermal neutron flux per incident fast neutron $\text{cm}^{-2} \text{sec}^{-1}$ is 92×10^{-2} per fast n $\text{cm}^{-2} \text{sec}^{-1}$. This is approximately 4 times the 6 in. beam value and hence the absorbed dose must increase by approximately a factor of 4 which gives a value approaching that predicted by Snyder (1955). While the theory developed to calculate F, and hence F for any beam relative to $F_{2 \text{ in.}}$, will produce a value for F in the limit of infinite beam width ($R \rightarrow \infty$), the ratio of the beam area relative to the 2 in. beam area tends to infinity and it is impossible to predict the thermal neutron flux for an infinitely wide beam. Since Snyder's theory is based on an infinitely wide beam incident on an infinitely wide phantom it is reasonable to assume that the 24 in. wide beam incident on a 30 cm wide phantom will provide a good approximation to the theoretical prediction of Snyder.

Equation (6.6) can be modified to take account of the variation in the thermal neutron density and also to specify the position in the phantom at which the theory should be compared to the experimental data. The centre of the spheres shall now be taken at the position of the peaks. The sphere can be considered as two hemispheres divided by the YZ plane where the X axis is the depth in tissue. Each hemisphere has a neutron density approximated to a straight line equation of the form $N = kX + N_0$ where N is the neutron density at distance X along the X axis measured from the centre of the sphere ($X = 0$), k is the gradient, and N_0 is the neutron density at the centre. When N is substituted in equations (6.6) X is expressed as $r \cos \theta$. Since the thermal neutron

density is now enhanced near the detector a larger fraction of neutrons can be expected to reach the detector. The fraction F can now be calculated from the relation

$$F = \frac{\int_{0.2}^R \int_0^{\pi/2} e^{-r/L_D} (k r \cos \theta + N_0) \cos \theta \sin \theta d \theta dr}{\int_{0.2}^R \int_0^{\pi/2} (k r \cos \theta + N_0) \cos \theta \sin \theta d \theta dr} \dots (6.8)$$

for both hemispheres and weighted to give F for the total sphere. The values of F obtained for the collimated beams are given in Table 6.7 and also the value of F for any beam relative to F for the 2 in. beam.

Table 6.7

Values of F for Non-Uniform Flux Density

Beam Diameter in.	Sphere Radius cm.	F for X - negative	F for X - positive	Mean	Ratio of $\frac{F \text{ Beam}}{F \text{ 2 in. Beam}}$	
					Calculated	Experimental
2	2.54	0.604	0.574	0.589	1.00	1.00
3	3.81	0.530	0.510	0.520	0.89	0.94
4	5.08	0.464	0.444	0.454	0.77	0.82
6*	8.60	0.336	0.312	0.324	0.55	0.58

*6 in. beam is a square beam.

The value of F calculated for the thermal neutron flux density to the left of the peak is represented in the table as $F_{X - \text{negative}}$, and

similarly for F to the right of the peak it is F_X - positive. Since the flux density gradient is steeper to the left of the peak the fraction F is correspondingly larger.

It can be seen from the table that by modifying equation (6.6) to provide a more realistic simulation of the actual experimental condition the experimental data can be predicted to an accuracy of 6%. When the errors involved in obtaining the experimental data are considered along with the assumption made in the theoretical approach, surprisingly good agreement is obtained.

Several conclusions can now be made from the two theoretical approaches. The more refined technique provides evidence in support of the experimental data and explains why the thermal neutron flux values do not increase in proportion to the beam area. A knowledge of the thermal neutron density is required, however, before this can be applied to the collimated beam in question. The experimental peak values for various beam sizes can, however, be predicted to a fair degree of accuracy using the simple technique where the density is assumed to be uniform. The thermal neutron flux per incident fast neutron $\text{cm}^{-2} \text{sec}^{-1}$ for the 2 in. beam is all that is required to be known to calculate the corresponding values for the other beams. Since the more refined method supports the experimental data, it must be assumed that this data is accurate and that the theoretical predictions by the simple method are low by as much as 20%. If these theoretical values are increased by 10% then the predicted experimental values should be correct to

± 10% for all beam sizes.

§6.8 Conclusions

The position of the thermal neutron flux maximum per incident fast neutron $\text{cm}^{-2} \text{sec}^{-1}$ can be calculated from equation (6.5) provided the incident beam is well collimated. Since the position of the peak is a function of the incident neutron energy, it varies for the three neutron sources considered. Also, for each source, it varies with the beam size due to neutrons which have been scattered in the collimator degrading the emergent neutron energy spectrum. The position of the peak does not depend on the shape of the phantom. Equation (6.5) can only be applied when the phantom dimensions are greater than the relaxation length.

The magnitude of the maximum flux is always larger for a beam traversing the minor axis, than it is for a major axis of the same phantom due to the extra mass of moderator available for scatter from the sides of the phantom. The maximum increase of a minor axis over a major axis is < 8% for the phantom sizes used.

When the beams traverse the major axis the magnitude of the maximum flux remains constant, but for the minor axis it increases slightly with increase in phantom size. The maximum observed increase was < 6%.

It was shown in §6.7 that the thermal neutron flux, and hence thermal neutron dose, at the peak position can be predicted to 10% accuracy provided the 2 in. beam dose measurements are available. The dose predicted by Snyder provides an upper limit to the dose received

but the maximum dose is nearer to the surface of the body than predicted by Snyder. Finally if the results were applied to the irradiation of people having different physical dimensions it is sufficient to calculate the dose for the standard man using the 30 cm × 20 cm × 40 cm phantom and the appropriate beam size. This provides a measure of the dose received for a person of any shape to within ± 5%.

CHAPTER SEVEN

FUNDAMENTAL PARAMETERS OF TISSUE-EQUIVALENT LIQUID
REQUIRED IN CALCULATIONS

§7.1 Introduction

The thermal neutron diffusion length L , and the transport mean free path λ_{tr} , have been mentioned in connection with various calculations in the energy deposition studies. For example, a knowledge of the diffusion length and transport mean free path was required to calculate the flux depression factor. Since neither of these quantities were recorded in the literature, for the tissue-equivalent liquid used, they were determined by experiment and compared with theory.

§7.2 Thermal Diffusion Length, L , and Transport MeanFree Path, λ_{tr} , for Tissue

The simple diffusion equation for the steady state condition in a non-multiplying medium is

$$\nabla^2 \phi - \frac{\Sigma \alpha}{D} \phi = 0$$

where D is the diffusion coefficient in cm, $\Sigma \alpha$ is the macroscopic absorption cross-section in cm^{-1} and ϕ is the thermal neutron flux in $\text{n cm}^{-2} \text{ sec}^{-1}$.

The quantity $\left(\frac{D}{\Sigma \alpha}\right)^{\frac{1}{2}}$ is the diffusion length. D can be replaced by the transport mean free path λ_{tr} since

$$D = \frac{\lambda_{tr}}{3} = \frac{1}{3 \Sigma_s (1 - \overline{\cos \phi})}$$

where Σ_s is the macroscopic scattering cross-section and $\overline{\cos \phi}$ is the average cosine in the laboratory system of the scattering angle.

These definitions assume that the neutrons are monoenergetic, and that in the scattering process, the atoms behave as if they are free. Experimentally, however, there is a spectrum of neutron energies which can be represented by a Maxwellian distribution. The quantities λ_{tr} and Σ_a must be averaged over this distribution, and if necessary, be corrected for the binding of the atoms in the molecule.

The diffusion length, L , can then be calculated from the equation

$$L^2 = \frac{\bar{\lambda}_{tr}}{3 \bar{\Sigma}_a}$$

where the bar indicates the averaging procedure is applied, and Σ_a is very much less than Σ_{tr} .

$$\bar{\Sigma}_a = \frac{\int_0^{\infty} \Sigma_a(E) \phi(E) dE}{\int_0^{\infty} \phi(E) dE} \quad \dots (7.1)$$

$$\bar{\lambda}_{tr} = \frac{\int_0^{\infty} \lambda_{tr}(E) \phi(E) dE}{\int_0^{\infty} \phi(E) dE} = \frac{\int_0^{\infty} \frac{1}{\Sigma_{tr}(E)} \phi(E) dE}{\int_0^{\infty} \phi(E) dE} \quad \dots (7.2)$$

where $\phi(E)$ is the value of the temperature dependent Maxwellian flux distribution at energy E , and $\Sigma_a(E)$ and $\Sigma_{tr}(E)$ are the macroscopic absorption and transport cross-sections respectively at the same energy.

Since the absorption cross-section is proportional to the reciprocal of the velocity it can easily be shown that

$$\bar{\Sigma}\alpha = \frac{\sqrt{\pi}}{2} (\Sigma\alpha)_{v_0} \sqrt{\frac{T_b}{T_m}} \frac{\rho(T_m)}{\rho(T_b)} \dots (7.3)$$

where $(\Sigma\alpha)_{v_0}$ and T_0 are the values of the macroscopic absorption cross-section and temperature ($E = kT$) at the neutron velocity of 2,200 m/s i.e. $T_0 = 293.6^\circ\text{K}$. T_m is the temperature of the material and $\rho(T_m)$, $\rho(T_0)$ are the densities at temperatures T_m and T_0 respectively.

The macroscopic absorption cross-section $(\Sigma\alpha)_{v_0}$ was calculated from the equation

$$(\Sigma\alpha)_{v_0} = \frac{\rho(T_0) N_A}{M} \cdot \sum_i \nu_i \sigma_i$$

where M is the molecular weight of the material, N_A is Avogadro's number and ν_i is the number of atoms of type i with microscopic absorption cross-section σ_i . Finally from equation (7.3), $\bar{\Sigma}\alpha$ was found to be 0.0194 cm^{-1} for water and 0.0228 cm^{-1} for tissue-equivalent liquid.

The mean value of the transport mean free path does not resolve to such a simple expression since the corresponding cross-section is not proportion to $(1/E)^{1/2}$. Instead λ_{tr} must be determined from experimental data at each energy and averaged over a Maxwellian distribution according to equation (7.2).

The transport mean free path and hence diffusion length for thermal neutrons in hydrogenous materials cannot be calculated in the simple manner used for single elements in the unbound state. Chemical binding

of the hydrogen atoms in the molecule affects the proton cross-section at thermal energies (Bethe 1937). The proton can be considered completely bound in the limit of zero neutron energy and free for energies above a few electron volts. For low energies the neutron wavelength is much larger than the molecular dimensions and therefore the protons are tightly bound to the oxygen atom and instead of recoiling by themselves, the whole molecule recoils.

Various authors have produced data on the effective hydrogen scattering cross-sections for thermal neutrons in hydrocarbons and water (Esch 1963, Melkonian 1949). Radkowsky (1950) proposed a model with which to compare the experimental neutron scattering cross-sections for water. The transport cross-section was defined as

$$\sigma_{tr}(E) = \sigma_s(E) (1 - \bar{\mu})$$

where $\bar{\mu} = \overline{\cos \phi}$ is the first Legendre moment of the differential cross-section and is equal to $2/3A$ where A is the mass of the scatterer.

Radkowsky suggested that the effects of molecular binding at the lower energies could be described by an effective mass $A(E)$. The quantum mechanical treatment of the scattering problem shows that for the bound atom, the scattering cross-section varies directly with the square of the reduced mass ratio.

$$(\sigma_s)_{free} = (\sigma_s(E))_{bound} \left[\frac{A(E)}{A(E) + 1} \right]^2 \left[\frac{A}{A + 1} \right]^2 \dots (7.4)$$

where A is the mass of the nucleus bound in the molecule.

Implicit in Radkowsky's method is that the scattering remains

isotropic in the centre of mass system.

The total transport mean free path of the molecule can now be calculated from a modified version of Radkowsky's prescription, via the transport cross-section, providing the scattering cross-section of the molecule is known. To a first approximation, the scattering cross-sections of all elements other than hydrogen can be assumed constant at their 'free atom' value. For hydrogen equation (7.4) reduces to

$$A(E) = \sqrt{\frac{1}{\frac{82.4}{\sigma_s(E)} - 1}}$$

since $(\sigma_s)_{\text{bound}}$ for hydrogen is 20.6 barns. The transport cross-section for the proton is

$$\sigma_{\text{tr}}(E) = \sigma_s(E) \left[1 - \frac{2}{3A(E)} \cdot R(E) \right]$$

where $R(E)$ is a weighting factor equal to the ratio of the macroscopic hydrogen total cross-section to the macroscopic total cross-section of the molecule, at energy E , and $\sigma_s(E)$ is the scattering cross-section of the proton.

The transport mean free path of the other elements present is then found from the standard relation

$$\sigma_{\text{tr}} = \sigma_s \left[1 - \frac{2}{3A} \right]$$

and the total transport cross-section is the sum of the individual cross-section. The method described was used to calculate the transport mean

free path for water, H_2O , and for tissue-equivalent liquid, $C_6 H_4 O O_{18} N$. The tissue molecules were assumed to have this formula since there was data available for the effective scattering cross-section of hydrogen in soft tissue (Schermer and Brownell 1961), but not for all the individual molecules which had been mixed to form the liquid. The total cross-sections used for carbon, nitrogen and oxygen were 4.6, 10.0 and 3.8 barns respectively (Hughes and Schwartz, 1958). The total cross-section of water was obtained from Hughes and Schwartz, and for tissue from Schermer's data.

The average value of the mean free path in each case was found by averaging the data over the Maxwellian distribution at the temperature $293.6^\circ K$ corresponding to a velocity of 2200 m/sec. The transport mean free path obtained for water, 0.452 cm, agreed with the calculated value of Esch (1963) who used a similar technique. Since Esch obtained excellent agreement between his calculated transport mean free paths for paraffin, polythene and water, and the corresponding experimental data, it seems reasonable to expect that the calculated transport mean free path for tissue-equivalent liquid of 0.466 cm should also show good agreement with experimental data. Unfortunately, due to poor experimental statistics, it was not possible to measure λ_{tr} for tissue.

The diffusion length was then calculated from the relation

$$L^2 = \frac{\bar{\lambda}_{tr}}{3 \sum \alpha}, \text{ and found to be } 2.78 \text{ cm for water and } 2.61 \text{ cm for the}$$

tissue-equivalent liquid, at $293.6^\circ K$.

[Note - Throughout Esch's report he makes a fundamental error in assuming that

$$\overline{\sigma}_{tr} = \frac{1}{N \overline{\lambda}_{tr}} \quad \dots (7.5)$$

where $\overline{\sigma}_{tr}$ is meant to represent the average Maxwellian transport cross-section. The diffusion length is defined in terms of the transport mean free path and not the cross-section which enters only indirectly by the relation

$$\lambda_{tr} = \frac{1}{N \overline{\sigma}_{tr}} \quad \text{where } N = \text{no. of molecules/cc.}$$

Hence when considering a Maxwellian distribution it is necessary to average the mean free path and not the cross-section and therefore

$$\overline{\lambda}_{tr} = \overline{\frac{1}{N \sigma_{tr}}} = \frac{1}{N} \cdot \overline{\frac{1}{\sigma_{tr}}} \neq \frac{1}{N \overline{\sigma}_{tr}} \quad \text{in general, from which it}$$

follows that equation (7.5) is incorrect.

The error is not immediately obvious in Esch's paper because it is applied to both the theoretical and experimental data. The calculations would be valid if his $\overline{\sigma}_{tr}$ was replaced by $\overline{\sigma_{tr}}$ or $(\sigma_{tr})_{\text{effective}}$ to indicate that the cross-section value quoted is not the Maxwellian average.

This does not detract, however, from the comparison of the present data with Esch's since he has in fact calculated $\overline{\lambda}_{tr}$ and it is only where the data is converted to cross-sections that the error occurs.]

The diffusion length was determined by experiment for water and the tissue-equivalent liquid. The value obtained for water acting as

a check on the validity of the experiment. Production of the thermal neutron flux has already been described in §2.4. The magnitude of the flux was found to be too low to obtain good statistics in the determination of the transport mean free path which was attempted by measuring the extrapolation length d and using the relation $d = 0.7104 \lambda_{tr}$ (Valente 1963). Since the absorption cross-sections are well known, however, λ_{tr} was obtained from the diffusion length.

The thermal flux was measured at depth in a 30 cm cubic polythene container, with 0.6 cm thick walls, filled with the appropriate moderator. Measurements of the thermal flux were made using a 4 mm diameter by 4 mm thick $\text{LiI}(\text{Eu})$ crystal along the axis of the beam after a depth of several slowing down lengths.

Since the beam was still a mixture of thermal neutrons and fast neutrons readings were taken at each position for,

- (a) the face of the shield completely covered with cadmium 0.05 cm thick, and
- (b) the shield completely covered except for the 6 in. square beam hole.

The difference between the two count rates gave the number of thermal neutrons at depth in tissue. The count rates were normalised in each case to 1 c/min on the standard. Throughout the experiment the polythene container was surrounded with 0.05 cm thick cadmium foil, except the face exposed to the beam, to remove any thermal neutrons produced by scattered fast neutrons.

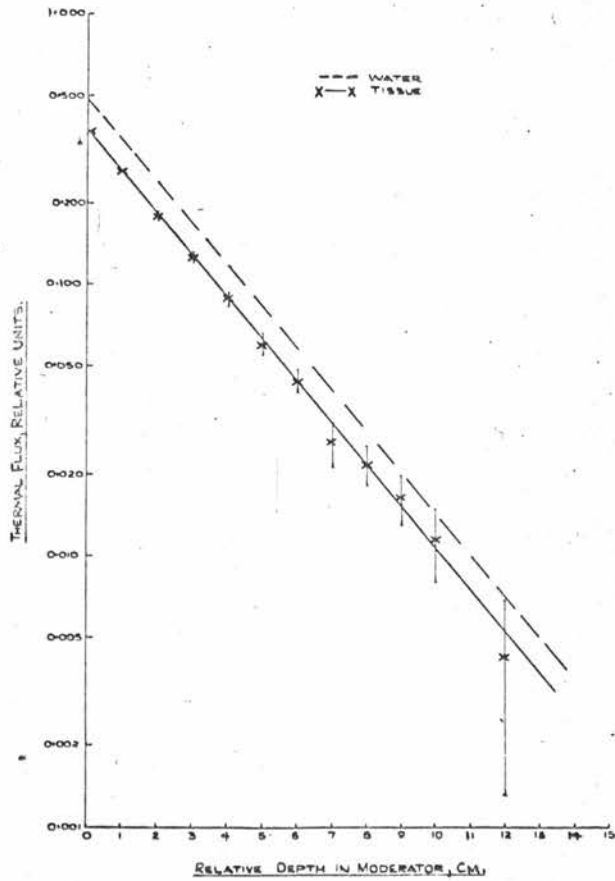


Fig. 7.1 Thermal Neutron Diffusion Length.

A graph of the log of the relative count rate is plotted against relative depth in the moderator in Fig. 7.1.

The standard fundamental solution of the diffusion equation $\nabla^2 \phi - \frac{\phi}{L^2} = 0$, i.e. neglecting higher harmonics, for a plane source of neutrons emitted at $Z = 0$ across a block of the material of dimensions 'a' in the x direction, 'b' in the y direction and 'h' in the z direction is

$$\phi(x,y,z) = \frac{2S}{abD} \cdot L_{11} \cos \frac{\pi x}{a} \cos \frac{\pi y}{b} e^{-z/L_{11}}$$

where S is the planar neutron source strength, D the diffusion coefficient and L_{11} is the relaxation length, (Glasstone and Sesonske 1955). The correlation between L and L_{11} is given by

$$\frac{1}{L_{11}^2} = \frac{1}{L^2} + \frac{\pi^2}{a^2} + \frac{\pi^2}{b^2} \quad \dots (7.6)$$

where L_{11} is the slope of the appropriate straight line in Fig. 7.1. Some indication of the size of container required can be seen from equation 7.6 putting $\pi^2 \left(\frac{1}{a^2} + \frac{1}{b^2} \right)$ equal to C^2 . Assuming the error in C is negligible,

$$\frac{\Delta L}{L} = \frac{\Delta L_{11}}{L_{11}} (1 + C^2 L^2) \text{ is the relative error in L.}$$

When $a = b = 30$ cm and L is assumed to be 3 cm., the error in L is only 1.2 times the error in L_{11} .

The least squares method was used to determine the best straight line and hence the slope of the line for both water and tissue. The errors in the data for water and tissue were very similar. Since water was used as a reference material, the errors have been plotted for

tissue-equivalent liquid only, to avoid confusion.

The diffusion lengths obtained were corrected to a moderator temperature of 293.6°K and gave the values 2.80 ± 0.06 cm for water and 2.68 ± 0.05 cm for tissue. The corresponding transport mean free paths were 0.46 ± 0.02 cm and 0.49 ± 0.02 cm. The values for water agree favourably with the data of Jarvis (1964) who has reviewed the diffusion parameters for thermal neutrons in water thus confirming the reliability of the method used in this experiment.

Table 7.1 gives a comparison of the theoretical and experimental diffusion lengths for tissue-equivalent liquid and water.

Table 7.1

Material \ Diffusion Length	Experimental cm	Theoretical cm
Water	$2.80 \pm .06$	2.78
Tissue-Equivalent Liquid	$2.68 \pm .05$	2.61(2.73)*

*It is difficult to estimate the error in the theoretical value of L. In particular in the calculation of L for tissue, the data of Schermer for the total cross-section of muscle tissue was used, where on the same graph the total cross-section for water was in error due to being displaced about the vertical axis. It was assumed that the data for tissue

was correct, however, if it too was displaced the the average Maxwellian transport cross-section calculated should be larger by approximately 10% which would make the diffusion length 2.73 cm instead of 2.61 cm. Since this was the only available reference, and the latter choice would move the theoretical value of the diffusion length towards the experimental value, the only conclusion that can be reached without bias is that the theoretical value for the diffusion length using a modified Radkowsky prescription will predict the diffusion length, certainly to well within 10%, and probably to better than 5%.

The diffusion length for tissue-equivalent liquid was therefore accepted as $2.68 \pm .05$ cm with a corresponding transport mean free path of $0.49 \pm .02$ cm.

§7.3 Flux Depression Caused by a LiI(Eu) Crystal

The thermal neutron fluxes measured using the LiI crystals required to be corrected for flux perturbations caused by the presence of the crystals. The crystal may act as a neutron sink absorbing neutrons which would normally have traversed the region occupied by the crystal more than once. This is known as 'flux depression' which depends on the total mean free path λ_t and the diffusion length L in the medium surrounding the detector, the thickness t and the radius R of the detector, and the macroscopic absorption cross-section Σ_a in the detector.

A second perturbation to the flux is the 'self-shielding' effect whereby the flux at the centre of the detector may be less than that

surrounding it due to the attenuation of neutrons while passing through the detector. The observed flux ϕ must therefore be increased to yield the true flux density ϕ_0 in the absence of the detector.

Several theories have been developed to provide a measure of these perturbation effects. Bothe (1943) calculated this effect on the basis of first order diffusion theory for a detector in the form of a small sphere, which he then modified to approximate to a thin circular disc detector. It was later found by Tittle (1951) that the theoretical treatment of Bothe for small spheres gave better agreement with experimental data than the corrected version provided that the scattering mean free path was replaced by the transport mean free path. Meanwhile Skyrme (1943) had also developed an alternative formula by an approximate solution of one speed transport theory provided $R \gg t$ and $\Sigma\alpha R \geq 1$. Ritchie and Eldridge (1960) compared the modified Bothe formula with the Skyrme formula, and used a more accurate transport theory for an infinite foil ($R \rightarrow \infty$) in an isotropically scattering medium. They proposed that the relationship between the observed flux ϕ after inserting the detector and the true average flux ϕ_0 for a finite sized foil should be

$$\frac{\phi}{\phi_0} = \frac{1/\tau \left[\frac{1}{2} - E_3(\tau) \right]}{1 + \left[\frac{1}{2} - E_3(\tau) \right] \left[\frac{3}{2} \cdot \frac{L}{\lambda} S\left(\frac{2R}{L}\right) - K\left(\frac{2R}{\lambda}, \gamma\right) \right]} \quad \dots (7.7)$$

The functions $S(2R/L)$ and $K(2R/\lambda, \gamma)$ are presented graphically in

N.B.S. Handbook 85 (1964). The quantity τ is defined to be $t \Sigma\alpha$ and

$E_3(\tau)$ is a third order exponential integral defined by

$E_n(x) = \int_1^\infty \frac{e^{-xu}}{u^n} du$ where $n = 3$ and can be obtained from tables produced by Trubey (1959). The cross-sections used must be averaged over the appropriate Maxwellian distribution for the flux. The parameter γ is the ratio of macroscopic scattering cross-section to the macroscopic total cross-section i.e. $\gamma = \frac{\Sigma_s}{\Sigma_t}$. Helm (1963), however, suggested that this should be modified for anisotropic scattering in the laboratory system to $\gamma = \frac{\Sigma_{tr}}{\Sigma_t}$ where Σ_{tr} is the macroscopic transport cross-section.

Since there was no literature available on the flux perturbations caused by LiI crystals it was decided to measure the flux depression and compare it with theory. The formula of Ritchie and Eldridge, modified for anisotropic scattering, was used since it was applicable over the widest range of crystal dimensions.

The experimentally determined values of the diffusion length and transport mean free path were used in equation (7.7). The numerator is the self-shielding factor and the remainder of the equation accounts for the flux depression. When τ is > 3.5 the quantity $\frac{1}{2} - E_3(\tau)$ is a constant 0.5. The macroscopic absorption cross-section of LiI crystals is 14.69 cm^{-1} when averaged over the Maxwellian distribution, therefore $\frac{1}{2} - E_3(\tau)$ will be constant for all crystals where thickness is $> 0.25 \text{ cm}$. and hence the flux depression would be dependent only on the radius. Since the self-shielding factor is solely a function of thickness this provides a method of discriminating the two effects. Different sized crystals (greater than 0.25 cm thick) were therefore used

to obtain numerous count rates at various depths in the phantom. It is deduced that no correction is required for self-shielding when using a LiI crystal provided only the surface area is considered effective for calculating the flux.

The experimental flux depression factor for a 2.54 cm diameter by 0.20 cm thick crystal was found to be 1.50 i.e. $\phi_0 = 1.50 \phi$. Theoretically ϕ_0 was 1.98ϕ for $L = 2.68$ cm and $\lambda_{tr} = 0.437$ cm. Owing to the uncertainties in the parameters involved this is in reasonable agreement with the experimental result. The flux measurements using the small crystal were therefore corrected by the appropriate theoretical factor 1.10.

CHAPTER EIGHT

CONCLUSIONS AND RECOMMENDATIONS FOR THE FUTURE

A complete evaluation of the energy deposited at depth in a tissue-equivalent phantom by three basic reactions due to irradiation with collimated beams of fast neutrons has been discussed in detail in the previous chapters. Ideally for the purposes of radiation protection and radiobiology it should be possible to express the physical data pertaining to tissue damage as

- (a) the absorbed dose in rads per incident fast neutron per cm^2 ,
 - (b) the distribution of the absorbed dose with LET, and associated with this the determination of an effective quality factor,
 - and (c) the absorbed dose in rems per incident fast neutron per cm^2 .
- This was successfully carried out in this report using only the two detectors described in Chapter 3.

The usefulness of the theoretical predictions of Snyder and Neufeld concerning the components of absorbed dose at depth in tissue has been confirmed for radiation protection purposes where the variation between theory and experiment of a factor of 2 is not critical. For more accurate radiobiological work, however, Snyder underestimates the proton recoil dose at the back of the phantom by an appreciable amount. It was also shown that although Snyder predicted the upper limit to the thermal neutron dose, the depth in tissue at which it occurred was in error. It is concluded that the thermal neutron dose should in fact be determined by the method described in Chapter 6 where two group theory

was used successfully to predict the doses measured in this report.

Excellent agreement was found between the proton recoil dose quality factors measured using the plastic phosphor and the values calculated by Snyder, reported in N.B.S. 63. It was found, however, that when the proton recoil dose due to 2.5 MeV neutrons was expressed as a function of LET, the phosphor curves did not agree with Snyder's histograms. The latter were greatly in error, possibly due to inaccuracies in the computer programme which is still in the early stages of development. Since the phosphor curves showed excellent agreement with the theoretical curves of Boag, it is concluded that this technique is satisfactory for determining the absorbed dose as a function of LET at depth in tissue.

A method of calculating the quality factor for the total dose due to 14 MeV neutrons was suggested in §4.4.3 which gave a QF of 8.5. It should be noted that this is less than the QF value of 10 currently accepted for neutrons of unknown energy. This, therefore, lends support to the theory that the maximum quality factor for neutrons can be taken to be 10. Other quantities which have also been measured for the first time include such parameters as the thermal neutron diffusion length in tissue, the flux depression due to LiI(Eu) crystals, and the proton recoil dose distribution with LET as a function of depth in tissue.

It is therefore concluded that the experimental techniques and theories suggested in this report should be adopted in neutron depth dose measurements. In §3.5 an indication was given of the magnitude of the distortion in the recoil proton spectrum due to wall and end effects.

It is intended to study this in more detail and to determine the optimum phosphor size for the depth dose measurements. The dose due to heavy recoils has not been considered in this report, however, according to Randolph 30% of the total dose from 14 MeV neutrons is due to elastic and inelastic scattering from the carbon, oxygen and nitrogen nuclei. Due to the widespread use of neutron generators for the production of 14 MeV neutrons it is felt that more research into the association^{ed} neutron dose should be carried out by several independent research institutes. In particular an attempt should be made to determine the heavy recoil dose. The large neutron fluxes available suggest that a combination of the techniques used in this report and tissue-equivalent plastic proportional counters could be used to separate the heavy recoil component from the total dose. Finally, it would also be of interest to measure the absorbed dose in air and in bone, and to compare the experimental perturbation on the dose in tissue due to the presence of air cavities and bone with the dose inferred from the experimental data obtained for air, bone and tissue.

REFERENCES

- Abson, W., Salmon, P. G., and Pyrah, S., 1957 A.E.R.E. EL/R/2406.
- Aceto, H., and Churchill, B. W., 1963 UCRL, 10267.
- Aebersold, P. C., and Lawrence, J. H., 1942, Am. Rev. Physical., 4, 25.
- Akagi, H., and Lehman, R. L., 1963, Health Physics, 9, 207.
- Anderson, M. E. and Bond Jr., W. H., 1963, Nuclear Physics, 43, 330.
- Anderson, I. Ö., and Braum, J., 1964, AE-132.
- Attix, F. H., 1965, The Meaning of First Collision Dose, Paper 113,
The Tenth Annual Meeting of the Health Physics Society.
- Barr, T. A., and Hurst, G. S., 1954, Nucleonics, 12, 33.
- Basson, J. K., and Dennis, J. A., 1962, A.E.R.E.-M 966.
- Bateman, J. L., Rossi, H. H., Bond, V. P., and Gilmartin, J., 1961,
Rad. Res., 15, 694.
- Benveniste, J., Zenger, J., 1954, UCRL-4266.
- Benveniste, J., Mitchell, A. C., Schrader, C. D., Zenger, J. H., 1959,
UCRL-5619.
- Bethe, H. A., 1937, Rev. Mod. Phys., 9, 119.
- Biram, M. B., 1949, A.E.R.E. Report No. T/R 443.
- Biram, M. B., 1962, A.E.R.E. Report No. T/R 1062.
- Birks, J. B., 1951, Proc. Phys. Soc., A 164, 10.
- Block, S., and Shon, F. J., 1962, Health Physics, 8, 533.
- Blosser, T. V., and Freestone, R. M., 1963, ORNL-3499 (Vol. 2), 85.
- Boag, J. W., 1954, Radiation Research, 1, 323.
- Bothe, W., 1943, Zeits. Angew, Phys., 120, 437.
- Bragg, W. H., 1912, Studies in Radioactivity, 94.

- Bramblett, R. I., Ewing, R. I., and Bonner, T. W., 1960, Nucl. Inst. and Methods, 2, 1.
- Bretscher, E., and French, A. P., 1944, British Atomic Energy Project Report BR-517.
- Brinkman, G. A., 1961, Ph.D. Thesis, Univ. of Amsterdam, October.
- Broek, H. W., and Anderson, C. E., 1960, Rev. Sci. Inst., 31, 1063.
- Bush, F., 1949, Brit. J. Radiol., 22, 102.
- Campbell, R. C., Korsmeyer, J. D., and Ralph, D. C., 1954, Phys. Rev., 94, 791.
- Capron, P. C., Faes, M., and Tavernier, G. C., 1949, Nature, 162, 129.
- Cheka, J. S., 1953, Phys. Rev., 90, 353.
- Chou, C. N., 1952, Phys. Rev., 87, 376 and 904.
- Conger, A. D., Randolph, M. L., Sheppard, C. W., and Luippold, H. J., 1958, Radiation Research, 9, 525.
- Cook, J. E., 1958, A.E.R.E. HP/R2744.
- Cowan, F. P., Phillips, L. F., and King, R. J., 1964, Health Physics, 10, 33.
- Dainty, J., 1950, CRM-482.
- Dennis, J. A., and Loosemore, W. R., 1957, A.E.R.E. EL/R2149.
- De Pangher, J., and Roesch, W. C., 1955, Phys. Rev., 100, 1793.
- Esch, L. J., 1963, Nucl. Sci. and Eng. 16, 196.
- Evans, H. C., and Bellamy, E. H., 1959, Proc. Phys. Soc., 74, 485.
- Fano, U., 1963, Ann. Rev. Nucl. Sci., 13, 1.
- Field, S. B., 1964, Inst. of Physics Conf. on Neutron Dosimetry for Radiological Purposes, 24th January.

- Field, S. B., and Parnell, C. J., 1965, Brit. J. Radiol, 38, 618.
- Fowler, J. L., and Brolley, J. E., 1956, Rev. Mod. Phys., 28, 103.
- Gabrysh, A. F., Eyring, H., Wadsworth, M. E., Baker, G. S., and Ree, T.,
1960, Jour. of App. Phys., 31, 1785.
- Geiger, K. W., and Hargrove, C. K., 1964, Nuclear Physics, 53, 204.
- Gettner, M., and Selove, W., 1960, Rev. Sci. Inst., 31, 450.
- Glass, F. M., and Hurst, G. S., 1952, Rev. Sci. Inst., 23, 67.
- Glasstone, S., and Sesonske, A., 1955, Nuclear Reactor Engineering.
- Glos, M. B., 1965, Nucleonics, 23, 66.
- Gooding, T. J. and Pugh, H. G., 1960, Nucl. Inst. Methods, 7, 189.
- Gray, L. H., 1928, Proc. Roy. Soc., A 122, 648.
- Gray, L. H., Mottram, J. C., and Read, J., 1940, Brit. J. Radiol., 13,
371.
- Gray, L. H., and Read, J., 1939, Nature, 144, 439.
- Hall, R. S., and Poole, D. H., 1965, C.E.G.B. RD/B/N 265.
- Hankins, D. E., 1961, IDO-16655.
- Hanson, A. O., and McKibben, J. L., 1947, Phys. Rev., 72, 673.
- Heertje, I., Van Westen, N. P., and Aten Jr., A. H. W., 1964, Physica,
30, 1846.
- Helm, F. J., 1963, Nucl. Sci. and Eng., 16, 235.
- Hess, W. N., 1957, Ann. Phys., 6, 116.
- Hornyak, W. F., 1952, Rev. Sci. Inst., 23, 264.
- Huber, P., Lewandowski, Z., Plattner, R., Poppelbaum, C., and Wagner, R.,
1962, Helv. Phys. Acta, 35, 557.
- Hughes, D. J., and Schwartz, R. B., 1958, BNL-325, 2nd Ed.

- Hurst, G. S., 1954, Brit. J. Radiol., 27, 253.
- Hurst, G. S., Harter, J. A., Hensley, P. N., Mills, W. A., Slater, M., and Reinhardt, P. W., 1956, Rev. Sci. Inst., 27, 153.
- Hurst, G. S., and Ritchie, R. H., 1953, Rev. Sci. Inst., 24, 664.
- Hurst, G. S., and Ritchie, R. H., 1962, Chapt. 6 in Nucl. Inst. and Uses, Vol. 1 by A. H. Snell.
- Hurst, G. S., Ritchie, R. H., and Wilson, H. N., 1951, Rev. Sci. Inst., 22, 981.
- Jarvis, R. G., 1964, AECL - 2072.
- Johnson, F. A., 1965, Tritium Considerations Associated with the Operation of Cockcroft-Walton-Type Neutron Generators.
- Johnson, D. R., Thorngate, J. H. Reinhardt, P. W., and Davis, F. J., 1965, Health Physics, 11, 759.
- Jones, T. D., Johnson, D. R., and Thorngate, J. H., 1965, Health Physics, 11, 519.
- Karama, R. A., and Wetherington, J. A., Jr., 1960, Trans. Amer. Nucl. Soc., 3, 221.
- Kogan, A. M., Petrov, G. G., Chudov, L. A., and Yampol'skii, P. M., 1959, Atomnaya Energiya, 7, 351.
- Lawrence, D. C., 1962, Health Physics, 7, 179.
- Lea, D. E. 1947, Action of Radiation on Living Cells, P.7.
- Lewandowski, Z., Huber, P., and Wagner, R., 1961, Helv. Phys. Acta 34, 457.
- Marinelli, L. D., 1953, Ann. Rev. Nucl. Sci., 3, 249.
- Melkonian, E., 1949, Phys. Rev., 76, 1750.
- Mills, W. A., and Hurst, G. S., 1954, Nucleonics, 12, 17.
- Mitchell, J. S., 1947(a), Brit. J. Radiol., 20, 79.

- Mitchell, J. S., 1947(b), Brit. J. Radiol., 20, 177.
- Muckenthaler, F. J., 1957, ORNL-2389, 270.
- McKibben, J. L., 1946, Phys. Rev., 70, 101A.
- McTaggart, M. H., 1958, A.W.R.E. NR/A-1/59.
- National Bureau of Standards Handbook 59, 1954, Permissible Dose from External Sources of Ionising Radiation.
- National Bureau of Standards Handbook 63, 1957, Protection against Neutron Radiation.
- National Bureau of Standards Handbook 72, 1960, Measurement of Neutron Flux and Spectra for Physical and Biological Applications.
- National Bureau of Standards Handbook 75, 1961, Measurement of Absorbed Dose of Neutrons, and Mixtures of Neutrons and Gamma Rays.
- National Bureau of Standards Handbook 84, 1963, Radiation Quantities and Units.
- National Bureau of Standards Handbook 85, 1964, Physical Aspects of Irradiation.
- National Bureau of Standards Handbook 88, 1963, Radiobiological Dosimetry.
- Neufeld, J., and Snyder, W. S., 1961, Selected Topics in Radiation Dosimetry, 35.
- Paić, M., Antolković, B., Tomaš, P., and Turk, M., 1963, Nucl. Inst. and Methods, 23, 19.
- Parker, H. M., 1948, Advances in Biological and Medical Physics, 1, 243.
- Prud'homme, J. T., 1964, Texas Nuclear Neutron Generators, 2nd Edition.
- Radkowsky, A., 1950, ANL-4476.
- Randolph, M. L., 1957, Radiation Research, 7, 47.
- Randolph, M. L., 1964, Annals of New York Acad. Sci., 114, 85.

- Report of the R.B.E. Committee, 1963, Health Physics, 2, 357.
- Reynolds, H. K., Dunbar, D. N. F., Wenzel, W. A., Whaling, W., 1953, Phys. Rev., 92, 742.
- Rich, M., and Mahey, R., 1954, UCRL-2301.
- Ritchie, R. H., and Eldridge, H. B., 1960, Nucl. Sci. and Eng., 8, 300.
- Rosenzweig, W., and Rossi, H. H., 1959, Radiation Research, 10, 532.
- Rossi, B. B., and Staub, H. H., 1949, Ionisation Chambers and Counters.
- Rossi, H. H., 1965, Health Physics, 11, 779.
- Rossi, H. H., and Failla, G., 1956, Nucleonics, 14, 32.
- Rossi, H. H., and Rosenzweig, W., 1953, 39th Annual Meeting of the Radiological Society of N. America, Dec. 13-18.
- Rossi, H. H., and Rosenzweig, W., 1955(a), Radiology, 64, 404.
- Rossi, H. H. and Rosenzweig, W., 1955(b), Radiation Research, 2, 417.
- Ruby, L., and Crawford, R. B., 1963, Nucl. Inst. and Methods, 24, 413.
- Sayeg, J. A., and Harris, P. S., 1958, LA-2174.
- Schermer, R. I., and Brownell, G., 1961, Nucl. Sci. and Eng., 11, 345.
- Seagrave, J. D., 1958, LAMS-2162.
- Shonka, F. R., Rose, J. E., and Failla, G., 1958, Proc. Second Int. Conf. on Peaceful Uses of Atomic Energy, Paper 749.
- Skjöldebrand, R., 1955, J. Nucl. Energy, 1, 299.
- Skyrme, T. H. R., 1943, U.K.A.E.A. Report MS 91 (also MS 91 2nd Ed. 1961).
- Smith, J. W., and Boot, S. J., 1961, A.E.R.E. R-3696.
- Snyder, W. S., 1950, Nucleonics, 6, 46.
- Snyder, W. S., 1963, Biological Effects of Neutron and Proton Irradiations, I.A.E.A., Vol. 1, 3.

Snyder, W. S., 1964, ORNL-3697, 117.

Snyder, W. S., and Neufeld, J., 1955, Brit. J. Radiol., 28, 331.

Steuer, M. F., and Wenzel, B. E., 1965, Nucl. Inst. Methods, 33, 131.

Stewart, L., 1955, Phys. Rev., 98, 740.

St. Romain, F. A., Bonner, T. W., Bramblett, R. L., and Hanna, J., 1962, Phys. Rev., 126, 1794.

Syrett, J. J., 1958, Nuclear Reactor Theory.

Tait, J. H., 1949, A.E.R.E. Report No. T/R 273.

Taylor, J. J., 1954, Application of Gamma Ray Build-up Data to Shield Design, WAPD-RM-217.

Thompson, I. M. G., and Lavender, A., 1965, C.E.G.B., RD/B/N385.

Tittle, C. W., 1951, Nucleonics, 8, 5, also 9, 60.

Tobias, C. A., Anger, H. O., and Lawrence, J. H., 1952, Am. J. Roentgenol and Radium Therapy, 67, 1.

Trubey, D. K., 1959, ORNL - 2750.

Turner, J. E., Zerby, C. D., Woodyard, R. L., Wright, H. A., Kinney, W. E., Snyder, W. S., and Neufeld, J., 1964, Health Physics, 10, 783.

Valente, F. A., 1963, A Manual of Experiments in Reactor Physics.

Wagner, E. B., and Hurst, G. S., 1958, Rev. Sci. Inst., 29, 153.

Wagner, E. B., and Hurst, G. S. 1961, Health Physics, 5, 20.

Warshaw, S. D., 1949, Phys. Rev., 76, 1759.

Wooten, P., Shalek, R. J., and Fletcher, G. H., 1954, Am. J. Roentgenology, Radium Therapy and Nuclear Medicine, Vol. LXXI, 683.

Wright, G. T., 1953, Phys. Rev., 91, 1282.

Young, D. S., 1955, LA-1938.

Young, W. R., 1965, UCRL-16149.

APPENDIX 1

Chapelcross Fortran Programme CXF 148

```

DIMENSION XIA(35),A(35,35),F(12),SUM(35), XIN(35),DIST(35),SUMC(35)
CORRN=(3.568/4.804)*1.0E-06*2.E-02*1.0E-04
24 CALL GODEC
DATA(F(I),I=1,11)/4.,.436,.155,.077,.045,.029,.02,.015,.011,.009,.
1007/
Y=FLDEC(4)
IF(YESDEC(0))2,3,3
3 WRITE(6,1)
1 FORMAT(19#ERROR IN INPUT DATA)
GO TO 4
2 CALL INDEX(JA,Y,11#MINOR*MAJOR)
GO TO (5,6,3),JA
5 JB=21
GO TO 7
6 JB=31
7 DO 8 I=1,JB
8 XIN(I)=FLDEC(0)
DO 9 JC=1,JB
DO 10 JD=1,JB
IF(JC-JD)12,11,13
11 JE=1
GO TO 14
12 JE=JD-JC+1
GO TO 14
13 JE=JC-JD+1
14 IF(JE.GT.11) GO TO 15
A(JD,JC)= XIN(JD)*F(JE)
GO TO 10
15 A(JD,JC)=0.
10 CONTINUE
SUM(JC)=0.0
DO 9 I=1,JB
SUM(JC)=SUM(JC)+A(I,JC)
9 SUMC(JC)=SUM(JC)*CORRN
WRITE(6,16)
16 FORMAT(//2(9X,10#DIST ALONG,4X,12#INTERMEDIATE,5X,9#GAMMA RAY, 8X)/
12(8X,12#PHANTOM(CMS),7X,4#DOSE,12X,4#DOSE,12X)//)
IF(JB-25)17,3,18
17 JF=11
GO TO 19

```

APPENDIX 1 (cont'd.)

Chapelcross Fortran Programme CXF 148 (cont'd.)

```
18  JF=16
19  JG=(JB-1)/2
    DO 20 I=1,JB
20  DIST(I)=FLOAT(I)-0.5
    DO 21 I=1,JG
    JH=I+JF
21  WRITE(6,22) DIST(I),SUM(I),SUMC(I),DIST(JH),SUM(JH), SUMC(JH)
22  FORMAT(2(12X,F4.1,11X,F6.2,7X,E10.3,8X)/)
    WRITE(6,23) DIST(JF),SUM(JF),SUMC(JF)
23  FORMAT(12X,F4.1,11X,F6.2,7XE10.3)
    GO TO 24
4   STOP
    END
```

APPENDIX 2

Chapelcross Fortran Programme CXF 157

```

17  CALL GODEC
    DIMENSION G(205),Y(17),X(17),A(20),CY(205),CE(205),CER(205),WS(3001),
    CERR(205,TOTA(205),TOTB(205),CORDS(205),CR(205),DOSE(40),CHAN(420),
    TEL(205),RAT(205),ATEL(205),TOTC(205),TOTD(205)
    R=FLDEC(0)
    D=FLDEC(0)
    T=FLDEC(0)
    G=FLDEC(0)
    P=FLDEC(0)
    ZM=FLDEC(3)
    N=0
4   Z=FLDEC(3)
    DATA HAST/1H*/
    IF(Z.EQ.HAST)GO TO 2
3   N=N+1
    C(N)=Z
    GO TO 4
2   CALL INDEX(M,ZM,10HPUBE*DT*DD)
    GO TO (101,102,103),M
101 L=9
    Y(1)=0.2
    Y(2)=0.5
    Y(3)=1.0
    Y(4)=2.0
    Y(5)=4.0
    Y(6)=6.0
    Y(7)=8.0
    Y(8)=10.0
    Y(9)=10.86
    X(9)=N
    X(8)=0.878*FLOAT(N)
    X(7)=0.633*FLOAT(N)
    X(6)=0.429*FLOAT(N)
    X(5)=0.224*FLOAT(N)
    X(4)=0.082*FLOAT(N)
    X(3)=0.024*FLOAT(N)
    X(2)=0.009*FLOAT(N)
    X(1)=0.002*FLOAT(N)
    GO TO 104

```

APPENDIX 2 (Cont'd.)

Chapelcross Fortran Programme CXF 157 (cont'd.)

```
102 L=15
    Y(1)=1.0
    Y(2)=2.0
    Y(3)=3.0
    Y(4)=4.0
    Y(5)=5.0
    Y(6)=6.0
    Y(7)=7.0
    Y(8)=8.0
    Y(9)=9.0
    Y(10)=10.0
    Y(11)=11.0
    Y(12)=12.0
    Y(13)=13.0
    Y(14)=14.0
    Y(15)=14.15
    X(15)=N
    X(14)=0.985*FLOAT(N)
    X(13)=0.884*FLOAT(N)
    X(12)=0.802*FLOAT(N)
    X(11)=0.716*FLOAT(N)
    X(10)=0.634*FLOAT(N)
    X(9)=0.545*FLOAT(N)
    X(8)=0.463*FLOAT(N)
    X(7)=0.384*FLOAT(N)
    X(6)=0.314*FLOAT(N)
    X(5)=0.243*FLOAT(N)
    X(4)=0.179*FLOAT(N)
    X(3)=0.116*FLOAT(N)
    X(2)=0.063*FLOAT(N)
    X(1)=0.022*FLOAT(N)
    GO TO 104
```

APPENDIX 2 (cont'd.)

Chapelcross Fortran Programme CXF 157 (cont'd.)

```

103 L=17
    Y(1)=0.2
    Y(2)=0.4
    Y(3)=0.6
    Y(4)=0.8
    Y(5)=1.0
    Y(6)=1.2
    Y(7)=1.4
    Y(8)=1.6
    Y(9)=1.8
    Y(10)=2.0
    Y(11)=2.2
    Y(12)=2.4
    Y(13)=2.6
    Y(14)=2.8
    Y(15)=3.0
    Y(16)=3.2
    Y(17)=3.4
    X(17)=N
    X(16)=0.918*FLOAT(N)
    X(15)=0.843*FLOAT(N)
    X(14)=0.755*FLOAT(N)
    X(13)=0.616*FLOAT(N)
    X(12)=0.616*FLOAT(N)
    X(11)=0.535*FLOAT(N)
    X(10)=0.453*FLOAT(N)
    X(9)=0.377*FLOAT(N)
    X(8)=0.296*FLOAT(N)
    X(7)=0.239*FLOAT(N)
    X(6)=0.182*FLOAT(N)
    X(5)=0.140*FLOAT(N)
    X(4)=0.112*FLOAT(N)
    X(3)=0.069*FLOAT(N)
    X(2)=0.043*FLOAT(N)
    X(1)=0.018*FLOAT(N)
104 CALL REDPAT(X,Y,L,A,4,1.0E-02,WS,M)
    D05K=1,N
    Z=K
    CY(K)=0.0
    D06I=1,M
    MN=M-I+1

```

APPENDIX 2 (cont'd.)

Chapelcross Fortran Programme CXF 157 (cont'd.)

```

6   CY(K)=CY(K)+A(MN+1)*(Z**MN)
5   CY(K)=CY(K)+A(1)
   IF(70..GT.R)GO TO 25
   DO 26I=1,N
   CE(I)=C(I)*CY(I)
   CER(I)=CE(I)*(((70.+D)/70.)**2)
   CERR(I)=CER(I)*(1.795/(G*T))*P
   CORDS(I)=CERR(I)
26  CR(I)=C(I)
   GO TO 8
25  DO7I=1,N
   CE(I)=C(I)*CY(I)
   CER(I)=CE(I)*(((R+D)/R)**2)
   CERR(I)=CER(I)*(1.795/(G*T))*P
   CORDS(I)=CERR(I)
7   CR(I)=C(I)
8   TOTA(1)=C(1)
   DO31I=2,N
31  TOTA(I)=TOTA(I-1)+C(I)
   TOTB(1)=TOTA(N)
   DO32J=2,N
32  TOTB(J)=TOTB(J-1)-C(J-1)
   SUMCER=0
   DO40I=1,N
40  SUMCER=SUMCER+CER(I)
   SUCERR=0
   DO41J=1,N
41  SUCERR=SUCERR+CERR(J)
   DO 50 I=1,15
   DOSE(I)=CERR(I+15)
50  CHAN(I)=I+15
   CALL REDPAT (CHAN,DOSE,15,A,1,10,WS,M)
   DO 58 K=1,15
   CHAN(K)=K
   CORDS(K)=A(1)+A(2)*CHAN(K)
   IF(70..GT.R) GO TO 56
51  CR(K)=CORDS(K)/(CY(K)*1.795*P/(G*T)*((70.+D)/70.)**2)
   GO TO 58
56  CR(K)=CORDS(K)/(CY(K)*1.795*P/(G*T)*((R+D)/R)**2)
58  CONTINUE
   TOTC(1)=CR(1)
   DO 59 I=2,N
59  TOTC(I)=TOTC(I-1)+CR(I)
   TOTD(1)=TOTC(N)
   DO 60 J=2,N

```

APPENDIX 2 (cont'd.)

Chapelcross Fortran Programme CXF 157 (cont'd.)

```

60  TOTD(J)=TOTD(J-1)-CR(J-1)
    SUCORD=0
    DO 55 I=1,N
    SUCORD=SUCORD+CORDS(I)
    IF(CY(I).LE.2.) GO TO 52
    IF(CY(I).LE.10.) GO TO 53
    GO TO 54
52  TEL(I)=46.5/CY(I)**0.7
    GO TO 55
53  TEL(I)=48.4/CY(I)**0.75
    GO TO 55
54  TEL(I)=53.2/CY(I)  0.8
55  CONTINUE
    NZ=N-1
    DO 61 I=1,NZ
    RAT(I)=CORDS(I)/(TEL(I)-TEL(I+1))
    ATEL(I)=(TEL(I)+TEL(I+1))/2.0
61  CONTINUE
    WRITE (6,62)
62  FORMAT(//(4X7HCHANNEL,3X8HORIGINAL,4X5HTOTAL,4X5HTOTAL,3X6HEENERGY,
15X4HDOSE,3X9HCORRECTED,3X9HCORRECTED,4X5HTOTAL,4X5HTOTAL,5X3HLET/7
2X2HNO,6X6HCOUNTS,5X6HCOUNTS,3X6HCOUNTS,2X6HFACTOR,3X8HRADS/SEC,3X4
3HDOSE,7X6HCOUNTS,6X6HCOUNTS,3X6HCOUNTS,3X5HKEV/U,)//)
    DO 63 I=1,N
63  WRITE(6,64) I,C(I),TOTA(I),TOTB(I),CY(I),CERR(I),CORDS(I),CR(I),
TOTC(I),TOTD(I),TEL(I)
64  FORMAT(I8,6X,F6.0,3X,F8.0,F9.0,F7.2,2X,F9.2,F9.2,5X,F7.0,5X,F7.0,2X,
F7.0,F9.2)
    WRITE(6,65) SUCERR,SUCORD
65  FORMAT(49X,F9.2,F9.2)
    WRITE(6,66)
66  FORMAT(//2(24X,9HLET VALUE,4X,9HDOSE/DLET,))
    NX=N/2
    DO 68 I=NX,NZ
    IA=I-NX+1
68  WRITE(6,67) ATEL(IA),RAT(IA),ATEL(I),RAT(I)
67  FORMAT(2(22X,F10.3,5X,F9.3))
    CALL GRAPH (17HLET VALUE (KEV/U),26HRATIO OF DOSE TO DELTA LET,ATEL,
RAT,N)
    GO TO 17
    END

```

APPENDIX 3

```

LET. FOR PROTONS IN WATER L(E)=
      7.93*LOGE(31.2E)/E SEE BOAG P 325
DIMENSION ALET(10)
E=0
DO 1 I=1,150
DO 2 J=1,10
E=E+.01
2  ALET(J)=7.93*LOGF(31.2*E)/E
1  PRINT3,ALET,E
C  DOSE AS F(LET) FOLLOWING BOAG P 325-331.
C  DATA READS PROTON ENERGY IN MEV., FACTOR, PHIS(LET), PHIM(LET)
C  PHIS=EQN.(7)  PHIM=EQN.(12)  FACTOR=PHIS/(1-E/EO).
12 CONTINUE
E=0
8  READ 5,EO
IF(EO)7,7,9
9  DO 4 I=1,500
E=E+.05
IF(E=EO) 11,11,12
11 CONTINUE
Y=LOGF(31.2*E)-1.
FACTOR=2.*E*E/(7.93*EO*Y)
PHIS=FACTOR*(1.-E/EO)
PHIM=FACTOR*LOGF(EO/E)*.5
PRINT 6,E,FACTOR,PHI,PHIM
4  CONTINUE
GO TO 12
7  CALL EXIT
5  FORMAT(F5.2)
6  FORMAT(4F10.4)
3  FORMAT(11F10.4)
END

```